

---

# CHAPTER

# 7

---

## NUMERICAL SOLUTIONS OF QUASI- ONE- DIMENSIONAL NOZZLE FLOWS

*When you measure what you are speaking about, and express it in numbers, you know something about it; but when you cannot measure it, when you cannot express it in numbers, your knowledge is of a meager and unsatisfactory kind: it may be the beginning of knowledge, but you have scarcely, in your thoughts, advanced to the stage of science.*

William Thomson, Lord Kelvin, from Popular Lectures and Addresses, 1891–1894

### 7.1 INTRODUCTION: THE FORMAT FOR CHAPTERS IN PART III

For the next four chapters, which constitute Part III, the following format will be followed. Each chapter will deal with a specific flow field; for example, the present chapter deals with the quasi-one-dimensional flow through a convergent-divergent nozzle. Each chapter will be subdivided into three main parts:

1. *Physical description of the flow.* The physical aspects of the flow will be described, and pertinent equations and relationships obtained from the analytical solution will be reviewed. If experimental data are appropriate, they will be

discussed. The purpose here is to give you a physical understanding of the flow field, to be calculated subsequently with our CFD techniques.

2. *CFD solution: intermediate steps.* A specific CFD technique (one of those discussed in Chap. 6) will be chosen for the numerical solution of the flow problem. The pertinent partial differential equations or the integral form of the equations, as the case may be, most suited for the specific CFD technique as applied to the specific flow problem will be set forth. The solution will be set up, step by step, and the numerical operations will be carried through in detail for the first few steps. Numbers will be given for all stages of the calculation during these intermediate steps so that you can compare them directly with your own calculations. Such matters as the calculations at internal points, at the boundaries, the numerical implementation of boundary conditions, and the determination of step size (if appropriate) will be covered in detail.
3. *CFD solution: final results.* Tabulations and graphs of the final numerical solution to the flow field will be given. These final results will be compared with the exact analytical (and/or experimental) results, and an evaluation of the accuracy of the CFD solution will be made.

*Note:* You have an option at this stage. You can decide simply to read these chapters, obtain a detailed understanding of the implementation of various CFD techniques to various problems, and get a feeling for the results. Or, you can also decide to write your own computer programs to calculate the answers yourself. It is for those of you who make the latter decision that some of the intermediate numbers obtained on the way toward a solution will be given. These numbers will be boxed and easy to follow so that you can check on the early calculational aspects of the problem. Also, the final answers will be given in some detail so that you can check the final results obtained from your computer program. You are strongly encouraged to make this latter decision: to write your own computer programs for the various solutions as we progress through the next four chapters. Simply reading the material is certainly worthwhile, but it is analogous to sitting on the sidelines watching a football game. By writing your own programs and calculating along with the steps given in the book, you will be playing the game yourself and getting your hands dirty. To really learn CFD, you must get your hands dirty; i.e., you must wade into the calculations and do them yourself. The flow problems and their CFD solutions given in the next four chapters are suitable for personal computers; you do not need a powerful mainframe or even a major workstation for their solution. Indeed, the present author has used his own Macintosh computer for the solutions described herein.

In some cases, more than one CFD technique will be used to solve the same flow problem. This is done to give you some comparison of the strengths and weaknesses of one technique versus another and a feeling for the relative difficulty of setting up one technique on the computer compared to another.

We are finally ready to go. This author wishes you happy computing!

## 7.2 INTRODUCTION TO THE PHYSICAL PROBLEM: SUBSONIC-SUPersonic ISENTROPIC FLOW

The flow problem discussed here can be found in any gas dynamic textbook; for example, it is covered in detail in Chap. 10 of the author's book *Fundamentals of Aerodynamics*, 2d ed. (Ref. 8), as well as in Chap. 5 of the author's book *Modern Compressible Flow*, 2d ed. (Ref. 21). In the present section, we will review some of the important physical and analytical aspects of this flow.

We consider the steady, isentropic flow through a convergent-divergent nozzle as sketched in Fig. 7.1. The flow at the inlet to the nozzle comes from a reservoir where the pressure and temperature are denoted by  $p_0$ , and  $T_0$ , respectively. The cross-sectional area of the reservoir is large (theoretically,  $A \rightarrow \infty$ ), and hence the velocity is very small ( $V \rightarrow 0$ ). Thus,  $p_0$  and  $T_0$  are the stagnation values, or *total* pressure and *total* temperature, respectively. The flow expands isentropically to supersonic speeds at the nozzle exit, where the exit pressure, temperature, velocity, and Mach number are denoted by  $p_e$ ,  $T_e$ ,  $V_e$ , and  $M_e$ , respectively. The flow is locally subsonic in the convergent section of the nozzle, sonic at the throat (minimum area), and supersonic at the divergent section. The sonic flow ( $M = 1$ ) at the throat means that the local velocity at this location is equal to

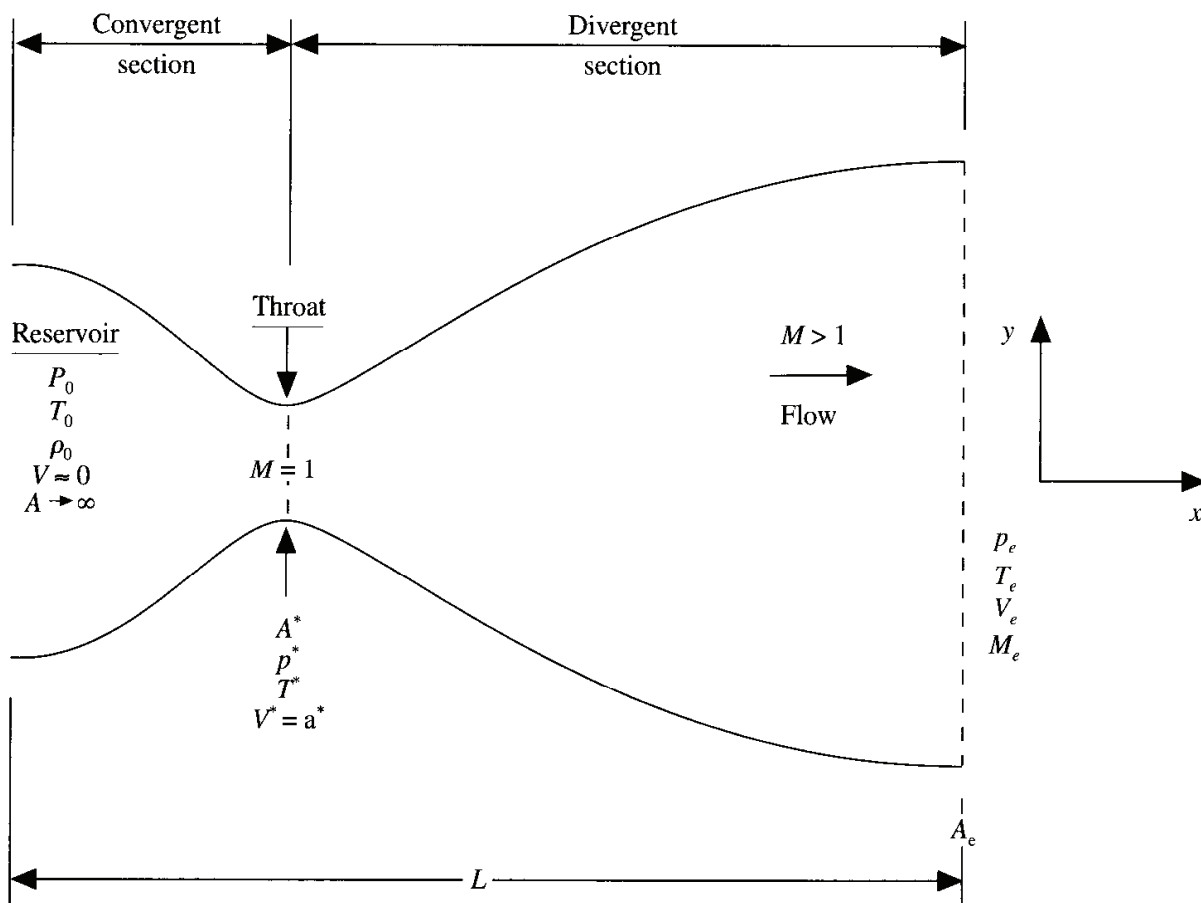


**FIG. 7.1**

Schematic for subsonic-supersonic isentropic nozzle flow.

the local speed of sound. Using an asterisk to denote sonic flow values, we have at the throat  $V = V^* = a^*$ . Similarly, the sonic flow values of pressure and temperature are denoted by  $p^*$  and  $T^*$ , respectively. The area of the sonic throat is denoted by  $A^*$ . We assume that at a given section, where the cross-sectional area is  $A$ , the flow properties are uniform across that section. Hence, although the area of the nozzle changes as a function of distance along the nozzle,  $x$ , and therefore in reality the flow field is two-dimensional (the flow varies in the two-dimensional  $xy$  space), we make the *assumption* that the flow properties vary only with  $x$ ; this is tantamount to assuming uniform flow properties across any given cross section. Such flow is defined as *quasi-one-dimensional* flow.

The governing continuity, momentum, and energy equations for this quasi-one-dimensional, steady, isentropic flow can be expressed, respectively, as

$$\text{Continuity : } \rho_1 V_1 A_1 = \rho_2 V_2 A_2 \quad (7.1)$$

$$\text{Momentum : } p_1 A_1 + \rho_1 V_1^2 A_1 + \int_{A_1}^{A_2} p \, dA = p_2 A_2 + \rho_2 V_2^2 A_2 \quad (7.2)$$

$$\text{Energy : } h_1 + \frac{V_1^2}{2} = h_2 + \frac{V_2^2}{2} \quad (7.3)$$

where subscripts 1 and 2 denote different locations along the nozzle. In addition, we have the perfect gas equation of state,

$$p = \rho R T \quad (7.4)$$

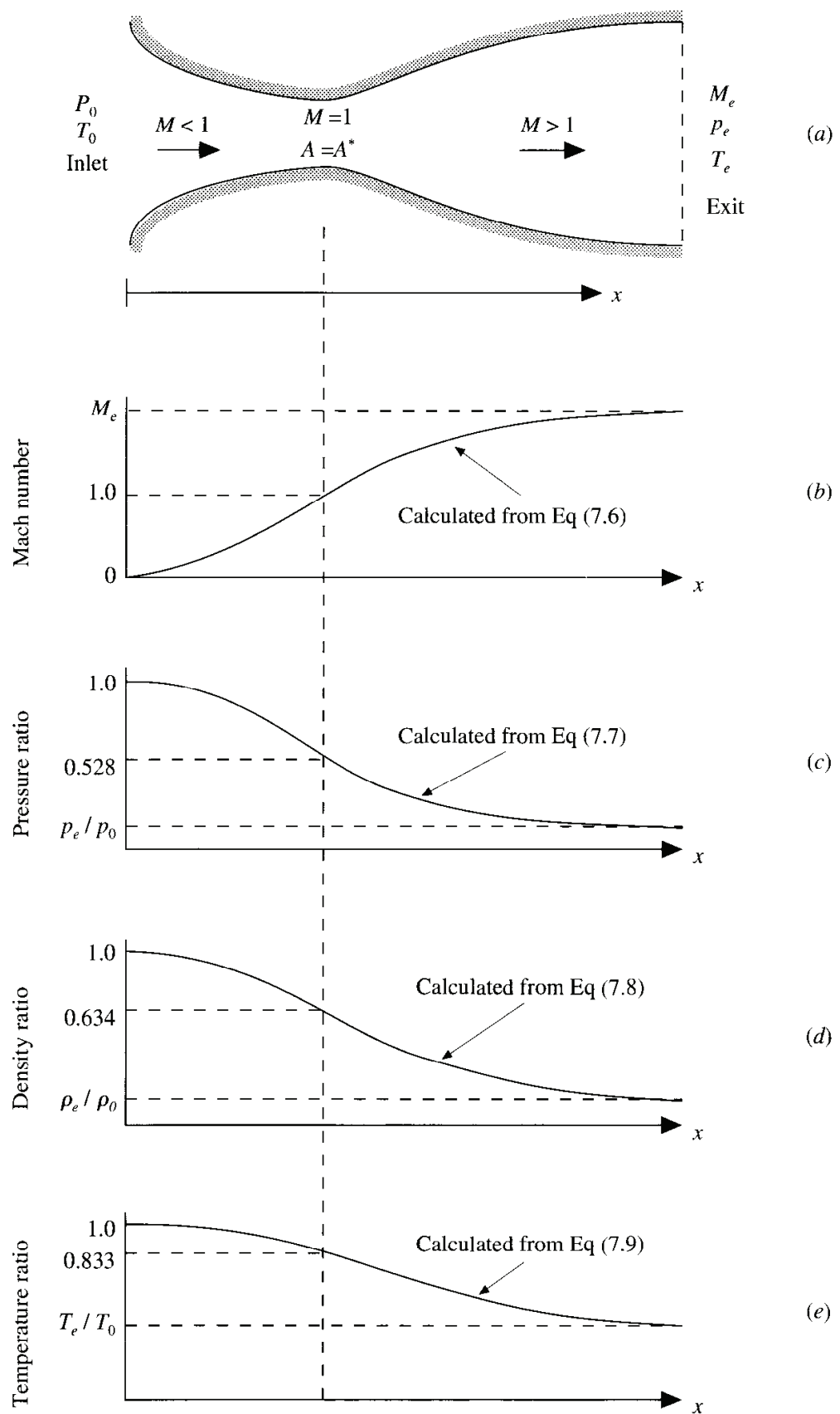
as well as the relation for a calorically perfect gas,

$$h = c_p T \quad (7.5)$$

Equations (7.1) to (7.5) can be solved analytically for the flow through the nozzle. Some results are as follows. The Mach number variation through the nozzle is governed exclusively by the area ratio  $A/A^*$  through the relation

$$\left( \frac{A}{A^*} \right)^2 = \frac{1}{M^2} \left[ \frac{2}{\gamma + 1} \left( 1 + \frac{\gamma - 1}{2} M^2 \right) \right]^{(\gamma + 1)/(\gamma - 1)} \quad (7.6)$$

where  $\gamma$  = ratio of specific heats =  $c_p/c_v$ . For air at standard conditions,  $\gamma = 1.4$ . For a nozzle where  $A$  is specified as a function of  $x$ , hence  $A/A^*$  is known as a function of  $x$ , then Eq. (7.6) allows the (implicit) calculation of  $M$  as a function of  $x$ . This is sketched in Fig. 7.2b. In turn, the variation of pressure, density, and temperature as a function of Mach number (and hence as a function of  $A/A^*$ , thus  $x$ ) is given,

**FIG. 7.2**

Qualitative aspects of quasi-one-dimensional nozzle flow: isentropic subsonic-supersonic solution.

respectively, by

$$\frac{p}{p_0} = \left(1 + \frac{\gamma - 1}{2} M^2\right)^{-\gamma/(\gamma-1)} \quad (7.7)$$

$$\frac{\rho}{\rho_0} = \left(1 + \frac{\gamma - 1}{2} M^2\right)^{-1/(\gamma-1)} \quad (7.8)$$

$$\frac{T}{T_0} = \left(1 + \frac{\gamma - 1}{2} M^2\right)^{-1} \quad (7.9)$$

These variations are sketched in Fig. 7.2c to e.

The nozzle flow described above just does not “happen” by itself. That is, if you take the nozzle sketched in Fig. 7.2a and place it on a desk in front of you, the air does not just start flowing through the nozzle by itself. As with all mechanical systems, it takes a force to accelerate a given mass; the nozzle flow is no different. In this case, the force exerted on the gas to accelerate it through the nozzle is supplied by the pressure ratio across the nozzle,  $p_0/p_e$ . For a nozzle with a specified area ratio  $A_e/A^*$ , the pressure ratio required to establish the subsonic-supersonic isentropic flow sketched in Fig. 7.2 must be a very specific value, namely, that value shown in Fig. 7.2c. This pressure ratio is a boundary condition applied to the flow; in the laboratory, it is provided by a high-pressure air reservoir at the inlet and/or a vacuum source at the exit.

### 7.3 CFD SOLUTION OF SUBSONIC-SUPersonic ISENTROPIC NOZZLE FLOW: MACCORMACK’S TECHNIQUE

At this point, you are reminded that *any* numerical solution of the steady, isentropic quasi-one-dimensional nozzle flow is overkill; we have a closed-form analytical solution as described in Sec. 7.2, and therefore in general a numerical solution is not needed. However, that is not the point. What we want to accomplish here is to illustrate the application of various CFD techniques, and we are intentionally choosing a flow problem with a known analytic solution for this illustration. That is, we are following the philosophy as set forth in Sec. 7.1.

In this section we choose to illustrate the application of MacCormack’s technique as described in Sec. 6.3. In particular, we will set up a time-marching, finite-difference solution for the quasi-one-dimensional nozzle flow. Before progressing further, pause at this point, return to Sec. 6.3, and read it again, carefully. In the present section, we will assume that you fully understand MacCormack’s technique to the extent described in Sec. 6.3. Also, reexamine Fig. 1.32b, which illustrates the major ideas that feed into this application.

#### 7.3.1 The Setup

In this section, we will set up three eschelons of equations as follows:

1. The governing flow equations will be couched in terms of *partial differential equations* suitable for the time-marching solution of quasi-one-dimensional flow (the closed-form algebraic equations discussed in Sec. 7.2 are for a steady flow and are not suitable for the present purpose).
2. The finite-difference expressions pertaining to MacCormack's technique as applied to this problem will be set up.
3. Other details for the numerical solution (such as the calculation of the time step and the treatment of boundary conditions) will be formulated.

**THE GOVERNING FLOW EQUATIONS.** Beginning with step 1 above, recall that we have derived the governing partial differential equations for inviscid flow (the Euler equations) in Chap. 2; these are summarized in Eqs. (2.82) to (2.86). Since we are dealing with a one-dimensional inviscid flow for our nozzle problem, it would seem appropriate to take Eqs. (2.82) to (2.86), simply write them down for one-dimensional flow, and proceed ahead. After all, these equations have been derived in Chap. 2 in the most general sense, and we should be able to make use of them. *However, such is not the case with quasi-one-dimensional nozzle flow.* Why? The answer lies with the simplifying assumption we have made with quasi-one-dimensional flow as described in Sec. 7.2, namely, we assume that the flow properties are uniform across any given cross section of the nozzle. In so doing, we have somewhat twisted the physics of the flow.\* Return to Fig. 7.1 for a moment. Note that, in reality, the real nozzle flow is a two-dimensional flow because, with the area changing as a function of  $x$ , in actuality there will be flow-field variations in both the  $x$  and  $y$  directions. This is the real physics of the flow, and Eqs. (2.82) to (2.86) properly describe such a two-dimensional flow. On the other hand, the *assumption* of quasi-one-dimensional flow dictates that the flow properties are functions of  $x$  only. Since this assumption twists the real physics of the flow, then Eqs. (2.82) to (2.86) are not necessarily appropriate for quasi-one-dimensional flow. On the other hand, for the equations that *are* appropriate for quasi-one-dimensional flow, we would at least like for the overall physical principles of (1) mass conservation, (2) Newton's second law, and (3) energy conservation to hold exactly, in spite of our twisted physics due to the quasi-one-dimensional assumption. To ensure that these physical principles are satisfied, we must return to the *integral forms* of the governing equations derived in Chap. 2 and apply these integral forms to a control volume consistent with the quasi-one-dimensional assumption. Let us proceed.

---

\* To say that we are “twisting” the physics of the flow is a rather strong statement in order to emphasize a point. What we are really doing with our quasi-one-dimensional assumptions is constructing a *simplified engineering model* of the flow. Such *modeling* to simplify more complicated problems is done very frequently in engineering and physical science. Of course, the price we pay for such modeling is usually some compromise with the real physics of the flow.

We start with the integral form of the continuity equation given by Eq. (2.19), repeated below:

$$\frac{\partial}{\partial t} \int \int \int_{\mathcal{V}} \rho \, d\mathcal{V} + \int \int_S \rho \mathbf{V} \cdot d\mathbf{S} = 0 \quad (2.19)$$

We apply this equation to the shaded control volume shown in Fig. 7.3. This control volume is a slice of the nozzle flow, where the infinitesimal thickness of the slice is  $dx$ . On the left side of the control volume, consistent with the quasi-one-dimensional assumption, the density, velocity, pressure, and internal energy, denoted by  $\rho$ ,  $V$ ,  $p$ , and  $e$ , respectively, are uniform over the area  $A$ . Similarly, on the right side of the control volume, the density, velocity, pressure, and internal energy, denoted by  $\rho + d\rho$ ,  $V + dV$ ,  $p + dp$ , and  $e + de$ , respectively, are uniform over the area  $A + dA$ . Applied to the control volume in Fig. 7.3, the volume integral in Eq. (2.19) becomes, in the limit as  $dx$  becomes very small,

$$\frac{\partial}{\partial t} \int \int \int_{\mathcal{V}} \rho \, d\mathcal{V} = \frac{\partial}{\partial t} (\rho A \, dx) \quad (7.10)$$

where  $A \, dx$  is the volume of the control volume in the limit of  $dx$  becoming vanishingly small. The surface integral in Eq. (2.19) becomes

$$\int \int_S \rho \mathbf{V} \cdot d\mathbf{S} = -\rho V A + (\rho + d\rho)(V + dV)(A + dA) \quad (7.11)$$

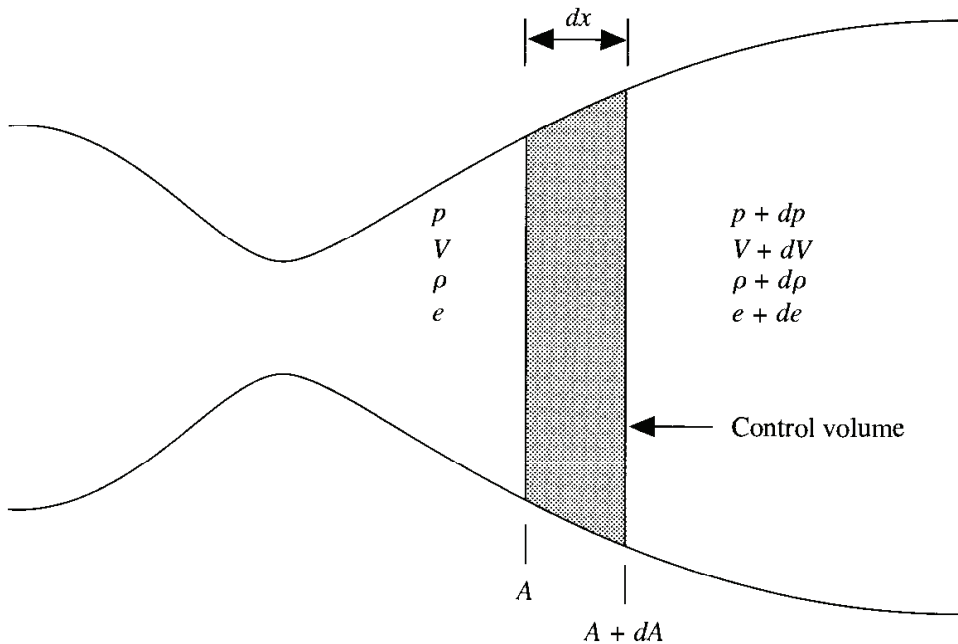


**FIG. 7.3**

Control volume for deriving the partial differential equations for unsteady, quasi-one-dimensional flow.

where the minus sign on the leading term on the right-hand side is due to the vectors  $\mathbf{V}$  and  $d\mathbf{S}$  pointing in opposite directions over the left face of the control volume, and hence the dot product is negative. (Recall from Chap. 2 that  $d\mathbf{S}$  always points *out* of the control volume, by convention.) Expanding the triple product term in Eq. (7.11), we have

$$\begin{aligned} \iint_S \rho \mathbf{V} \cdot d\mathbf{S} &= -\rho VA + \rho VA + \rho V dA + \rho A dV + \rho dV dA \\ &\quad + AV d\rho + V dA d\rho + A dV d\rho + d\rho dV dA \end{aligned} \quad (7.12)$$

In the limit as  $dx$  becomes very small, the terms involving *products* of differentials in Eq. (7.12), such as  $\rho dV dA$ ,  $d\rho dV dA$ , go to zero much faster than those terms involving only one differential. Hence, in Eq. (7.12), all terms involving *products* of differentials can be dropped, yielding in the limit as  $dx$  becomes very small

$$\iint_S \rho \mathbf{V} \cdot d\mathbf{S} = \rho V dA + \rho A dV + AV d\rho = d(\rho AV) \quad (7.13)$$

Substituting Eqs. (7.10) and (7.13) into (2.19), we have

$$\frac{\partial}{\partial t} (\rho A dx) + d(\rho AV) = 0 \quad (7.14)$$

Dividing Eq. (7.14) by  $dx$  and noting that  $d(\rho AV)/dx$  is, in the limit as  $dx$  goes to zero, the definition of the partial derivative with respect to  $x$ , we have

$$\frac{\partial(\rho A)}{\partial t} + \frac{\partial(\rho AV)}{\partial x} = 0 \quad (7.15)$$

Equation (7.15) is the partial differential equation form of the continuity equation *suitable for unsteady, quasi-one-dimensional flow*. It ensures that mass is conserved for this model of the flow.

It is interesting to pause for a moment and compare this with the general continuity equation for three-dimensional flow, Eq. (2.82b), specialized for one-dimensional flow. For such a case, Eq. (2.82b) becomes

$$\frac{\partial \rho}{\partial t} + \frac{\partial(\rho u)}{\partial x} = 0 \quad (7.16)$$

where  $u$  is the  $x$  component of velocity. Clearly, Eq. (7.16) is different from Eq. (7.15). Equation (7.16) applies to a *truly* one-dimensional flow, where  $A$  is constant with respect to  $x$ . It does *not* represent a proper statement of the conservation of mass for our *model* of quasi-one-dimensional flow, where  $A = A(x)$ ; instead, Eq. (7.15) is a proper statement of mass conservation for our model. Of course, note that for the special case of constant-area flow, Eq. (7.15) reduces to Eq. (7.16).

We now turn to the integral form of the  $x$  component of the momentum equation, (from Prob. 2.2) written below for an inviscid flow (neglecting the viscous

stress terms) with no body forces,

$$\frac{\partial}{\partial t} \int_V \int (\rho u) dV + \int_S (\rho u \mathbf{V}) \cdot d\mathbf{S} = - \int_S (p dS)_x \quad (7.17)$$

where the term  $(p dS)_x$  denotes the  $x$  component of the vector  $p \mathbf{dS}$ . We apply Eq. (7.17) to the shaded control volume in Fig. 7.3. In Eq. (7.17), the integrals on the left side are evaluated in the same manner as discussed above in regard to the continuity equation. That is,

$$\frac{\partial}{\partial t} \int_V \int (\rho u) dV = \frac{\partial}{\partial t} (\rho V A dx) \quad (7.18)$$

and

$$\int_S (\rho u \mathbf{V}) \cdot d\mathbf{S} = -\rho V^2 A + (\rho + d\rho)(V + dV)^2(A + dA) \quad (7.19)$$

The evaluation of the pressure force term on the right-hand side of Eq. (7.17) is best carried out with the aid of Fig. 7.4. Here, the  $x$  components of the vector  $p \mathbf{dS}$  are shown on all four sides of the control volume. Remember that  $\mathbf{dS}$  always points *away* from the control volume; hence any  $x$  component  $(p dS)_x$  that acts toward the left (in the negative  $x$  direction) is a negative quantity, and any  $x$  component  $(p dS)_x$  that acts toward the right (in the positive  $x$  direction) is a positive quantity. Also note that the  $x$  component of  $p \mathbf{dS}$  acting on the top and bottom inclined faces of the control volume in Fig. 7.4 can be expressed as the pressure  $p$  acting on the *component* of the inclined area projected perpendicular to the  $x$  direction,  $(dA)/2$ ; hence, the contribution of each inclined face (top or bottom) to the pressure integral in Eq. (7.17) is  $-p(dA/2)$ . All together, the right-hand side of Eq. (7.17) is expressed as follows:

$$\int_S (p dS)_x = -pA + (p + dp)(A + dA) - 2p\left(\frac{dA}{2}\right) \quad (7.20)$$

Substituting Eqs. (7.18) to (7.20) into (7.17), we have

$$\begin{aligned} \frac{\partial}{\partial t} (\rho V A dx) - \rho V^2 A + (\rho + d\rho)(V + dV)^2(A + dA) \\ = pA - (p + dp)(A + dA) + p dA \end{aligned} \quad (7.21)$$

Canceling like terms and ignoring products of differentials, Eq. (7.21) becomes in the limit of  $dx$  becoming very small

$$\frac{\partial}{\partial t} (\rho V A dx) + d(\rho V^2 A) = -A dp \quad (7.22)$$

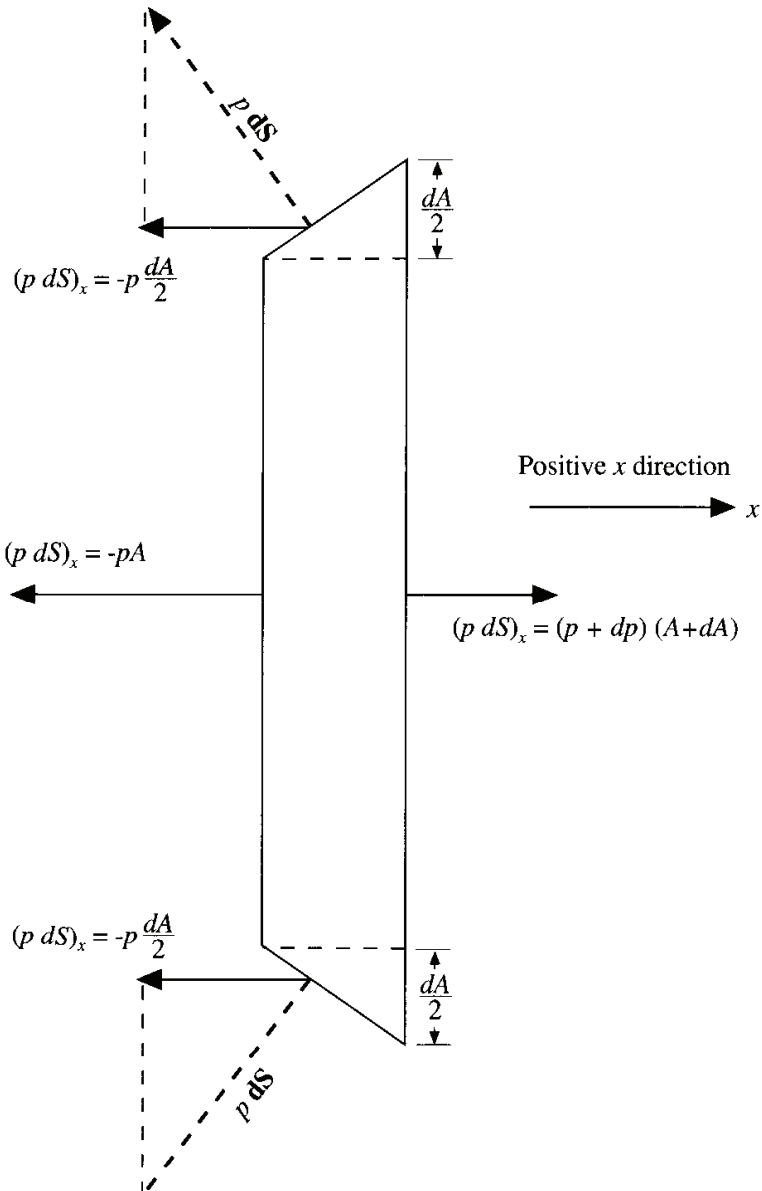


**FIG. 7.4**  
The forces in the  $x$  direction acting on the control volume.

Dividing Eq. (7.22) by  $dx$  and taking the limit as  $dx$  goes to zero, we obtain the partial differential equation

$$\frac{\partial(\rho VA)}{\partial t} + \frac{\partial(\rho V^2 A)}{\partial x} = -A \frac{\partial p}{\partial x} \quad (7.23)$$

We could live with Eq. (7.23) as it stands—it represents the *conservation* form of the momentum equation for quasi-one-dimensional flow. However, let us obtain the equivalent nonconservation form. This is done by multiplying the continuity equation, Eq. (7.15), by  $V$ , obtaining

$$V \frac{\partial(\rho A)}{\partial t} + V \frac{\partial(\rho VA)}{\partial x} = 0 \quad (7.24)$$

and then subtracting Eq. (7.24) from Eq. (7.23).

$$\frac{\partial(\rho VA)}{\partial t} - V \frac{\partial(\rho A)}{\partial t} + \frac{\partial(\rho V^2 A)}{\partial x} - V \frac{\partial(\rho VA)}{\partial x} = -A \frac{\partial p}{\partial x} \quad (7.25)$$

Expanding the derivatives on the left-hand side of Eq. (7.25) and canceling like terms, we have

$$\rho A \frac{\partial V}{\partial t} + \rho A V \frac{\partial V}{\partial x} = -A \frac{\partial p}{\partial x} \quad (7.26)$$

Dividing Eq. (7.26) by  $A$ , we finally obtain

$$\rho \frac{\partial V}{\partial t} + \rho V \frac{\partial V}{\partial x} = - \frac{\partial p}{\partial x} \quad (7.27)$$

Equation (7.27) is the momentum equation appropriate for quasi-one-dimensional flow, written in nonconservation form.

One of the reasons for obtaining the nonconservation form of the momentum equation is to compare it with the general result expressed by Eq. (2.83a). For one-dimensional flow with no body forces, Eq. (2.83a) is written as

$$\rho \frac{\partial u}{\partial t} + \rho u \frac{\partial u}{\partial x} = - \frac{\partial p}{\partial x} \quad (7.28)$$

This is stylistically the same form as Eq. (7.27) for quasi-one-dimensional flow. Equations (7.27) and (7.28) simply demonstrate that the classic form of Euler's equation, generically written as

$$dp = -\rho V dV$$

holds for both types of flow.

Finally, let us consider the integral form of the energy equation, as obtained in Prob. 2.2. For an adiabatic flow ( $\dot{q} = 0$ ) with no body forces and no viscous effects, the integral form of the energy equation is

$$\frac{\partial}{\partial t} \int \int \int_{\mathcal{V}} \rho \left( e + \frac{V^2}{2} \right) d\mathcal{V} + \int \int_S \rho \left( e + \frac{V^2}{2} \right) \mathbf{V} \cdot \mathbf{d}\mathbf{S} = - \int \int_S (p\mathbf{V}) \cdot \mathbf{d}\mathbf{S} \quad (7.29)$$

Applied to the shaded control volume in Fig. 7.3, and keeping in mind the pressure forces shown in Fig. 7.4, Eq. (7.29) becomes

$$\begin{aligned} & \frac{\partial}{\partial t} \left[ \rho \left( e + \frac{V^2}{2} \right) A dx \right] - \rho \left( e + \frac{V^2}{2} \right) VA \\ & + (\rho + d\rho) \left[ e + de + \frac{(V + dV)^2}{2} \right] (V + dV)(A + dA) \\ & = - \left[ -pVA + (p + dp)(V + dV)(A + dA) - 2 \left( pV \frac{dA}{2} \right) \right] \end{aligned} \quad (7.30)$$

Neglecting products of differentials and canceling like terms, Eq. (7.30) becomes

$$\frac{\partial}{\partial t} \left[ \rho \left( e + \frac{V^2}{2} \right) A dx \right] + d(\rho e VA) + \frac{d(\rho V^3 A)}{2} = -d(pAV) \quad (7.31)$$

or

$$\frac{\partial}{\partial t} \left[ \rho \left( e + \frac{V^2}{2} \right) A dx \right] + d \left[ \rho \left( e + \frac{V^2}{2} \right) VA \right] = -d(pAV) \quad (7.32)$$

Taking the limit as  $dx$  approaches zero, Eq. (7.32), becomes the following partial differential equation:

$$\frac{\partial[\rho(e + V^2/2)A]}{\partial t} + \frac{\partial[\rho(e + V^2/2)VA]}{\partial x} = -\frac{\partial(pAV)}{\partial x} \quad (7.33)$$

Equation (7.33) is the conservation form of the energy equation expressed in terms of the total energy  $e + V^2/2$ , appropriate for unsteady, quasi-one-dimensional flow. Let us obtain from Eq. (7.33) the nonconservation form expressed in terms of internal energy by itself. The latter can be achieved by multiplying Eq. (7.23) by  $V$ , obtaining

$$\frac{\partial[\rho(V^2/2)A]}{\partial t} + \frac{\partial[\rho(V^3/2)A]}{\partial x} = -AV \frac{\partial p}{\partial x} \quad (7.34)$$

and subtracting Eq. (7.34) from (7.33), yielding

$$\frac{\partial(\rho e A)}{\partial t} + \frac{\partial(\rho e V A)}{\partial x} = -p \frac{\partial(AV)}{\partial x} \quad (7.35)$$

Equation (7.35) is the conservation form of the energy equation expressed in terms of internal energy  $e$ , suitable for quasi-one-dimensional flow. The nonconservation form is then obtained by multiplying the continuity equation, Eq. (7.15), by  $e$ ,

$$e \frac{\partial(\rho A)}{\partial t} + e \frac{\partial(\rho AV)}{\partial x} = 0 \quad (7.36)$$

and subtracting Eq. (7.36) from Eq. (7.35), yielding

$$\rho A \frac{\partial e}{\partial t} + \rho AV \frac{\partial e}{\partial x} = -p \frac{\partial(AV)}{\partial x} \quad (7.37)$$

Expanding the right-hand side and dividing by  $A$ , Eq. (7.37) becomes

$$\rho \frac{\partial e}{\partial t} + \rho V \frac{\partial e}{\partial x} = -p \frac{\partial V}{\partial x} - p \frac{V}{A} \frac{\partial A}{\partial x}$$

or

$$\rho \frac{\partial e}{\partial t} + \rho V \frac{\partial e}{\partial x} = -p \frac{\partial V}{\partial x} - p V \frac{\partial(\ln A)}{\partial x} \quad (7.38)$$

Equation (7.38) is the nonconservation form of the energy equation expressed in terms of internal energy, appropriate to unsteady, quasi-one-dimensional flow.

The reason for obtaining the energy equation in the form of Eq. (7.38) is that, for a calorically perfect gas, it leads directly to a form of the energy equation in terms of temperature  $T$ . For our solution of the quasi-one-dimensional nozzle flow of a calorically perfect gas, this is a fundamental variable, and therefore it is convenient

to deal with it as the primary dependent variable in the energy equation. For a calorically perfect gas

$$e = c_v T$$

Hence, Eq. (7.38) becomes

$$\rho c_v \frac{\partial T}{\partial t} + \rho V c_v \frac{\partial T}{\partial x} = -p \frac{\partial V}{\partial x} - pV \frac{\partial(\ln A)}{\partial x} \quad (7.39)$$

As an interim summary, our continuity, momentum, and energy equations for unsteady, quasi-one-dimensional flow are given by Eqs. (7.15), (7.27), and (7.39), respectively. Take the time to look at these equations; you see three equations with four unknown variables  $\rho$ ,  $V$ ,  $p$ , and  $T$ . The pressure can be eliminated from these equations by using the equation of state

$$p = \rho R T \quad (7.40)$$

along with its derivative

$$\frac{\partial p}{\partial x} = R \left( \rho \frac{\partial T}{\partial x} + T \frac{\partial \rho}{\partial x} \right) \quad (7.41)$$

With this, we expand Eq. (7.15) and rewrite Eqs. (7.27) and (7.39), respectively, as

$$\text{Continuity : } \frac{\partial(\rho A)}{\partial t} + \rho A \frac{\partial V}{\partial x} + \rho V \frac{\partial A}{\partial x} + VA \frac{\partial \rho}{\partial x} = 0 \quad (7.42)$$

$$\text{Momentum : } \rho \frac{\partial V}{\partial t} + \rho V \frac{\partial V}{\partial x} = -R \left( \rho \frac{\partial T}{\partial x} + T \frac{\partial \rho}{\partial x} \right) \quad (7.43)$$

$$\text{Energy : } \rho c_v \frac{\partial T}{\partial t} + \rho V c_v \frac{\partial T}{\partial x} = -\rho R T \left[ \frac{\partial V}{\partial x} + V \frac{\partial(\ln A)}{\partial x} \right] \quad (7.44)$$

At this stage, we could readily proceed to set up our numerical solution of Eqs. (7.42) to (7.44). Note that these are written in terms of dimensional variables. This is fine, and many CFD solutions are carried out directly in terms of such dimensional variables. Indeed, this has an added engineering advantage because it gives you a feeling for the magnitudes of the real physical quantities as the solution progresses. However, for nozzle flows, the flow-field variables are frequently expressed in terms of nondimensional variables, such as those sketched in Fig. 7.2, where the flow variables are referenced to their reservoir values. The nondimensional variables  $p/p_0$ ,  $\rho/\rho_0$ , and  $T/T_0$  vary between 0 and 1, which is an “aesthetic” advantage when presenting the results. Because fluid dynamicists dealing with nozzle flows so frequently use these nondimensional terms, we will follow suit here. (A number of CFD practitioners prefer to always deal with nondimensional variables, whereas others prefer dimensional variables; as far as the numerics are concerned, there should be no real difference, and the choice is really a matter of your personal preference.) Therefore, returning to Fig. 7.1, where the

reservoir temperature and density are denoted by  $T_0$  and  $\rho_0$ , respectively, we define the nondimensional temperature and density, respectively, as

$$T' = \frac{T}{T_0} \quad \rho' = \frac{\rho}{\rho_0}$$

where (for the time being) the prime denotes a dimensionless variable. Moreover, letting  $L$  denote the length of the nozzle, we define a dimensionless length as

$$x' = \frac{x}{L}$$

Denoting the speed of sound in the reservoir as  $a_0$ , where

$$a_0 = \sqrt{\gamma R T_0}$$

we define a dimensionless velocity as

$$V' = \frac{V}{a_0}$$

Also, the quantity  $L/a_0$  has the dimension of time, and we define a dimensionless time as

$$t' = \frac{t}{L/a_0}$$

Finally, we ratio the local area  $A$  to the sonic throat area  $A^*$  and define a dimensionless area as

$$A' = \frac{A}{A^*}$$

Returning to Eq. (7.42) and introducing the nondimensional variables, we have

$$\begin{aligned} \frac{\partial(\rho' A')}{\partial t'} \left( \frac{\rho_0 A^*}{L/a_0} \right) + \rho' A' \frac{\partial V'}{\partial x'} \left( \frac{\rho_0 A^* a_0}{L} \right) + \rho' V' \frac{\partial A'}{\partial x'} \left( \frac{\rho_0 a_0 A^*}{L} \right) \\ + V' A' \frac{\partial \rho'}{\partial x'} \left( \frac{a_0 A^* \rho_0}{L} \right) = 0 \end{aligned} \quad (7.45)$$

Note that  $A'$  is a function of  $x'$  only; it is *not* a function of time (the nozzle geometry is fixed, invariant with time). Hence, in Eq. (7.45) the time derivative can be written as

$$\frac{\partial(\rho' A')}{\partial t'} = A' \frac{\partial \rho'}{\partial t'}$$

With this, Eq. (7.45) becomes

*Continuity :*

$$\frac{\partial \rho'}{\partial t'} = -\rho' \frac{\partial V'}{\partial x'} - \rho' V' \frac{\partial(\ln A')}{\partial x'} - V' \frac{\partial \rho'}{\partial x'} \quad (7.46)$$

Returning to Eq. (7.43) and introducing the nondimensional variables, we have

$$\rho' \frac{\partial V'}{\partial t'} \left( \frac{\rho_0 a_0}{L/a_0} \right) + \rho' V' \frac{\partial V'}{\partial x'} \left( \frac{\rho_0 a_0^2}{L} \right) = -R \left( \rho' \frac{\partial T'}{\partial x'} + T' \frac{\partial \rho'}{\partial x'} \right) \left( \frac{\rho_0 T_0}{L} \right)$$

or

$$\rho' \frac{\partial V'}{\partial t'} = -\rho' V' \frac{\partial V'}{\partial x'} - \left( \rho' \frac{\partial T'}{\partial x'} + T' \frac{\partial \rho'}{\partial x'} \right) \frac{RT_0}{a_0^2} \quad (7.47)$$

In Eq. (7.47), note that

$$\frac{RT_0}{a_0^2} = \frac{\gamma RT_0}{\gamma a_0^2} = \frac{a_0^2}{\gamma a_0^2} = \frac{1}{\gamma}$$

Hence, Eq. (7.47) becomes

*Momentum :*

$$\frac{\partial V'}{\partial t'} = -V' \frac{\partial V'}{\partial x'} - \frac{1}{\gamma} \left( \frac{\partial T'}{\partial x'} + \frac{T'}{\rho'} \frac{\partial \rho'}{\partial x'} \right) \quad (7.48)$$

Returning to Eq. (7.44) and introducing the nondimensional variables, we have

$$\begin{aligned} \rho' c_v \frac{\partial T'}{\partial t'} \left( \frac{\rho_0 T_0}{L/a_0} \right) + \rho' V' c_v \frac{\partial T'}{\partial x'} \left( \frac{\rho_0 a_0 T_0}{L} \right) \\ = -\rho' R T' \left[ \frac{\partial V'}{\partial x'} + V' \frac{\partial(\ln A')}{\partial x'} \right] \left( \frac{\rho_0 T_0 a_0}{L} \right) \end{aligned} \quad (7.49)$$

In Eq. (7.49), the factor  $R/c_v$  is given by

$$\frac{R}{c_v} = \frac{R}{R/(\gamma - 1)} = \gamma - 1$$

Hence, Eq. (7.49) becomes

*Energy :*

$$\frac{\partial T'}{\partial t'} = -V' \frac{\partial T'}{\partial x'} - (\gamma - 1) T' \left[ \frac{\partial V'}{\partial x'} + V' \frac{\partial(\ln A')}{\partial x'} \right] \quad (7.50)$$

That is it! We are finally finished with the first eschelon as itemized at the beginning of this subsection. After what may seem like an interminable manipulation of the governing equations, we have finally set up that particular form of the equations that will be most appropriate as well as convenient for the time-marching solution of quasi-one-dimensional nozzle flow, namely, Eqs. (7.46), (7.48), and (7.50).

**THE FINITE-DIFFERENCE EQUATIONS.** We now proceed to the next eschelon, namely, the setting up of the finite-difference expressions using MacCormack's explicit technique for the numerical solution of Eqs. (7.46), (7.48), and (7.50). To implement a finite-difference solution, we divide the  $x$  axis along the nozzle into a number of discrete grid points, as shown in Fig. 7.5. (Recall that in our quasi-one-dimensional nozzle assumption, the flow variables *across* the nozzle cross section at any particular grid point, say point  $i$ , are uniform.) In Fig. 7.5, the first grid point, labeled point 1, is assumed to be in the reservoir. The points are evenly distributed along the  $x$  axis, with  $\Delta x$  denoting the spacing between grid points. The last point, namely, that at the nozzle exit, is denoted by  $N$ ; we have a total number of  $N$  grid points distributed along the axis. Point  $i$  is simply an arbitrary grid point, with points  $i - 1$  and  $i + 1$  as the adjacent points. Recall from Sec. 6.3 that MacCormack's technique is a predictor-corrector method. In the time-marching approach, remember that we know the flow-field variables at time  $t$ , and we use the difference equations to solve explicitly for the variables at time  $t + \Delta t$ .

First, consider the predictor step. Following the discussion in Sec. 6.3, we set up the spatial derivatives as forward differences. Also, to reduce the complexity of the notation, we will drop the use of the prime to denote a dimensionless variable. In what follows, *all* variables are the nondimensional variables, denoted earlier by the prime notation. Analogous to Eq. (6.17), from Eq. (7.46) we have

$$\left( \frac{\partial \rho}{\partial t} \right)_i^t = -\rho_i^t \frac{V_{i+1}^t - V_i^t}{\Delta x} - \rho_i^t V_i^t \frac{\ln A_{i+1} - \ln A_i}{\Delta x} - V_i^t \frac{\rho_{i+1}^t - \rho_i^t}{\Delta x} \quad (7.51)$$

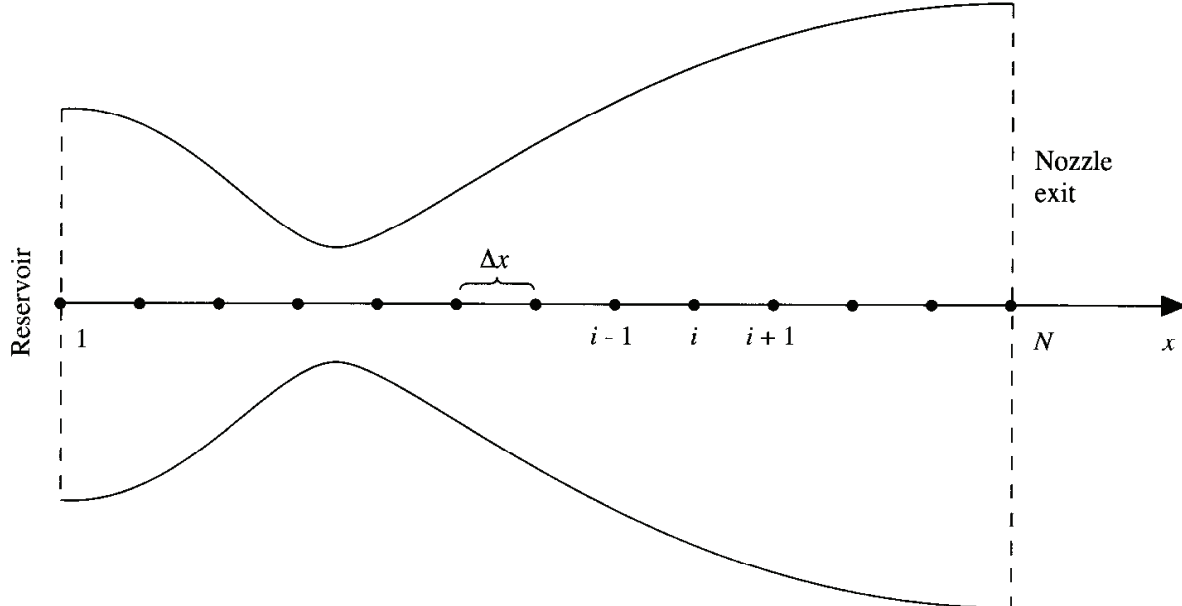


**FIG. 7.5**  
Grid point distribution along the nozzle.

From Eq. (7.48), we have

$$\left(\frac{\partial V}{\partial t}\right)_i^t = -V_i^t \frac{V_{i+1}^t - V_i^t}{\Delta x} - \frac{1}{\gamma} \left( \frac{T_{i+1}^t - T_i^t}{\Delta x} + \frac{T_i^t \rho_{i+1}^t - \rho_i^t}{\Delta x} \right) \quad (7.52)$$

From Eq. (7.50), we have

$$\left(\frac{\partial T}{\partial t}\right)_i^t = -V_i^t \frac{T_{i+1}^t - T_i^t}{\Delta x} - (\gamma - 1) T_i^t \left( \frac{V_{i+1}^t - V_i^t}{\Delta x} + V_i^t \frac{\ln A_{i+1} - \ln A_i}{\Delta x} \right) \quad (7.53)$$

Analogous to Eqs. (6.18) to (6.21), we obtain predicted values of  $\rho$ ,  $V$ , and  $T$ , denoted by barred quantities, from

$$\bar{\rho}_i^{t+\Delta t} = \rho_i^t + \left(\frac{\partial \rho}{\partial t}\right)_i^t \Delta t \quad (7.54)$$

$$\bar{V}_i^{t+\Delta t} = V_i^t + \left(\frac{\partial V}{\partial t}\right)_i^t \Delta t \quad (7.55)$$

$$\bar{T}_i^{t+\Delta t} = T_i^t + \left(\frac{\partial T}{\partial t}\right)_i^t \Delta t \quad (7.56)$$

In Eqs. (7.54) to (7.56),  $p_i^t$ ,  $V_i^t$ , and  $T_i^t$  are known values at time  $t$ . Numbers for the time derivatives in Eqs. (7.54) to (7.56) are supplied directly by Eqs. (7.51) to (7.53).

Moving to the corrector step, we return to Eqs. (7.46), (7.48), and (7.50) and replace the spatial derivatives with rearward differences, using the predicted (barred) quantities. Analogous to Eq. (6.22), we have from Eq. (7.46)

$$\begin{aligned} \left(\frac{\partial \bar{\rho}}{\partial t}\right)_i^{t+\Delta t} &= -\bar{\rho}_i^{t+\Delta t} \frac{\bar{V}_i^{t+\Delta t} - \bar{V}_{i-1}^{t+\Delta t}}{\Delta x} - \bar{\rho}_i^{t+\Delta t} \bar{V}_i^{t+\Delta t} \frac{\ln A_i - \ln A_{i-1}}{\Delta x} \\ &\quad - \bar{V}_i^{t+\Delta t} \frac{\bar{\rho}_i^{t+\Delta t} - \bar{\rho}_{i-1}^{t+\Delta t}}{\Delta x} \end{aligned} \quad (7.57)$$

From Eq. (7.48), we have

$$\begin{aligned} \left(\frac{\partial \bar{V}}{\partial t}\right)_i^{t+\Delta t} &= -\bar{V}_i^{t+\Delta t} \frac{\bar{V}_i^{t+\Delta t} - \bar{V}_{i-1}^{t+\Delta t}}{\Delta x} - \frac{1}{\gamma} \left( \frac{\bar{T}_i^{t+\Delta t} - \bar{T}_{i-1}^{t+\Delta t}}{\Delta x} + \frac{\bar{T}_i^{t+\Delta t} \bar{\rho}_i^{t+\Delta t} - \bar{\rho}_{i-1}^{t+\Delta t}}{\Delta x} \right) \end{aligned} \quad (7.58)$$

From Eq. (7.50), we have

$$\begin{aligned} \left(\frac{\partial \bar{T}}{\partial t}\right)_i^{t+\Delta t} &= -\bar{V}_i^{t+\Delta t} \frac{\bar{T}_i^{t+\Delta t} - \bar{T}_{i-1}^{t+\Delta t}}{\Delta x} - (\gamma - 1) \bar{T}_i^{t+\Delta t} \\ &\quad \times \left( \frac{\bar{V}_i^{t+\Delta t} - \bar{V}_{i-1}^{t+\Delta t}}{\Delta x} + \bar{V}_i^{t+\Delta t} \frac{\ln A_i - \ln A_{i-1}}{\Delta x} \right) \end{aligned} \quad (7.59)$$

Analogous to Eq. (6.22), the average time derivatives are given by

$$\left(\frac{\partial \rho}{\partial t}\right)_{av} = 0.5 \left[ \underbrace{\left(\frac{\partial \rho}{\partial t}\right)_i^t}_{\text{From Eq. (7.51)}} + \underbrace{\left(\frac{\partial \rho}{\partial t}\right)_i^{t+\Delta t}}_{\text{From Eq. (7.57)}} \right] \quad (7.60)$$

$$\left(\frac{\partial V}{\partial t}\right)_{av} = 0.5 \left[ \underbrace{\left(\frac{\partial V}{\partial t}\right)_i^t}_{\text{From Eq. (7.52)}} + \underbrace{\left(\frac{\partial V}{\partial t}\right)_i^{t+\Delta t}}_{\text{From Eq. (7.58)}} \right] \quad (7.61)$$

$$\left(\frac{\partial T}{\partial t}\right)_{av} = 0.5 \left[ \underbrace{\left(\frac{\partial T}{\partial t}\right)_i^t}_{\text{From Eq. (7.53)}} + \underbrace{\left(\frac{\partial T}{\partial t}\right)_i^{t+\Delta t}}_{\text{From Eq. (7.59)}} \right] \quad (7.62)$$

Finally, analogous to Eqs. (6.13) to (6.16), we have for the corrected values of the flow-field variables at time  $t + \Delta t$

$$\rho_i^{t+\Delta t} = \rho_i^t + \left(\frac{\partial \rho}{\partial t}\right)_{av} \Delta t \quad (7.63)$$

$$V_i^{t+\Delta t} = V_i^t + \left(\frac{\partial V}{\partial t}\right)_{av} \Delta t \quad (7.64)$$

$$T_i^{t+\Delta t} = T_i^t + \left(\frac{\partial T}{\partial t}\right)_{av} \Delta t \quad (7.65)$$

Keep in mind that all the variables in Eqs. (7.51) to (7.65) are the *nondimensional* values. Also, Eqs. (7.51) to (7.65) constitute our second eschelon of equations, namely, the finite-difference expressions of the governing equations in a form that pertains to MacCormack's technique.

**CALCULATION OF TIME STEP.** We now proceed to the third and final eschelon of equations mentioned at the beginning of this section, namely, the setting up of other details necessary for the numerical solution of the quasi-one-dimensional nozzle flow problem. First, we ask the question: What about the magnitude of  $\Delta t$ ? The governing system of equations, Eqs. (7.42) to (7.44), is hyperbolic with respect to time. Recalling our discussion of stability considerations in Sec. 4.5, a stability constraint exists on this system analogous to that found in Eq. (4.84), namely,

$$\Delta t = C \frac{\Delta x}{a + V} \quad (7.66)$$

Recall from Sec. 4.5 that  $C$  is the *Courant number*; the simple stability analysis of a linear hyperbolic equation carried out in Sec. 4.5 gives the result that  $C \leq 1$  for an explicit numerical solution to be stable. The present application to subsonic-supersonic isentropic nozzle flow is governed by *nonlinear* partial differential equations, namely, Eqs. (7.46), (7.48), and (7.50). In this case, the exact stability criterion for a linear equation, namely, that  $C \leq 1$ , can only be viewed as general guidance for our present nonlinear problem. However, it turns out to be quite good guidance, as we shall see. Also note that, in contrast to Eq. (4.84), Eq. (7.66) is written with the sum  $a + V$  in the denominator. Equation (7.66) is the *Courant-Friedrichs-Lowry (CFL) criterion* for a one-dimensional flow, where  $V$  is the local flow velocity at a point in the flow and  $a$  is the local speed of sound. Equation (7.66), along with  $C \leq 1$ , simply states that  $\Delta t$  must be less than, or at best equal to, the time it takes a sound wave to move from one grid point to the next. Equation (7.66) is in dimensional form. However, when  $t$ ,  $x$ ,  $a$ , and  $V$  are nondimensionalized, the nondimensional form of Eq. (7.66) is exactly the same form as the dimensional case. (Prove this to yourself.) Hence, we will hereafter treat the variables in Eq. (7.66) as our nondimensional variables defined earlier. That is, in Eq. (7.66),  $\Delta t$  is the increment in nondimensional time and  $\Delta x$  is the increment in nondimensional space;  $\Delta t$  and  $\Delta x$  in Eq. (7.66) are precisely the same as appear in the nondimensional equations (7.51) to (7.65). Examining Eq. (7.66) more carefully, we note that, although  $\Delta x$  is the same throughout the flow, both  $V$  and  $a$  are variables. Hence, at a given grid point at a given time step, Eq. (7.66) is written as

$$(\Delta t)_i^t = C \frac{\Delta x}{a_i^t + V_i^t} \quad (7.67)$$

At an adjacent grid point, we have from Eq. (7.66)

$$(\Delta)_{i+1}^t = C \frac{\Delta x}{a_{i+1}^t + V_{i+1}^t} \quad (7.68)$$

Clearly,  $(\Delta t)_i^t$  and  $(\Delta t)_{i+1}^t$  obtained from Eqs. (7.67) and (7.68), respectively are, in general, different values. Hence, in the implementation of the time-marching solution, we have two choices:

1. In utilizing Eqs. (7.54) to (7.56) and (7.63) to (7.65), we can, at each grid point  $i$ , employ the *local* values of  $(\Delta t)_i^t$  determined from Eq. (7.67). In this fashion, the flow-field variables at each grid point in Fig. 7.5 will be advanced in time according to their own, local time step. Hence, the resulting flow field at time  $t + \Delta t$  will be in a type of *artificial “time warp,”* with the flow-field variables at a given grid point corresponding to some nonphysical time different from that of the variables at an adjacent grid point. Clearly, such a *local time-stepping* approach does not realistically follow the *actual, physical transients* in the flow and hence cannot be used for an accurate solution of the *unsteady* flow. However, if the final steady-state flow field in the limit of large time is the only desired result, then the intermediate variation of the flow-field variables with time is irrelevant. Indeed, if such is the case, the *local* time stepping will frequently lead

to *faster* convergence to the steady state. This is why some practitioners use the local time-stepping approach. However, there is always a philosophical question that arises here, namely, does the *local* time-stepping method always lead to the *correct* steady state? Although the answer is usually yes, there is still some reason for a small feeling of discomfort in this regard.

2. The other choice is to calculate  $(\Delta t)_i^t$  at all the grid points,  $i = 1$  to  $i = N$ , and then choose the *minimum* value for use in Eqs. (7.54) to (7.56) and (7.63) to (7.65). That is,

$$\Delta t = \min(\Delta t_1^t, \Delta t_2^t, \dots, \Delta t_i^t, \dots, \Delta t_N^t) \quad (7.69)$$

The resulting  $\Delta t$  obtained from Eq. (7.69) is then used in Eqs. (7.54) to (7.56) and (7.63) to (7.65). In this fashion, the flow-field variables at all the grid points at time  $t + \Delta t$  all correspond to the *same* physical time. Hence, the time-marching solution is following the actual unsteady flow variations that would exist in nature; i.e., the solution gives a time-accurate solution of the actual transient flow field, consistent with the unsteady continuity, momentum, and energy equations. This consistent time marching is the approach we will use in the present book. Although it may require more time steps to approach the steady state in comparison to the “local” time stepping described earlier, we can feel comfortable that the consistent time-marching approach is giving us the physically meaningful transient variations—which frequently are of intrinsic value by themselves. Thus, in our subsequent calculations, we will use Eq. (7.69) to determine the value of  $\Delta t$ .

**BOUNDARY CONDITIONS.** Another aspect of the numerical solution is that of *boundary conditions*—an all-important aspect, because without the physically proper implementation of boundary conditions and their numerically proper representation, we have no hope whatsoever in obtaining a proper numerical solution to our flow problem. First, let us examine the physical boundary conditions for the subsonic-supersonic isentropic flow shown in Fig. 7.2, which is the subject of this section. Returning to Fig. 7.5, we note that grid points 1 and  $N$  represent the two boundary points on the  $x$  axis. Point 1 is essentially in the reservoir; it represents an *inflow* boundary, with flow coming from the reservoir and entering the nozzle. In contrast, point  $N$  is an *outflow* boundary, with flow leaving the nozzle at the nozzle exit. Moreover, the flow velocity at point 1 is a very low, subsonic value. (The flow velocity at point 1, which corresponds to a finite area ratio  $A_1/A^*$ , cannot be precisely zero; if it were, there would be no mass flow entering the nozzle. Hence, point 1 does not correspond *exactly* to the reservoir, where by definition the flow velocity is zero. That is, the area for the reservoir is theoretically infinite, and we are clearly starting our own calculation at point 1 where the cross-sectional area is finite.) Hence, not only is point 1 an *inflow* boundary, it is a *subsonic* inflow boundary. *Question:* Which flow quantities should be specified at this subsonic inflow boundary and which should be calculated as part of the solution (i.e., allowed to “float” as a function of time)? A formal answer can be obtained by using the method of characteristics for an unsteady, one-dimensional flow, as introduced in

Chap. 3. We did not develop the method of characteristics in Chap. 3 to the extent necessary to precisely study this question about the boundary conditions; indeed, such a matter is beyond the scope of this book. However, we will mention the result of such a study, which you will find to be physically acceptable. In a subsection of Sec. 3.4.1, we indicated that unsteady, inviscid flow is governed by hyperbolic equations, and therefore for one-dimensional unsteady flow there exist two real characteristic lines through any point in the  $xt$  plane. This is illustrated in Fig. 3.6; return to this figure and examine it carefully before continuing on. Note that the two characteristic lines through point  $P$  in Fig. 3.6 are labeled left- and right-running characteristics, respectively. Physically, these two characteristics represent infinitely weak Mach waves which are propagating upstream and downstream, respectively. Both Mach waves are traveling at the speed of sound  $a$ . Now turn to Fig. 7.6, which shows our convergent-divergent nozzle (Fig. 7.6a) with an  $xt$  diagram sketched below it (Fig. 7.6b). Concentrate on grid point 1 in the  $xt$  plane in Fig. 7.6b. At point

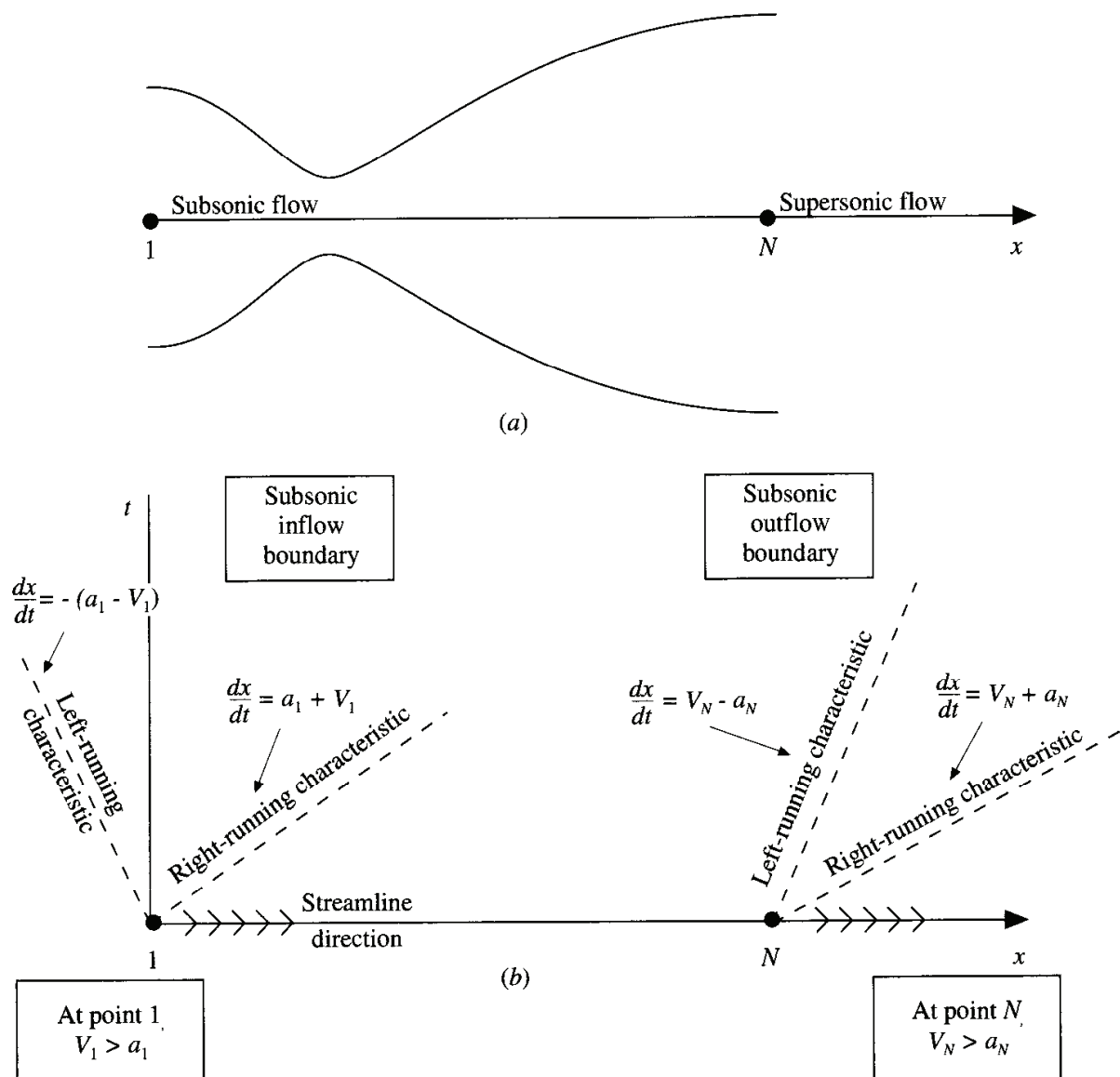


FIG. 7.6

Study of boundary conditions: subsonic inflow and supersonic outflow.

1, the local flow velocity is subsonic,  $V_1 < a_1$ . Hence, the left-running characteristic at point 1 travels *upstream*, to the left in Fig. 7.6; i.e., the left-running Mach wave, which is traveling toward the left (relative to a moving fluid element) at the speed of sound easily works its way *upstream* against the low-velocity subsonic flow, which is slowly moving from left to right. Hence, in Fig. 7.6b, we show the left-running characteristic running to the left with a combined speed  $a_1 - V_1$  (relative to the fixed nozzle in Fig. 7.6a). Since the domain for the flow field to be calculated is contained between grid points 1 and  $N$ , then at point 1 we see that the left-running characteristic is propagating *out of* the domain; it is propagating to the left, away from the domain. In contrast, the right-running characteristic, which is a Mach wave propagating to the right at the speed of sound relative to a fluid element, is clearly moving toward the right in Fig. 7.6b. This is for two reasons: (1) the fluid element at point 1 is already moving toward the right, and (2) the right-running Mach wave (characteristic) is moving toward the right at the speed of sound relative to the fluid element. Hence, the right-running characteristic is propagating to the right (relative to the nozzle) at a combined velocity of  $V_1 + a_1$ . What we see here is that the right-running characteristic is propagating from point 1 *into* the domain of the calculation.

What does all this have to do with boundary conditions? The method of characteristics tells us that at a boundary where one characteristic propagates *into* the domain, then the value of one dependent flow-field variable must be *specified* at that boundary, and if one characteristic line propagates *out of* the domain, then the value of another dependent flow-field variable must be allowed to *float* at the boundary; i.e., it must be calculated in steps of time as a function of the timewise solution of the flow field. Also, note that at point 1 a streamline flows *into* the domain, across the inflow boundary. In terms of denoting what should and should not be specified at the boundary, the streamline *direction* plays the same role as the characteristic directions; i.e., the streamline moving *into* the domain at point 1 stipulates that the value of a second flow-field variable must be *specified* at the inflow boundary. *Conclusion:* At the *subsonic inflow boundary*, we must *stipulate* the values of *two* dependent flow-field variables, whereas the value of *one* other variable must be allowed to *float*. (Please note that the above discussion has been intentionally hand-waving and somewhat intuitive; a rigorous mathematical development is deferred for your future studies, beyond the scope of this book.)

Let us apply the above ideas to the *outflow boundary*, located at grid point  $N$  in Fig. 7.6. As before, the left-running characteristic at point  $N$  propagates to the left at the speed of sound *a relative to a fluid element*. However, because the speed of the fluid element itself is supersonic, the left-running characteristic is carried *downstream* at the speed (relative to the nozzle) of  $V_N - a_N$ . The right-running characteristic at point  $N$  propagates to the right at the speed of sound *a* relative to the fluid element, and thus it is swept downstream at the speed (relative to the nozzle) of  $V_N + a_N$ . Hence, at the *supersonic outflow boundary*, we have both characteristics propagating *out of* the domain; so does the streamline at point  $N$ . Therefore, there are *no* flow-field variables which require their values to be stipulated at the supersonic outflow boundary; *all* variables must be allowed to *float* at this boundary.

The above discussion details how the inflow and outflow boundary conditions are to be handled on an *analytical* basis. The *numerical* implementation of this discussion is carried out as follows.

**Subsonic inflow boundary (point 1).** Here, we must allow one variable to float; we choose the velocity  $V_1$ , because on a physical basis we know the mass flow through the nozzle must be allowed to adjust to the proper steady state, and allowing  $V_1$  to float makes the most sense as part of this adjustment. The value of  $V_1$  changes with time and is calculated from information provided by the flow-field solution over the internal points. (The *internal* points are those *not* on a boundary, i.e., points 2 through  $N - 1$  in Fig. 7.5). We use linear extrapolation from points 2 and 3 to calculate  $V_1$ . This is illustrated in Fig. 7.7. Here, the slope of the linear extrapolation line is determined from points 2 and 3 as

$$\text{Slope} = \frac{V_3 - V_2}{\Delta x}$$

Using this slope to find  $V_1$  by linear extrapolation, we have

$$V_1 = V_2 - \frac{V_3 - V_2}{\Delta x} \Delta x$$

or

$$V_1 = 2V_2 - V_3 \quad (7.70)$$

All other flow-field variables are specified. Since point 1 is viewed as essentially the reservoir, we stipulate the density and temperature at point 1 to be their respective stagnation values,  $\rho_0$  and  $T_0$ , respectively. These are held *fixed*, independent of time. Hence, in terms of the *nondimensional* variables, we have

$$\left. \begin{array}{l} \rho_1 = 1 \\ T_1 = 1 \end{array} \right\} \text{fixed, independent of time} \quad (7.71)$$

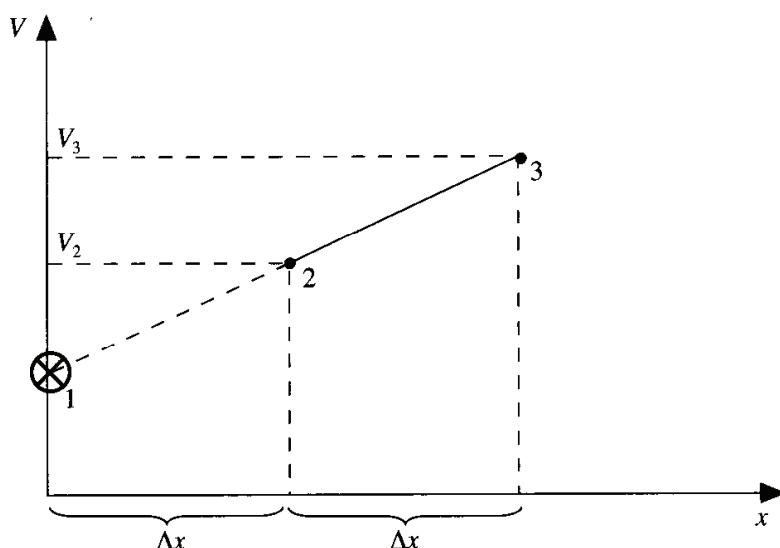


**FIG. 7.7**  
Sketch for linear extrapolation.

**Supersonic outflow boundary (point  $N$ ).** Here, we must allow *all* flow-field variables to float. We again choose to use linear extrapolation based on the flow-field values at the internal points. Specifically, we have, for the *nondimensional* variables,

$$V_N = 2V_{N-1} - V_{N-2} \quad (7.72a)$$

$$\rho_N = 2\rho_{N-1} - \rho_{N-2} \quad (7.72b)$$

$$T_N = 2T_{N-1} - T_{N-2} \quad (7.72c)$$

**NOZZLE SHAPE AND INITIAL CONDITIONS.** The nozzle shape,  $A = A(x)$ , is specified and held fixed, independent of time. For the case illustrated in this section, we choose a parabolic area distribution given by

$$A = 1 + 2.2(x - 1.5)^2 \quad 0 \leq x \leq 3 \quad (7.73)$$

Note that  $x = 1.5$  is the throat of the nozzle, that the convergent section occurs for  $x < 1.5$ , and that the divergent section occurs for  $x > 1.5$ . This nozzle shape is drawn to scale in Fig. 7.8.

To start the time-marching calculations, we must stipulate *initial* conditions for  $\rho$ ,  $T$ , and  $V$  as a function of  $x$ ; that is, we must set up values of  $\rho$ ,  $T$ , and  $V$  at time  $t = 0$ . In *theory*, these initial conditions can be purely arbitrary. In practice, there are

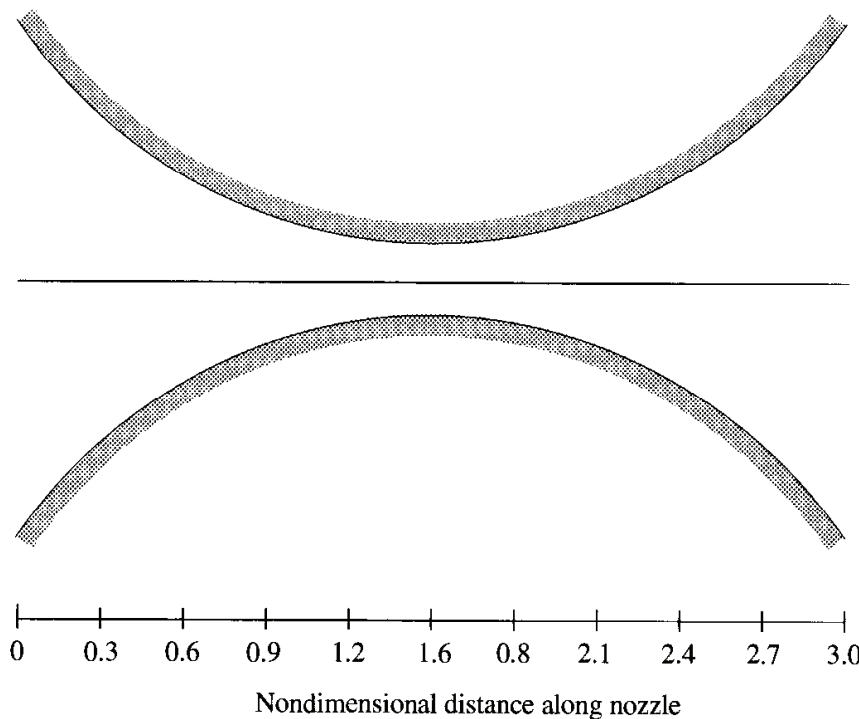


FIG. 7.8

Shape of the nozzle used for the present calculations. This geometric picture is not unique; for a calorically perfect gas, what is germane is the area ratio distribution along the nozzle. Hence, assuming a two-dimensional nozzle, the ordinates of the shape shown here can be ratioed by any constant factor, and the nozzle solution would be the same.

two reasons why you want to choose the initial conditions *intelligently*:

1. The closer the initial conditions are to the final steady-state answer, the faster the time-marching procedure will converge, and hence the shorter will be the computer execution time.
2. If the initial conditions are too far away from reality, the initial timewise gradients at early time steps can become huge; i.e., the *time derivatives* themselves are initially very large. For a given time step  $\Delta t$  and a given spatial resolution  $\Delta x$ , it has been the author's experience that *inordinately* large gradients during the early part of the time-stepping procedure can cause the program to go unstable. In a sense, you can visualize the behavior of a time-marching solution as a stretched rubber band. At early times, the rubber band is highly stretched, thus providing a *strong* potential to push the flow field *rapidly* toward the steady-state solution. As time progresses, the flow field gets closer to the steady-state solution, and the rubber band progressively relaxes, hence slowing down the rate of approach [i.e., at larger times, the values of the time derivatives calculated from Eqs. (7.60) to (7.62) become progressively smaller]. At the beginning of the calculation, it is wise not to pick initial conditions which are so far off that the rubber band is "stretched too far," and may even break.

Therefore, in your choice of initial conditions, you are encouraged to use *any* knowledge you may have about a given problem in order to intelligently pick some initial conditions. For example, in the present problem, we know that  $\rho$  and  $T$  *decrease* and  $V$  *increases* as the flow expands through the nozzle. Hence, we choose initial conditions that *qualitatively* behave in the same fashion. For simplicity, let us assume linear variations of the flow-field variables, as a function of  $x$ . For the present case, we assume the following values at time  $t = 0$ .

$$\rho = 1 - 0.3146x \quad \left. \begin{array}{l} \\ \\ \end{array} \right\} \text{initial conditions at } t = 0 \quad (7.74a)$$

$$T = 1 - 0.2314x \quad \left. \begin{array}{l} \\ \\ \end{array} \right\} \text{initial conditions at } t = 0 \quad (7.74b)$$

$$V = (0.1 + 1.09x)T^{1/2} \quad \left. \begin{array}{l} \\ \\ \end{array} \right\} \text{initial conditions at } t = 0 \quad (7.74c)$$

### 7.3.2 Intermediate Numerical Results: The First Few Steps

In this section, we give a few numerical results which reflect the first stages of the calculation. This is to give you a more solid impression of what is going on and to provide some intermediate results for you to compare with when you write and run your own computer solution to this problem.

The first step is to feed the nozzle shape and the initial conditions into the program. These are given by Eqs. (7.73) and (7.74); the resulting numbers are tabulated in Table 7.1. The values of  $\rho$ ,  $V$ , and  $T$  given in this table are for  $t = 0$ .

The next step is to put these initial conditions into Eqs. (7.51) to (7.53) to initiate calculations pertaining to the predictor step. For purposes of illustration, let us return to the sketch shown in Fig. 7.5 and focus on the calculations associated

**TABLE 7.1**  
Nozzle shape and initial conditions

$\frac{x}{L}$	$\frac{A}{A^*}$	$\frac{\rho}{\rho_0}$	$\frac{V}{a_0}$	$\frac{T}{T_0}$
0	5.950	1.000	0.100	1.000
0.1	5.312	0.969	0.207	0.977
0.2	4.718	0.937	0.311	0.954
0.3	4.168	0.906	0.412	0.931
0.4	3.662	0.874	0.511	0.907
0.5	3.200	0.843	0.607	0.884
0.6	2.782	0.811	0.700	0.861
0.7	2.408	0.780	0.790	0.838
0.8	2.078	0.748	0.877	0.815
0.9	1.792	0.717	0.962	0.792
1.0	1.550	0.685	1.043	0.769
1.1	1.352	0.654	1.122	0.745
1.2	1.198	0.622	1.197	0.722
1.3	1.088	0.591	1.268	0.699
1.4	1.022	0.560	1.337	0.676
1.5	1.000	0.528	1.402	0.653
1.6	1.022	0.497	1.463	0.630
1.7	1.088	0.465	1.521	0.607
1.8	1.198	0.434	1.575	0.583
1.9	1.352	0.402	1.625	0.560
2.0	1.550	0.371	1.671	0.537
2.1	1.792	0.339	1.713	0.514
2.2	2.078	0.308	1.750	0.491
2.3	2.408	0.276	1.783	0.468
2.4	2.782	0.245	1.811	0.445
2.5	3.200	0.214	1.834	0.422
2.6	3.662	0.182	1.852	0.398
2.7	4.168	0.151	1.864	0.375
2.8	4.718	0.119	1.870	0.352
2.9	5.312	0.088	1.870	0.329
3.0	5.950	0.056	1.864	0.306

with grid point  $i$ . We will choose  $i = 16$ , which is the grid point at the throat of the nozzle drawn in Fig. 7.8. From the initial data given in Table 7.1, we have

$$\begin{aligned}
 \rho_i &= \rho_{16} = 0.528 \\
 \rho_{i+1} &= \rho_{17} = 0.497 \\
 V_i &= V_{16} = 1.402 \\
 V_{i+1} &= V_{17} = 1.463 \\
 T_i &= T_{16} = 0.653 \\
 T_{i+1} &= T_{17} = 0.630 \\
 \Delta x &= 0.1 \\
 A_i &= A_{16} = 1.0 \quad \ln A_{16} = 0 \\
 A_{i+1} &= A_{17} = 1.022 \quad \ln A_{17} = 0.02176
 \end{aligned}$$

Substitute these values into Eq. (7.51).

$$\begin{aligned} \left( \frac{\partial \rho}{\partial t} \right)_{16}^{t=0} &= -0.528 \left( \frac{1.463 - 1.402}{0.1} \right) - 0.528(1.402) \left( \frac{0.02176 - 0}{0.1} \right) \\ &\quad - 1.402 \left( \frac{0.497 - 0.528}{0.1} \right) \\ &= \boxed{-0.0445} \end{aligned}$$

Substitute the above values into Eq. (7.52)

$$\begin{aligned} \left( \frac{\partial V}{\partial t} \right)_{16}^{t=0} &= -1.402 \left( \frac{1.463 - 1.402}{0.1} \right) \\ &\quad - \frac{1}{1.4} \left[ \frac{0.630 - 0.653}{0.1} + \frac{0.653}{0.528} \left( \frac{0.497 - 0.528}{0.1} \right) \right] \\ &= \boxed{-0.418} \end{aligned}$$

Substitute the above values into Eq. (7.53).

$$\begin{aligned} \left( \frac{\partial T}{\partial t} \right)_{16}^{t=0} &= -1.402 \left( \frac{0.630 - 0.653}{0.1} \right) - (1.4 - 1)(0.653) \\ &\quad \times \left[ \frac{1.463 - 1.402}{0.1} + 1.402 \left( \frac{0.02176 - 0}{0.1} \right) \right] \\ &= \boxed{0.0843} \end{aligned}$$

*Please note:* The numbers shown in the boxes above are the precise numbers, rounded to three significant figures, that came out of the author's Macintosh computer. If you choose to run through the above calculations with your hand calculator using all the above entries, there will be slight differences because the numbers you feed into the calculator are *already* rounded to three significant figures, and hence the subsequent arithmetic operations on your calculator will lead to slight errors compared to the computer results. That is, your hand-calculator results may not always give you *precisely* the numbers you will find in the boxes, but they will certainly be close enough to check the results.

The next step is to calculate the *predicted* values (the "barred" quantities) from Eqs. (7.54) to (7.56). To do this, we first note that  $\Delta t$  is calculated from Eq. (7.69), which picks the minimum value of  $\Delta t_i$  from all those calculated from Eq. (7.67) evaluated for all internal points  $i = 2, 3, \dots, 30$ . We do not have the space to show all these calculations here. As a sample calculation, let us calculate  $(\Delta t)_{16}^{t=0}$  from Eq. (7.67). At present, we will assume a Courant number equal to 0.5; that is,  $C = 0.5$ . Also, in nondimensional terms, the speed of sound is given by

$$a = \sqrt{T} \tag{7.75}$$

where in Eq. (7.75) both  $a$  and  $T$  are the *nondimensional* values ( $a$  denotes the local speed of sound divided by  $a_0$ ). Derive Eq. (7.75) for yourself. Thus, from Eq. (7.67), we have

$$(\Delta t)_{16}^{t=0} = C \left[ \frac{\Delta x}{(T_{16})^{1/2} + V_{16}} \right] = 0.5 \left[ \frac{0.1}{(0.653)^{1/2} + 1.402} \right] = 0.0226$$

This type of calculation is made at all the interior grid points, and the minimum value is chosen. The resulting minimum value is

$$\Delta t = 0.0201$$

With this, we can calculate  $\bar{\rho}$ ,  $\bar{V}$ , and  $\bar{T}$  as follows. From Eq. (7.54), noting that  $t = 0 + \Delta t = \Delta t$ ,

$$\begin{aligned} \bar{\rho}_{16}^{t=\Delta t} &= \rho_{16}^{t=0} + \left( \frac{\partial \rho}{\partial t} \right)_{16}^{t=0} \Delta t = 0.528 + (-0.0445)(0.0201) \\ &= \boxed{0.527} \end{aligned}$$

From Eq. (7.55)

$$\begin{aligned} \bar{V}_{16}^{t=\Delta t} &= V_{16}^{t=0} + \left( \frac{\partial V}{\partial t} \right)_{16}^{t=0} \Delta t = 1.402 + (-0.418)(0.0201) \\ &= \boxed{1.39} \end{aligned}$$

From Eq. (7.56)

$$\begin{aligned} \bar{T}_{16}^{t=\Delta t} &= T_{16}^{t=0} + \left( \frac{\partial T}{\partial t} \right)_{16}^{t=0} \Delta t = 0.653 + (0.0843)(0.0201) \\ &= \boxed{0.655} \end{aligned}$$

At this stage, we note that the above calculations are carried out over *all* the internal grid points  $i = 2$  to 30. The calculations are too repetitive to include here. Simply note that when the predictor step is completed, we have  $\bar{\rho}$ ,  $\bar{V}$ , and  $\bar{T}$  at all the internal grid points  $i = 2$  to 30. This includes, of course,  $\bar{\rho}_{15}^{t=\Delta t}$ ,  $\bar{V}_{15}^{t=\Delta t}$ , and  $\bar{T}_{15}^{t=\Delta t}$ . Focusing again on grid point 16, we now insert these *barred* quantities at grid points 15 and 16 into Eqs. (7.57) to (7.59). This is the beginning of the corrector step. From Eq. (7.57) we have

$$\begin{aligned} \left( \overline{\frac{\partial \rho}{\partial t}} \right)_{16}^{t=\Delta t} &= -0.527(0.653) - 0.527(1.39)(-0.218) - 1.39(-0.368) \\ &= \boxed{0.328} \end{aligned}$$

From Eq. (7.58) we have

$$\begin{aligned} \left( \overline{\frac{\partial V}{\partial t}} \right)_{16}^{t=\Delta t} &= -1.39(0.653) - \frac{1}{1.4} \left( -0.257 + \frac{0.655}{0.527} \right) = \boxed{-0.400} \end{aligned}$$

From Eq. (7.59) we have

$$\left( \frac{\partial \bar{T}}{\partial t} \right)_{16}^{t=\Delta t} = -1.39(-0.257) - (1.4 - 1)(0.655)[0.653 + 1.39(-0.218)] \\ = \boxed{0.267}$$

With these values, we form the *average* time derivatives using Eqs. (7.60) to (7.62). From Eq. (7.60), we have at grid point  $i = 16$ ,

$$\left( \frac{\partial \rho}{\partial t} \right)_{av} = 0.5(-0.0445 + 0.328) = \boxed{0.142}$$

From Eq. (7.61), we have at grid point  $i = 16$ ,

$$\left( \frac{\partial V}{\partial t} \right)_{av} = 0.5(-0.418 + 0.400) = \boxed{-0.409}$$

From Eq. (7.62), we have at grid point  $i = 16$ ,

$$\left( \frac{\partial T}{\partial t} \right)_{av} = 0.5(0.0843 + 0.267) = \boxed{0.176}$$

We now complete the corrector step by using Eqs. (7.63) to (7.65). From Eq. (7.63), we have at  $i = 16$ ,

$$\rho_{16}^{t=\Delta t} = 0.528 + 0.142(0.0201) = \boxed{0.531}$$

From Eq. (7.64), we have at  $i = 16$ ,

$$V_{16}^{t=\Delta t} = 1.402 + (-0.409)(0.0201) = \boxed{1.394}$$

From Eq. (7.65), we have at  $i = 16$ ,

$$T_{16}^{t=\Delta t} = 0.653 + 0.176(0.0201) = \boxed{0.656}$$

Defining a nondimensional pressure as the local static pressure divided by the reservoir pressure  $p_0$ , the equation of state is given by

$$p = \rho T$$

where  $p$ ,  $\rho$ , and  $T$  are *nondimensional* values. Thus, at grid point  $i = 16$ , we have

$$p_{16}^{t=\Delta t} = \rho_{16}^{t=\Delta t} T_{16}^{t=\Delta t} = 0.531(0.656) = \boxed{0.349}$$

*This now completes the corrector step for grid point  $i = 16$ . When the above corrector-step calculations are carried out for all grid points from  $i = 2$  to 30, then we have completed the corrector step for all the *internal* grid points.*

It remains to calculate the flow-field variables at the boundary points. At the subsonic inflow boundary ( $i = 1$ ),  $V_1$  is calculated by linear extrapolation from grid

points 2 and 3. At the end of the corrector step, from a calculation identical to that given above, the values of  $V_2$  and  $V_3$  at time  $t = \Delta t$  are  $V_2 = 0.212$  and  $V_3 = 0.312$ . Thus, from Eq. (7.70), we have

$$V_1 = 2V_2 - V_3 = 2(0.212) - 0.312 = \boxed{0.111}$$

At the supersonic outflow boundary ( $i = 31$ ) all the flow-field variables are calculated by linear extrapolation from Eqs. (7.72a) to (7.72c). At the end of the corrector step, from a calculation identical to that given above,  $V_{29} = 1.884$ ,  $V_{30} = 1.890$ ,  $\rho_{29} = 0.125$ ,  $\rho_{30} = 0.095$ ,  $T_{29} = 0.354$ , and  $T_{30} = 0.332$ . When these values are inserted into Eqs. (7.72a) to (7.72c), we have

$$V_{31} = 2V_{30} - V_{29} = 2(1.890) - 1.884 = \boxed{1.895}$$

$$\rho_{31} = 2\rho_{30} - \rho_{29} = 2(0.095) - 0.125 = \boxed{0.066}$$

$$T_{31} = 2T_{30} - T_{29} = 2(0.332) - 0.354 = \boxed{0.309}$$

With this, we have completed the calculation of all the flow-field variables at all the grid points after the first time step, i.e., at time  $t = \Delta t$ . A tabulation of these variables is given in Table 7.2. Note that the Mach number is included in this tabulation. In terms of the nondimensional velocity and temperature, the Mach number (which is already a dimensionless parameter defined as the local velocity divided by the local speed of sound) is given by

$$M = \frac{V}{\sqrt{T}} \quad (7.76)$$

Examine Table 7.2 closely. By reading across the line labeled  $I = 16$ , you will find the familiar numbers that we have generated for grid point  $i = 16$  in the above discussion. Take the time to make this comparison. The entries for all other internal grid points are calculated in a like manner. Also note the values at the boundary points, labeled  $I = 1$  and  $I = 31$  in Table 7.2. You will find the numbers to be the same as discussed above.

### 7.3.3 Final Numerical Results: The Steady-State Solution

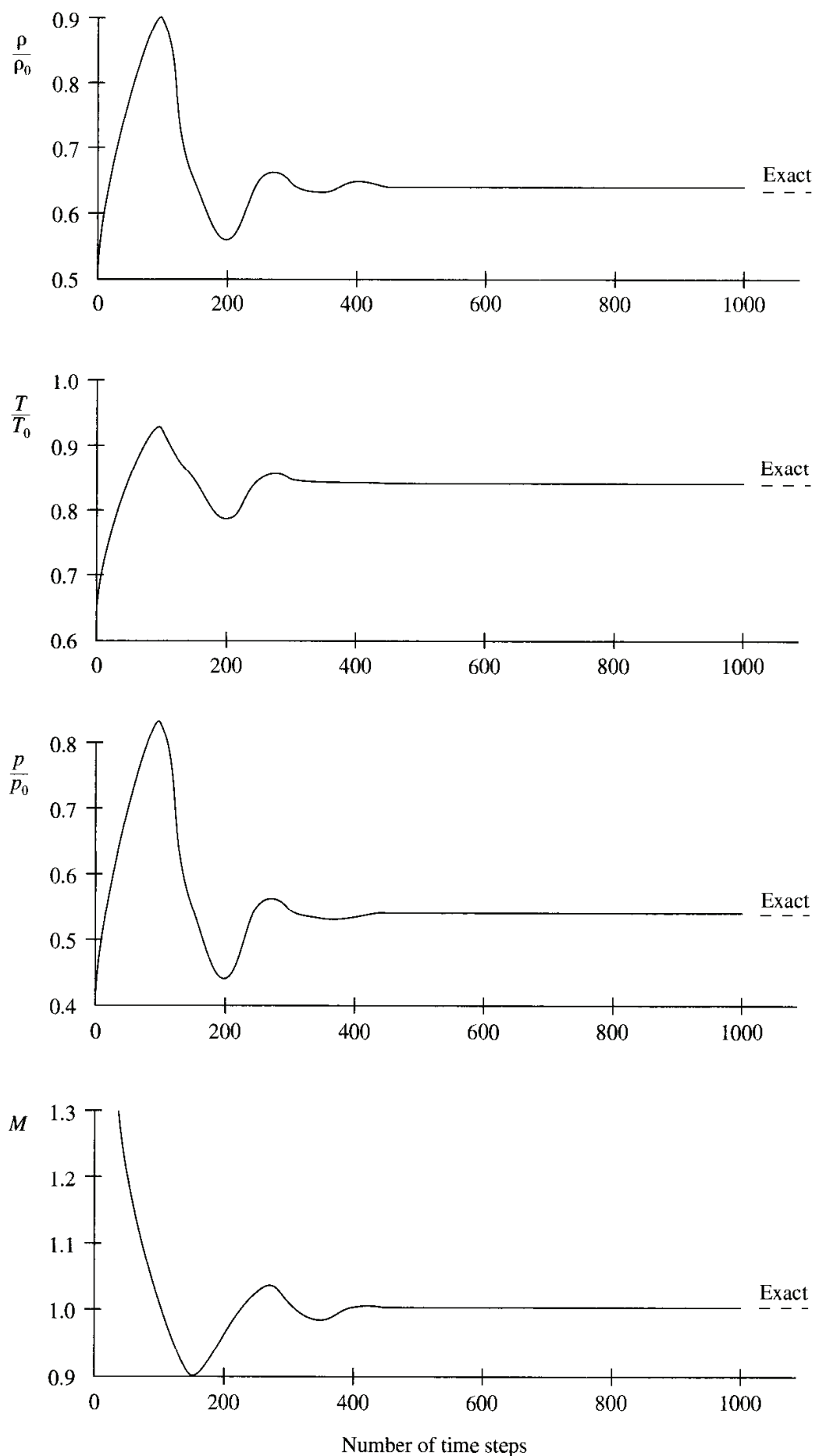
Compare the flow-field results obtained after one time step (Table 7.2) with the same quantities at the previous time (in this case the initial conditions given in Table 7.1). Comparing these two tables, we see that the flow-field variables *have changed*. For example, the nondimensional density at the throat (where  $A = 1$ ) has changed from 0.528 to 0.531, a 0.57 percent change over one time step. This is the natural behavior of a time-marching solution—the flow-field variables change from one time step to the next. However, in the approach toward the steady-state solution, at larger values of time (after a large number of time steps), the *changes* in the flow-field variables from one time step to the next become smaller and approach zero in

**TABLE 7.2**  
Flow-field variables after the first time step

<i>I</i>	$\frac{x}{L}$	$\frac{A}{A^*}$	$\frac{\rho}{\rho_0}$	$\frac{V}{a_0}$	$\frac{T}{T_0}$	$\frac{p}{p_0}$	<i>M</i>
1	0.000	5.950	1.000	0.111	1.000	1.000	0.111
2	0.100	5.312	0.955	0.212	0.972	0.928	0.215
3	0.200	4.718	0.927	0.312	0.950	0.881	0.320
4	0.300	4.168	0.900	0.411	0.929	0.836	0.427
5	0.400	3.662	0.872	0.508	0.908	0.791	0.534
6	0.500	3.200	0.844	0.603	0.886	0.748	0.640
7	0.600	2.782	0.817	0.695	0.865	0.706	0.747
8	0.700	2.408	0.789	0.784	0.843	0.665	0.854
9	0.800	2.078	0.760	0.870	0.822	0.625	0.960
10	0.900	1.792	0.731	0.954	0.800	0.585	1.067
11	1.000	1.550	0.701	1.035	0.778	0.545	1.174
12	1.100	1.352	0.670	1.113	0.755	0.506	1.281
13	1.200	1.198	0.637	1.188	0.731	0.466	1.389
14	1.300	1.088	0.603	1.260	0.707	0.426	1.498
15	1.400	1.022	0.567	1.328	0.682	0.387	1.609
16	1.500	1.000	0.531	1.394	0.656	0.349	1.720
17	1.600	1.022	0.494	1.455	0.631	0.312	1.833
18	1.700	1.088	0.459	1.514	0.605	0.278	1.945
19	1.800	1.198	0.425	1.568	0.581	0.247	2.058
20	1.900	1.352	0.392	1.619	0.556	0.218	2.171
21	2.000	1.550	0.361	1.666	0.533	0.192	2.282
22	2.100	1.792	0.330	1.709	0.510	0.168	2.393
23	2.200	2.078	0.301	1.748	0.487	0.146	2.504
24	2.300	2.408	0.271	1.782	0.465	0.126	2.614
25	2.400	2.782	0.242	1.813	0.443	0.107	2.724
26	2.500	3.200	0.213	1.838	0.421	0.090	2.834
27	2.600	3.662	0.184	1.858	0.398	0.073	2.944
28	2.700	4.168	0.154	1.874	0.376	0.058	3.055
29	2.800	4.718	0.125	1.884	0.354	0.044	3.167
30	2.900	5.312	0.095	1.890	0.332	0.032	3.281
31	3.000	5.950	0.066	1.895	0.309	0.020	3.406

the limit of large time. At this stage, the steady state (for all practical purposes) has been achieved, and the calculation can be stopped. This termination of the calculation can be done automatically by the computer program itself by having a test in the program to sense when the changes in the flow-field variables become smaller than some prescribed value (prescribed by you, depending on your desired accuracy of the final “steady-state” solution). Another option, and that preferred by the present author, is to simply stop the calculation after a prescribed number of time steps, look at the results, and see if they have approached the stage where the flow-field variables are not materially changing any more. If such is not the case, simply resume the calculations, and carry them out for the requisite number of time steps until you do see that the steady-state results have been reached.

What patterns do the timewise variations of the flow-field variables take? Some feeling for the answer is provided by Fig. 7.9, which shows the variation of  $\rho$ ,

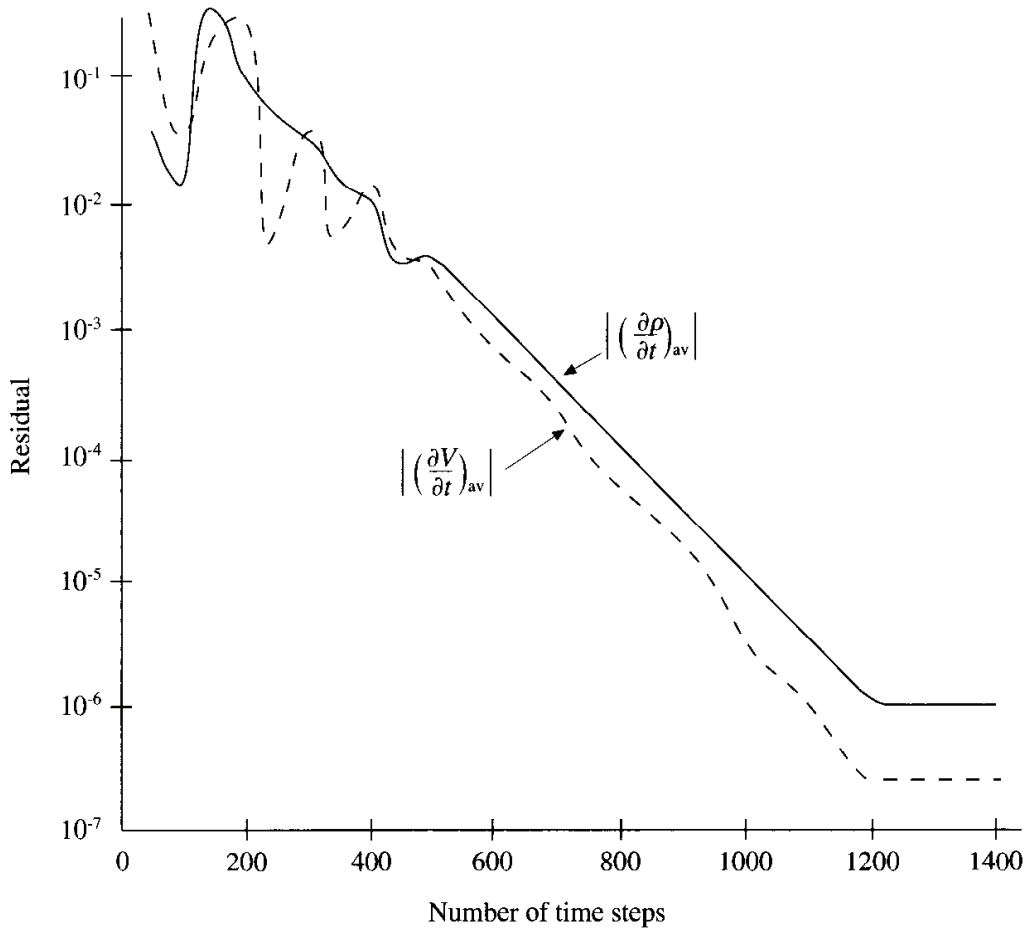


**FIG. 7.9**

Timewise variations of the density, temperature, pressure, and Mach number at the nozzle throat (at grid point  $i = 15$ , where  $A = 1$ ).

$T$ ,  $p$ , and  $M$  at the nozzle throat plotted versus the number of time steps. The abscissa starts at zero, which represents the initial conditions, and ends at time step 1000. Hence, the abscissa is essentially a time axis, with time increasing to the right. Note that the largest changes take place at early times, after which the final, steady-state value is approached almost asymptotically. Here is the “rubber band effect” mentioned previously; at early times the rubber band is “stretched” tightly, and therefore the flow-field variables are driven by a stronger potential and hence change rapidly. At later times, as the steady state is approached, the rubber band is less stretched; it becomes more “relaxed”, and the changes become much smaller with time. The dashed lines to the right of the curves shown in Fig. 7.9 represent the exact, analytical values as obtained from the equations discussed in Sec. 7.2. Note that the numerical time-marching procedure converges to the proper theoretical steady-state answer. We also note that no artificial viscosity has been explicitly added for these calculations; it is not needed.

It is interesting to examine the variation of the time derivatives as a function of time itself, or equivalently as a function of the number of time steps. Once again focusing on the nozzle throat (at grid point  $i = 16$ ), Fig. 7.10 gives the variation of the time derivatives of nondimensional density and velocity as a function of the

**FIG. 7.10**

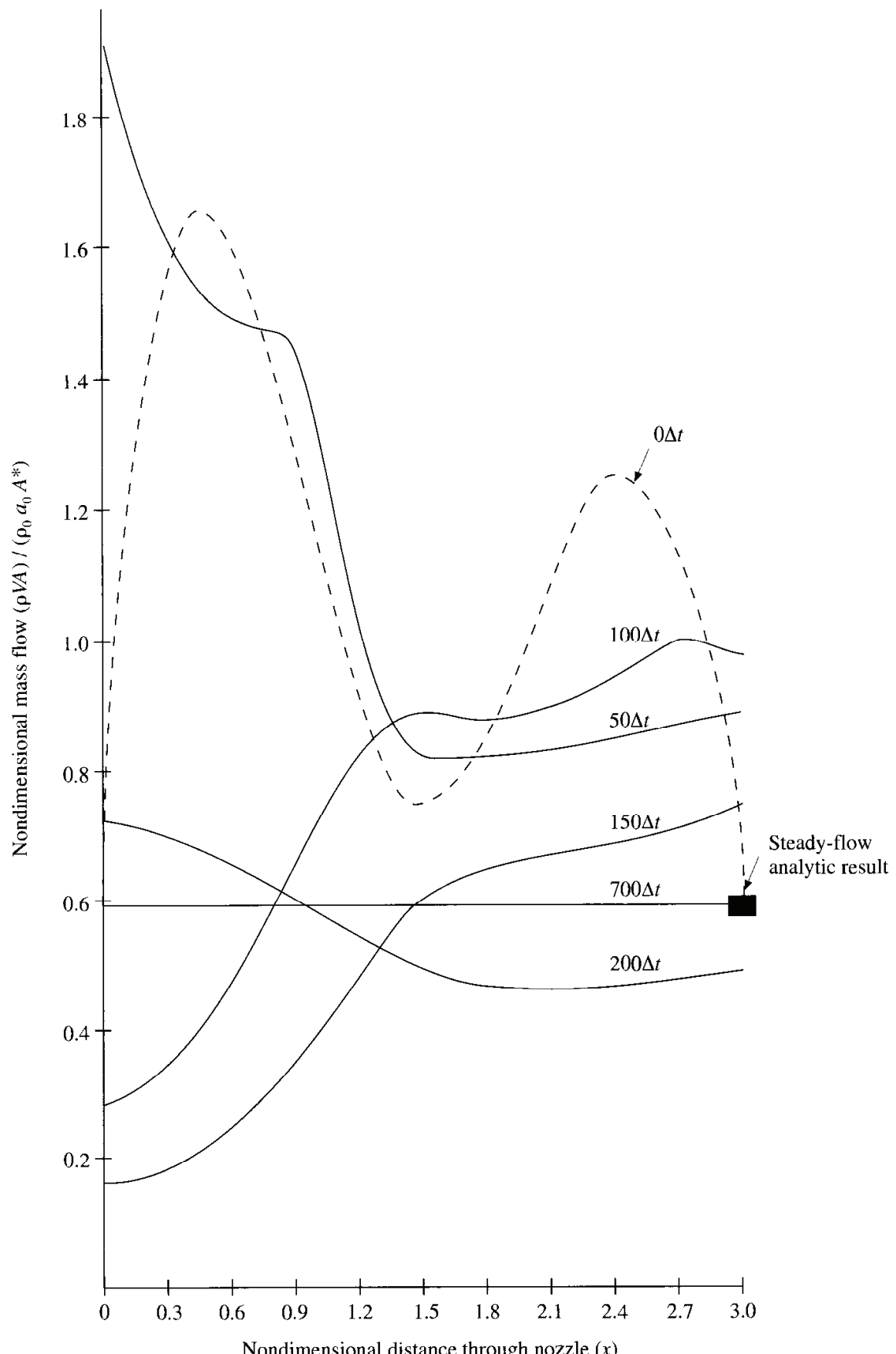
Timewise variations of the absolute values of the time derivatives of nondimensional density and velocity at the nozzle throat (at grid point  $i = 16$ ).

number of time steps. These are the *average* time derivatives calculated from Eqs. (7.60) and (7.61), respectively. The *absolute value* of these time derivatives is shown in Fig. 7.10. From these results, note two important aspects:

1. At early times, the time derivatives are large, and they oscillate in value. These oscillations are associated with various unsteady compression and expansion waves which propagate through the nozzle during the transient process. (See Chap. 7 of Ref. 21 for a discussion of unsteady wave motion in a duct.)
2. At later times, the time derivatives rapidly grow small, changing by six orders of magnitude over a span of 1000 time steps. This is, of course, what we want to see happen. In the theoretical limit of the steady state (which is achieved at infinite time), the time derivatives should go to zero. However, numerically this will never happen over a finite number of time steps. In fact, the results shown in Fig. 7.10 indicate that the values of the time derivatives plateau after 1200 time steps. This seems to be a characteristic of MacCormack's technique. However, the values of the time derivatives at these plateaus are so small that, for all practical purposes, the numerical solution has arrived at the steady-state solution. Indeed, in terms of the values of the flow-field variables themselves, the results of Fig. 7.9 indicate that the steady state is realistically achieved after 500 time steps, during which the time derivatives in Fig. 7.10 have decreased only by two orders of magnitude.

Return to Eqs. (7.46) and (7.48) for a moment; we might visualize that what is being plotted in Fig. 7.10 are the numerical values of the right-hand side of these equations. As time progresses and as the steady-state is approached, the right-hand side of these equations should approach zero. Since the *numerical* values of the right-hand side are not precisely zero, they are called *residuals*. This is why the ordinate in Fig. 7.10 is labeled as the residual. When CFD experts are comparing the relative merits of two or more different algorithms for a time-marching solution to the steady state, the magnitude of the residuals and their rate of decay are often used as figures of merit. That algorithm which gives the fastest decay of the residuals to the smallest value is usually looked upon most favorably.

Another insight to the mechanics of the timewise variation of the flow and its approach to the steady state is provided by the mass flow variations shown in Fig. 7.11. Here, the nondimensional mass flow  $\rho VA$  (where  $\rho$ ,  $V$ , and  $A$  are the nondimensional values) is plotted as a function of nondimensional distance through the nozzle. Six different curves are shown, each for a different time during the course of the time-marching procedure. The dashed curve is the variation of  $\rho VA$  which pertains to the initial conditions, and hence it is labeled  $0\Delta t$ . The strange-looking, distorted sinelike variation of this dashed curve is simply the product of the assumed initial values for  $\rho$  and  $V$  combined with the specified parabolic variation of the nozzle area ratio  $A$ . After 50 time steps, the mass flow distribution through the nozzle has changed considerably; this is given by the curve labeled  $50\Delta t$ . After 100 time steps ( $100\Delta t$ ), the mass flow distribution has changed radically; the mass flow variation is simply flopping around inside the nozzle due to

**FIG. 7.11**

Instantaneous distributions of the nondimensional mass flow as a function of distance through the nozzle at six different times during the time-marching approach to the steady state.

the transient variation of the flow-field variables. However, after 200 time steps ( $200\Delta t$ ), the mass flow distribution is beginning to settle down, and after 700 time steps ( $700\Delta t$ ), the mass flow distribution is a straight, horizontal line across the graph. This says that the mass flow has converged to a *constant*, steady-state value throughout the nozzle. This agrees with our basic knowledge of steady-state nozzle flows, namely, that

$$\rho VA = \text{constant}$$

Moreover, it has converged to essentially the *correct value* of the steady mass flow, which in terms of the *nondimensional* variables evaluated at the nozzle throat is given by

$$\rho VA = \rho^* \sqrt{T^*} \quad (\text{at throat}) \quad (7.77)$$

where  $\rho^*$  and  $T^*$  are the nondimensional density and temperature at the throat, and where  $M = 1$ . [Derive Eq. (7.77) yourself—it is easy.] From the analytical equations discussed in Sec. 7.2, when  $M = 1$  and  $\gamma = 1.4$ , we have  $\rho^* = 0.634$  and  $T^* = 0.833$ . With these numbers, Eq. (7.77) yields

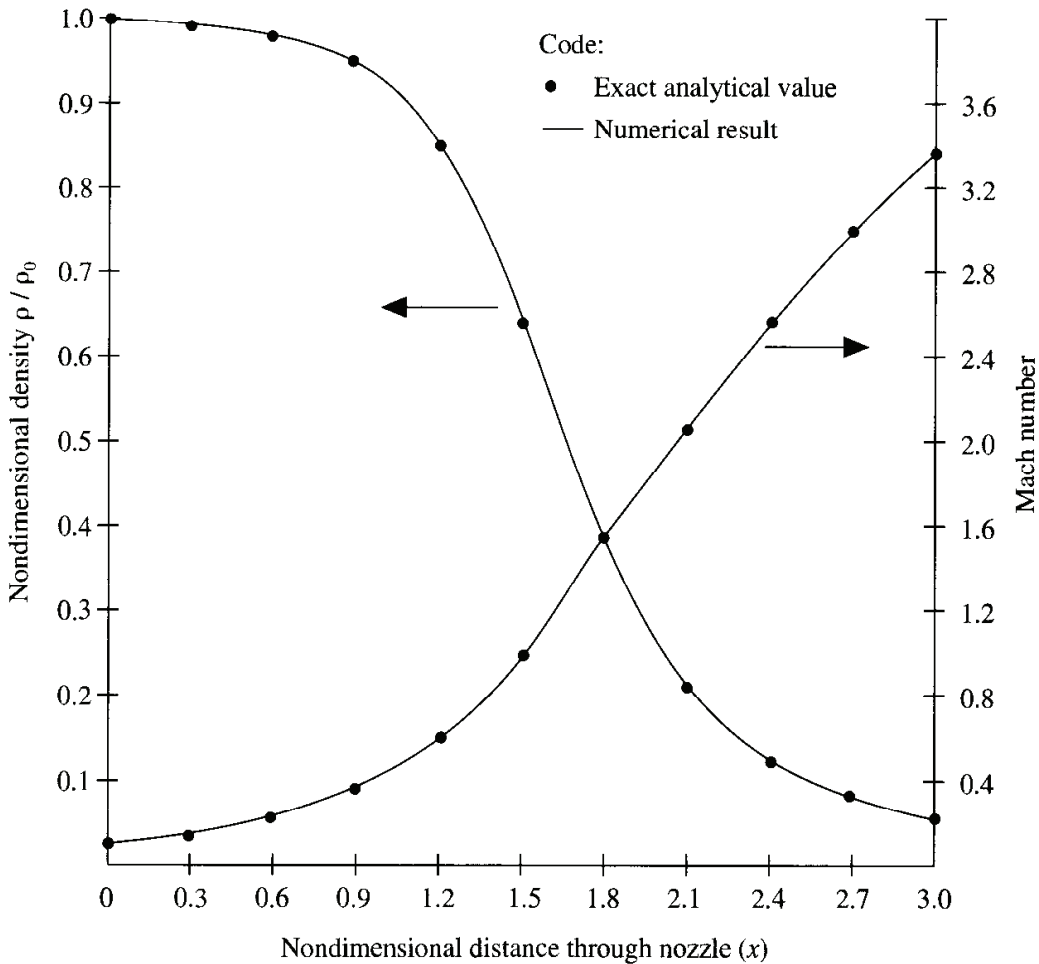
$$\rho VA = \text{constant} = 0.579$$

This value is given by the dark square in Fig. 7.11; the mass flow result for  $700\Delta t$  agrees reasonably well with the dark square.

Finally, let us examine the steady-state results. From the discussion above and from examining Fig. 7.9, the steady state is, for all practical purposes, reached after about 500 time steps. However, being very conservative, we will examine the results obtained after 1400 time steps; between 700 and 1400 time steps, there is no change in the results, at least to the three-decimal-place accuracy given in the tables herein.

A feeling for the graphical accuracy of the numerically obtained steady state is given by Fig. 7.12. Here, the steady-state nondimensional density and Mach number distributions through the nozzle are plotted as a function of nondimensional distance along the nozzle. The numerical results, obtained after 1400 time steps, are given by the solid curves, and the exact analytical results are given by the circles. The analytical results are obtained from the equations discussed in Sec. 7.2; they can readily be obtained from the tables at the back of most compressible flow texts, such as Ref. 21. They can also be obtained by writing your own short computer program to calculate numbers from the theoretically derived equations in Sec. 7.2. In any event, the comparison shown in Fig. 7.12 clearly demonstrates that the numerical results agree very well with the exact analytical values, certainly to within graphical accuracy.

The detailed numerical results, to three decimal places, are tabulated in Table 7.3. These are the results obtained after 1400 time steps. They are given here for you to compare numbers from your own computer program. It is interesting to note that the elapsed nondimensional time, starting at zero with the initial conditions, is, after 1400 time steps, a value of 28.952. Since time is nondimensionalized by the quantity  $L/a_0$ , let us assume a case where the length of the nozzle is 1 m and the reservoir temperature is the standard sea level value,  $T = 288$  K. For this case,  $L/a_0 = (1 \text{ m})/(340.2 \text{ m/s}) = 2.94 \times 10^{-3} \text{ s}$ . Hence, the total *real* time that has

**FIG. 7.12**

Steady-state distributions of nondimensional density and Mach number as a function of nondimensional distance through the nozzle. Comparison between the exact analytical values (circles) and the numerical results (solid curves).

elapsed over the 1400 time steps is  $(2.94 \times 10^{-3})(28.952) = 0.0851$  s. That is, the nozzle flow, starting from the assumed initial conditions, takes only 85.1 ms to reach steady-state conditions; in reality, since convergence is obtained for all practical purposes after about 500 time steps, the practical convergence time is more on the order of 30 ms.

A comparison between some of the numerical results and the corresponding exact analytical values is given in Table 7.4; this provides you with a more detailed comparison than is given in Fig. 7.12. Compared are the numerical and analytical results for the density ratio and Mach number. Note that the numerical results, to three decimal places, are not in precise agreement with the analytical values; there is a small percentage disagreement between the two sets of results, ranging from 0.3 to 3.29 percent. This amount of error is not discernable on the graphical display in Fig. 7.12. At first thought, there might be three reasons for these small numerical inaccuracies: (1) a small inflow boundary condition error, (2) truncation errors associated with the finite value of  $\Delta x$ , such as discussed in Sec. 4.3, and (3) possible effects of the Courant number being substantially less than unity (recall that in the

**TABLE 7.3**

Flow-field variables after 1400 time steps (nonconservation form of the governing equations)

<i>I</i>	$\frac{x}{L}$	$\frac{A}{A^*}$	$\frac{\rho}{\rho_0}$	$\frac{V}{a_0}$	$\frac{T}{T_0}$	$\frac{p}{p_0}$	<i>M</i>	<i>m</i>
1	0.000	5.950	1.000	0.099	1.000	1.000	0.099	0.590
2	0.100	5.312	0.998	0.112	0.999	0.997	0.112	0.594
3	0.200	4.718	0.997	0.125	0.999	0.996	0.125	0.589
4	0.300	4.168	0.994	0.143	0.998	0.992	0.143	0.591
5	0.400	3.662	0.992	0.162	0.997	0.988	0.163	0.589
6	0.500	3.200	0.987	0.187	0.995	0.982	0.187	0.589
7	0.600	2.782	0.982	0.215	0.993	0.974	0.216	0.588
8	0.700	2.408	0.974	0.251	0.989	0.963	0.252	0.588
9	0.800	2.078	0.963	0.294	0.985	0.948	0.296	0.587
10	0.900	1.792	0.947	0.346	0.978	0.926	0.350	0.587
11	1.000	1.550	0.924	0.409	0.969	0.895	0.416	0.586
12	1.100	1.352	0.892	0.485	0.956	0.853	0.496	0.585
13	1.200	1.198	0.849	0.575	0.937	0.795	0.594	0.585
14	1.300	1.088	0.792	0.678	0.911	0.722	0.710	0.584
15	1.400	1.022	0.721	0.793	0.878	0.633	0.846	0.584
16	1.500	1.000	0.639	0.914	0.836	0.534	0.099	0.584
17	1.600	1.022	0.551	1.037	0.789	0.434	1.167	0.584
18	1.700	1.088	0.465	1.155	0.737	0.343	1.345	0.584
19	1.800	1.198	0.386	1.263	0.684	0.264	1.528	0.585
20	1.900	1.352	0.318	1.361	0.633	0.201	1.710	0.586
21	2.000	1.550	0.262	1.446	0.585	0.153	1.890	0.587
22	2.100	1.792	0.216	1.519	0.541	0.117	2.065	0.588
23	2.200	2.078	0.179	1.582	0.502	0.090	2.233	0.589
24	2.300	2.408	0.150	1.636	0.467	0.070	2.394	0.590
25	2.400	2.782	0.126	1.683	0.436	0.055	2.549	0.590
26	2.500	3.200	0.107	1.723	0.408	0.044	2.696	0.591
27	2.600	3.662	0.092	1.759	0.384	0.035	2.839	0.591
28	2.700	4.168	0.079	1.789	0.362	0.029	2.972	0.592
29	2.800	4.718	0.069	1.817	0.342	0.024	3.105	0.592
30	2.900	5.312	0.061	1.839	0.325	0.020	3.225	0.595
31	3.000	5.950	0.053	1.862	0.308	0.016	3.353	0.585

calculations discussed so far, the Courant number is chosen to be 0.5), such as discussed at the end of Sec. 4.5. Let us examine each of these reasons in turn.

**INFLOW BOUNDARY CONDITION ERROR.** There is a “built-in” error at the inflow boundary. At the first grid point, at  $x = 0$ , we *assume* that the density, pressure, and temperature are the reservoir properties  $\rho_0$ ,  $p_0$ , and  $T_0$ , respectively. This is strictly true only if  $M = 0$  at this point. In reality, there is a finite area ratio at  $x = 0$ , namely,  $A/A^* = 5.95$ , and hence a finite Mach number must exist at  $x = 0$ , both numerically and analytically (to allow a finite value of mass flow through the nozzle). Hence, in Table 7.4, the numerical value of  $\rho/\rho_0$  at  $x = 0$  is equal to 1.0—

**TABLE 7.4**  
Density ratio and Mach number distributions through the nozzle

$\frac{x}{L}$	$A$	$\frac{\rho}{\rho_0}$ (numerical results)	$\frac{\rho}{\rho_0}$		$M$ (numerical results)	$M$ (exact analytical results)	
			exact analytical results)	Difference, %		(exact analytical results)	Difference, %
0.000	5.950	1.000	0.995	0.50	0.099	0.098	1.01
0.100	5.312	0.998	0.994	0.40	0.112	0.110	1.79
0.200	4.718	0.997	0.992	0.30	0.125	0.124	0.08
0.300	4.168	0.994	0.990	0.40	0.143	0.140	2.10
0.400	3.662	0.992	0.987	0.50	0.163	0.160	1.84
0.500	3.200	0.987	0.983	0.40	0.187	0.185	1.07
0.600	2.782	0.982	0.978	0.41	0.216	0.214	0.93
0.700	2.408	0.974	0.970	0.41	0.252	0.249	1.19
0.800	2.078	0.963	0.958	0.52	0.296	0.293	1.01
0.900	1.792	0.947	0.942	0.53	0.350	0.347	0.86
1.000	1.550	0.924	0.920	0.43	0.416	0.413	0.72
1.100	1.352	0.892	0.888	0.45	0.496	0.494	0.40
1.200	1.198	0.849	0.844	0.59	0.594	0.592	0.34
1.300	1.088	0.792	0.787	0.63	0.710	0.709	0.14
1.400	1.022	0.721	0.716	0.69	0.846	0.845	0.12
1.500	1.000	0.639	0.634	0.78	0.999	1.000	0.10
1.600	1.022	0.551	0.547	0.73	1.167	1.169	0.17
1.700	1.088	0.465	0.461	0.87	1.345	1.348	0.22
1.800	1.198	0.386	0.382	1.04	1.528	1.531	0.20
1.900	1.352	0.318	0.315	0.94	1.710	1.715	0.29
2.000	1.550	0.262	0.258	1.53	1.890	1.896	0.32
2.100	1.792	0.216	0.213	1.39	2.065	2.071	0.29
2.200	2.078	0.179	0.176	1.68	2.233	2.240	0.31
2.300	2.408	0.150	0.147	2.00	2.394	2.402	0.33
2.400	2.782	0.126	0.124	2.38	2.549	2.557	0.31
2.500	3.200	0.107	0.105	1.87	2.696	2.706	0.37
2.600	3.662	0.092	0.090	2.17	2.839	2.848	0.32
2.700	4.168	0.079	0.078	1.28	2.972	2.983	0.37
2.800	4.718	0.069	0.068	1.45	3.105	3.114	0.29
2.900	5.312	0.061	0.059	3.29	3.225	3.239	0.43
3.000	5.950	0.053	0.052	1.89	3.353	3.359	0.18

this is our prescribed boundary condition. On the other hand, the exact analytical value of  $\rho/\rho_0$  at  $x = 0$  is 0.995, giving a 0.5 percent error. This built-in error is not viewed as serious, and we will not be concerned with it here.

**TRUNCATION ERROR: THE MATTER OF GRID INDEPENDENCE.** The matter of *grid independence* is a serious consideration in CFD, and this stage of our data analysis is a perfect time to introduce the concept. In general, when you solve a problem using CFD, you are employing a finite number of grid points (or a finite mesh) distributed over the flow field. Assume that you are using  $N$  grid points. If everything goes well during your solution, you will get some numbers out for the

flow-field variables at these  $N$  grid points, and these numbers may look qualitatively good to you. However, assume that you rerun your solution, this time using twice as many grid points,  $2N$ , distributed over the same domain; i.e., you have decreased the value of the increment  $\Delta x$  (and also  $\Delta y$  in general, if you are dealing with a two-dimensional solution). You may find that the values of your flow-field variables are quite different for this second calculation. If this is the case, then your solution is a function of the number of grid points you are using—an untenable situation. You must, if at all practical, continue to increase the number of grid points until you reach a solution which is no longer sensitive to the number of points. When you reach this situation, then you have achieved *grid independence*.

*Question:* Do we have grid independence for the present calculation? Recall that we have used 31 grid points distributed evenly through the nozzle. To address this question, let us double the number of grid points; i.e., let us halve the value of  $\Delta x$  by using 61 grid points. Table 7.5 compares the steady-state results for density, temperature, and pressure ratios, as well as for Mach numbers, at the throat for both the cases using 31 and 61 grid points. Also tabulated in Table 7.5 are the exact analytical results. Note that although doubling the number of grid points did improve the numerical solution, it did so only marginally. The same is true for all locations within the nozzle. In other words, the two steady-state numerical solutions are essentially the same, and therefore we can conclude that our original calculations using 31 grid points is essentially *grid-independent*. This grid independent solution does not agree *exactly* with the analytical results, but it is certainly close enough for our purposes. The degree of grid independence that you need to achieve in a given problem depends on what you want out of the solution. Do you need extreme accuracy? If so, you need to press the matter of grid independence in a very detailed fashion. Can you tolerate answers that can be a little less precise numerically (such as the 1 or 2 percent accuracy shown in the present calculations)? If so, you can slightly relax the criterion for extreme grid independence and use fewer grid points, thus saving computer time (which frequently means saving money). The proper decision depends on the circumstances. However, you should always be conscious of the question of grid independence and resolve the matter to your satisfaction for any CFD problem you solve. For example, in the present problem, do you think you can drive the numerical results shown in Table 7.5 to agree exactly with the analytical results by using more and more grid points? If so, how many grid points

TABLE 7.5  
Demonstration of grid independence

	Conditions at the nozzle throat			
	$\frac{\rho^*}{\rho_0}$	$\frac{T^*}{T_0}$	$\frac{p^*}{p_0}$	$M$
Case 1: 31 points	0.639	0.836	0.534	0.999
Case 2: 61 points	0.638	0.835	0.533	1.000
Exact analytical solution	0.634	0.833	0.528	1.000

will you need? You might want to experiment with this question by running your own program and seeing what happens.

**COURANT NUMBER EFFECTS.** At the end of Sec. 4.5, we broached the possibility that if the Courant number were too small, and hence the analytical domain for a given grid point were much smaller than the numerical domain, there might be problems in regard to the accuracy of the solution, albeit the solution will be very stable. Do we have such a problem with the present calculations? We have employed  $C = 0.5$  for the present calculations. Is this too small, considering that the stability criterion for *linear* hyperbolic equations (see Sec. 4.5) is  $C \leq 1.0$ ? To examine this question, we can simply repeat the previous calculations but with progressively higher values of the Courant number. The resulting steady-state flow-field values at the nozzle throat are tabulated in Table 7.6; the tabulations are given for six different values of  $C$ , starting at  $C = 0.5$  and ranging to 1.2. For values ranging to as high as  $C = 1.1$ , the results were only marginally different, as seen in Table 7.6. By increasing  $C$  to as high as 1.1., the numerical results do not agree any better with the exact analytical results (as shown in Table 7.6) than the results at lower values of  $C$ . Hence, all our previous results obtained by using  $C = 0.5$  are not tainted by any noticeable error due to the smaller-than-necessary value of  $C$ . Indeed, if anything, the numerical results for  $C = 0.5$  in Table 7.6 are marginally *closer* to the exact analytical solution than the results for higher Courant numbers. For the steady-state numerical results tabulated in Table 7.6, the number of time steps was adjusted each time  $C$  was changed so that the nondimensional time at the end of each run was essentially the same. This adjustment is necessary because the value of  $\Delta t$  calculated from Eqs. (7.66) and (7.69) will obviously be different for different values of  $C$ . For example, when  $C = 0.5$  as in our previous results, we carried out the time-marching procedure to 1400 time steps, which corresponded to a nondimensional time of 28.952. When  $C$  is increased to 0.7, the number of time steps carried out was  $1400(\frac{5}{7}) = 1000$ . This corresponded to a nondimensional time of 28.961—essentially the same as for the previous run. In the same manner, all the numerical data compared in Table 7.6 pertain to the same nondimensional time.

**TABLE 7.6**  
Courant number effects

Courant number	$\frac{\rho^*}{\rho_0}$	$\frac{T^*}{T_0}$	$\frac{p^*}{p_0}$	$M$
0.5	0.639	0.836	0.534	0.999
0.7	0.639	0.837	0.535	0.999
0.9	0.639	0.837	0.535	0.999
1.0	0.640	0.837	0.535	0.999
1.1	0.640	0.837	0.535	0.999
1.2	Program went unstable and blew up			
Exact analytical solution	0.634	0.833	0.528	1.000

It is interesting to note that for the present application, the CFL criterion as first introduced by Eq. (4.84), namely, that  $C \leq 1$ , does not hold exactly. In Table 7.6, we show results where  $C = 1.1$ ; a stable solution is obtained in spite of the fact that the CFL criterion is violated. However, as noted in Table 7.6, when the Courant number is increased to 1.2, instabilities do occur, and the program blows up. Therefore, for the flow problem we have been discussing in this chapter, which is governed by *nonlinear* hyperbolic partial differential equations, the CFL criterion (which is based on linear equations) does not hold exactly. However, from the above results, we can see that the CFL criterion is certainly a good *estimate* for the value of  $\Delta t$ ; it is the most reliable estimate for  $\Delta t$  that we can use, even though the governing equations are nonlinear.

## 7.4 CFD SOLUTION OF PURELY SUBSONIC ISENTROPIC NOZZLE FLOW

In this section we treat the case of purely subsonic flow through a duct. The physical aspects of such a flow are described in detail in Refs. 8 and 21. They differ from the subsonic-supersonic isentropic solution described in Sec. 7.2 in the following ways:

1. For subsonic flow in the duct, there are an *infinite* number of possible isentropic flow solutions, each one corresponding to a specific pressure ratio  $p_e/p_0$ , between the exit and the reservoir. Two such solutions are sketched in Fig. 7.13. For one case, labeled case *a*, the exit pressure is  $(p_e)_a$ , where  $(p_e)_a$  is only slightly smaller than the reservoir pressure  $p_0$ . This small pressure difference across the nozzle causes a “gentle wind” to blow through the duct, with the local Mach number increasing with distance in the convergent portion of the duct, reaching a peak value at the minimum area section (where this peak value of  $M$  is considerably less than 1), and then decreasing in the divergent section, resulting in the value of the Mach number at the exit  $(M_e)_a$ , being very small. If the exit pressure is reduced, hence creating a larger pressure difference across the nozzle, the flow through the nozzle will be faster. For example, for the case labeled *b* in Fig. 7.13, where  $(p_e)_b < (p_e)_a$ , the Mach number is larger through the nozzle, albeit still purely subsonic throughout. If the exit pressure is further reduced, there will be some value of  $p_e$ , say  $(p_e)_c$ , which results in the Mach number at the throat just barely grazing unity, such as sketched in Fig. 7.13. At the same time, the pressure at the minimum area section will equal  $0.528p_0$ , which corresponds to local sonic conditions. Examining Fig. 7.13 carefully, we note that for exit pressures  $p_e$  such that  $(p_e)_c < p_e < p_0$ , the flow through the duct will be purely subsonic. There are an infinite number of such flows, corresponding to the infinite choice of  $p_e$  in the range from  $p_0$  to  $(p_e)_c$ . Therefore, when the flow is totally subsonic throughout the duct, the local flow properties are dictated by *both* the local area ratio  $A/A_t$  (where  $A_t$  is the minimum area—the throat area) *and* the pressure ratio across the nozzle  $p_e/p_0$ . This is in contrast to the subsonic-supersonic case described in Sec. 7.2, where the local Mach number is strictly a function of the area ratio only [from Eq. (7.6)].

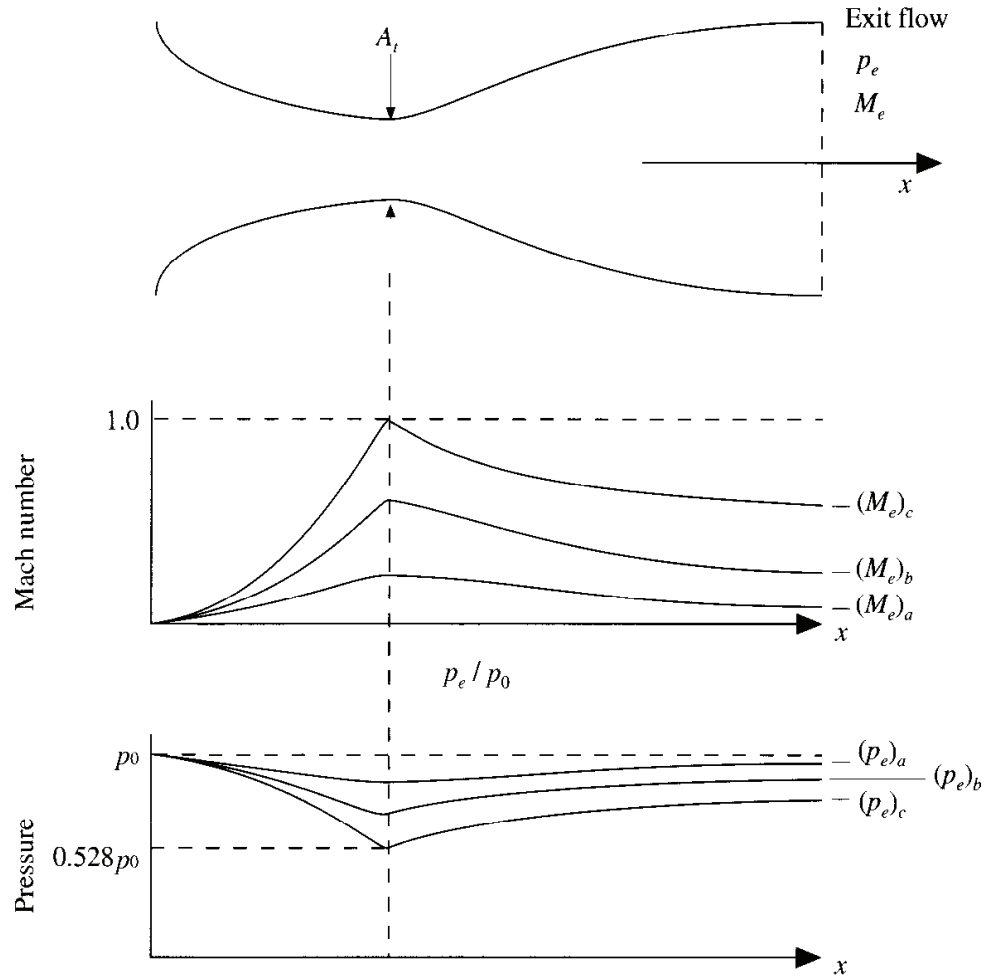


**FIG. 7.13**  
Schematic of purely subsonic flow in a convergent-divergent nozzle.

2. In the subsonic case, the Mach number at the minimum area  $A_t$  is less than 1. Hence,  $A_t$  is *not* the same as  $A^*$ , which is defined in Sec. 7.2 as the *sonic* throat area; that is,  $A^*$  is the throat area which corresponds to sonic flow. Hence, in the purely subsonic flow case,  $A^*$  is simply a reference area; moreover, in this situation,  $A^* < A_t$ .

The exact analytical solution of the purely subsonic flow case proceeds as follows. The exit-to-reservoir pressure ratio must be specified; that is,  $p_e/p_0$  is given. Since the total pressure is constant through the nozzle, the value of  $p_e/p_0$  defines  $M_e$  through Eq. (7.7), i.e.,

$$\frac{p_e}{p_0} = \left(1 + \frac{\gamma - 1}{2} M_e^2\right)^{-\gamma/(\gamma - 1)} \quad (7.78)$$

Once  $M_e$  is known from a solution of Eq. (7.78), the value of  $A^*$  can be calculated from Eq. (7.6) as

$$\frac{A_e}{A^*} = \frac{1}{M_e^2} \left[ \frac{2}{\gamma + 1} \left(1 + \frac{\gamma - 1}{2} M_e^2\right)\right]^{(\gamma + 1)/(\gamma - 1)} \quad (7.79)$$

where  $A^*$  is simply a reference value in this case;  $A^*$  is smaller than the throat area  $A_t$ . In turn, with  $A^*$  known, the local area divided by  $A^*$ , namely,  $A/A^*$ , determines the local Mach number  $M$  via Eq. (7.6). Finally, this local value of  $M$  determines the local values of  $p/p_0$ ,  $\rho/\rho_0$ , and  $T/T_0$  from Eqs. (7.7) to (7.9).

### 7.4.1 The Setup: Boundary and Initial Conditions

For this calculation, we will specify a nozzle with the following area distribution, where all symbols are in dimensional terms:

$$\frac{A}{A_t} = \begin{cases} 1 + 2.2\left(\frac{x}{L} - 1.5\right)^2 & \text{for } 0 \leq \frac{x}{L} \leq 1.5 \end{cases} \quad (7.80a)$$

$$\frac{A}{A_t} = \begin{cases} 1 + 0.2223\left(\frac{x}{L} - 1.5\right)^2 & \text{for } 1.5 \leq \frac{x}{L} \leq 3.0 \end{cases} \quad (7.80b)$$

In the above equations,  $A_t$  denotes the area of the nozzle throat. Keep in mind that as long as the flow is subsonic at the throat,  $A_t$  is *not* equal to  $A^*$ ; indeed,  $A_t > A^*$ . A plot of the area distribution given by Eqs. (7.80a) and (7.80b) is shown in Fig. 7.14.

The governing flow equations are the same as used for the subsonic-supersonic solutions discussed in Sec. 7.3, namely, Eqs. (7.46), (7.48), and (7.50).

The treatment of the boundary conditions for the present subsonic flow solution must reflect the need to *specify* the pressure ratio across the nozzle in order to have a unique solution, as discussed at the beginning of Sec. 7.4. Referring to Fig. 7.15, the subsonic inflow boundary, point 1, is treated exactly as discussed in the Boundary Conditions subsection to Sec. 7.3.1. However, in the present problem, the *outflow boundary* is also *subsonic*. In the context of the discussion of the Boundary Conditions subsection, we have at the subsonic outflow boundary one characteristic line (the right-running characteristic) propagating to the right and the other characteristic line (the left-running characteristic) propagating to the left. Also, the streamline at point  $N$  is moving toward the right. Examining Fig. 7.15, we see at point  $N$  one characteristic moving *out* of the domain, namely, the right-running characteristic, as well as the flow along the streamline moving *out* of the domain. Consistent with our discussion in the Boundary Condition subsection to

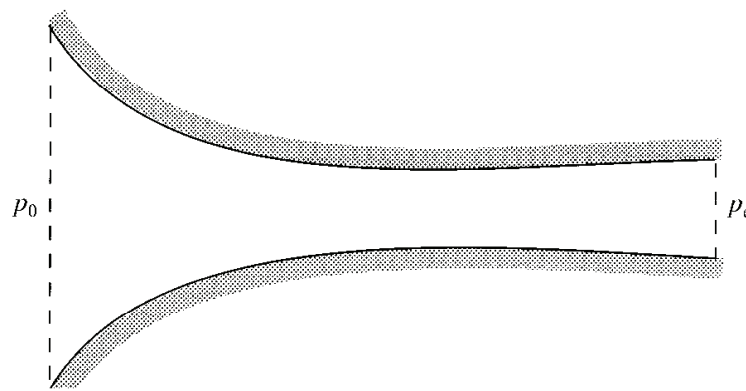


**FIG. 7.14**

Sketch of nozzle for the purely subsonic flow solution discussed in Sec. 7.4.

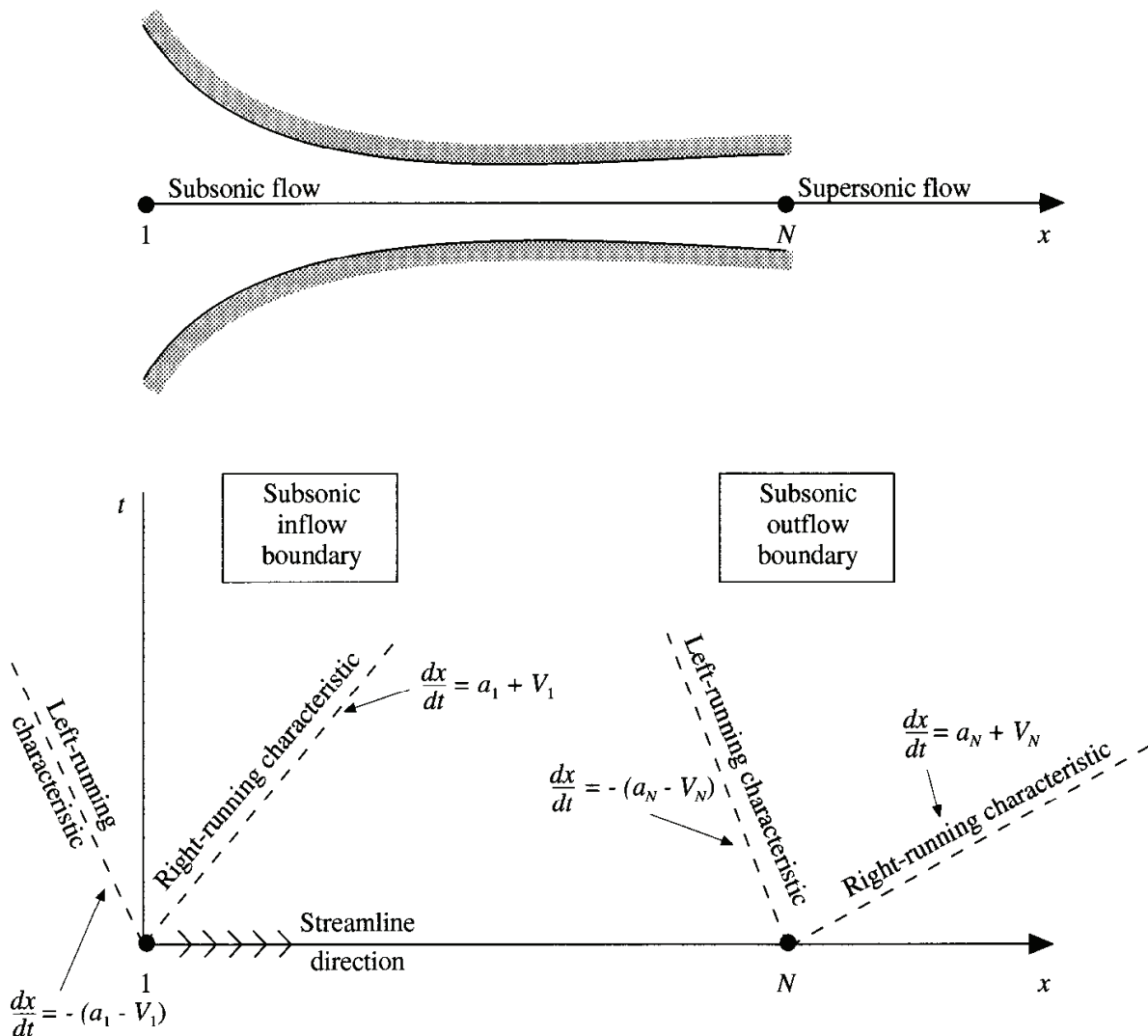


**FIG. 7.15**  
Study of boundary conditions for subsonic inflow and outflow.

Sec. 7.3.1 this means that two flow variables should be allowed to *float* at the boundary point  $N$ . On the other hand, we also see at point  $N$  *one* characteristic moving *into* the domain, namely, the left-running characteristic. As discussed in the Boundary Conditions subsection, this means that the value of *one* flow variable must be *specified* at the boundary point  $N$ . Of course, this is consistent with our earlier physical discussion, namely, that to have a unique solution of the purely subsonic flow in the duct, we need to specify the pressure ratio across the nozzle,  $p_0/p_e$ ; that is, for a fixed  $p_0$ , we need to *specify* the exit pressure  $p_e$ .

How do we implement the specification of  $p_e$  within the numerical solution? Returning to the governing equations, Eqs. (7.46), (7.48) and (7.50), we note that the dependent variables in these equations are density, velocity, and temperature—not pressure. However, through the equation of state,

$$p = \rho RT \quad (7.81)$$

Hence, specifying the value of  $p_e$  is the same as specifying the product  $\rho_e R T_e$ . In terms of the nondimensional variables in Eqs. (7.46), (7.48), and (7.50), we can

express Eq. (7.81) evaluated at the duct exit as

$$p'_e = \rho'_e T'_e \quad (7.82)$$

The numerical implementation of the boundary conditions is carried out as follows. The subsonic inflow boundary is treated exactly as in the Boundary Conditions subsection to Sec. 7.3.1; that is, Eqs. (7.70) and (7.71) are used here. For the subsonic *outflow* boundary, we have

$$p'_N = \text{specified value} \quad (7.83)$$

Since  $\rho'_N$  and  $T'_N$  are the dependent variables appropriate to our governing equations, we must make certain that both  $\rho'_N$  and  $T'_N$ , which will vary as a function of time, are strongly coupled to the pressure boundary condition given by Eq. (7.83); that is, no matter how  $\rho'_N$  and  $T'_N$  vary from one time step to the next, at *each* time step they must satisfy the constraint that

$$\rho'_N T'_N = p'_N = \text{specified value} \quad (7.84)$$

One way to accomplish this strong coupling is as follows. Let us linearly extrapolate  $T'_N$  obtaining

$$T'_N = 2T'_{N-1} - T'_{N-2} \quad (7.85)$$

From this value of  $T'_N$ , calculate  $\rho'_N$  from the equation of state such that Eq. (7.83) is satisfied, i.e.,

$$\rho'_N = \frac{p'_N}{T'_N} = \frac{\text{specified value}}{T'_N} \quad (7.86)$$

The values of  $T'_N$  from Eq. (7.85) along with  $\rho'_N$  from Eq. (7.86) ensure that  $p'_N$  remains constant at the specified value. Alternatively, we could obtain  $\rho'_N$  by linear extrapolation,

$$\rho'_N = 2\rho'_{N-1} - \rho'_{N-2} \quad (7.87)$$

and calculate  $T'_N$  from the equation of state,

$$T'_N = \frac{p'_N}{\rho'_N} = \frac{\text{specified value}}{\rho'_N} \quad (7.88)$$

The values of  $\rho'_N$  and  $T'_N$  obtained from Eqs. (7.87) and (7.88), respectively, also ensure that  $p'_N$  remains constant at the specified value. (It has been the author's experience that either combination works equally as well, i.e., the combination of Eqs. (7.85) and (7.86) where temperature is extrapolated or the combination of Eqs. (7.87) and (7.88) where density is extrapolated.) Finally, as before, the velocity at the downstream boundary is extrapolated:

$$V'_N = 2V'_{N-1} - V'_{N-2} \quad (7.89)$$

*Note:* There is more than meets the eye to the way we have set up the boundary conditions to this problem. We will return to this point in Sec. 7.4.2.

Finally, for the initial conditions, let us somewhat arbitrarily set up the following variations:

$$\rho' = 1.0 - 0.023x' \quad (7.90a)$$

$$T' = 1.0 - 0.009333x' \quad (7.90b)$$

$$V' = 0.05 + 0.11x' \quad (7.90c)$$

These specify the initial flow field at time  $t = 0$ .

We will carry out a time-marching solution of the purely subsonic flowfield using MacCormack's predictor-corrector explicit finite-difference method just as utilized for the previous subsonic-supersonic solution. The details are exactly the same. Indeed, to treat the subsonic flow described in this section, only a slight modification is needed to the computer program you might have written for the previous case—just the initial conditions, the nozzle shape, and the downstream boundary conditions need to be changed. Therefore, no further details are needed here.

#### 7.4.2 Final Numerical Results: MacCormack's Technique

In Sec. 7.3.2 we discussed some intermediate results pertaining to the detailed calculations on the first time step. Since exactly the same method is being used here, there is no need to discuss the intermediate calculations. Let us proceed to the final numerical results.

A feeling for the timewise variation of the flow field as it marches toward the steady-state solution is provided by Fig. 7.16 and 7.17. These results pertain to a

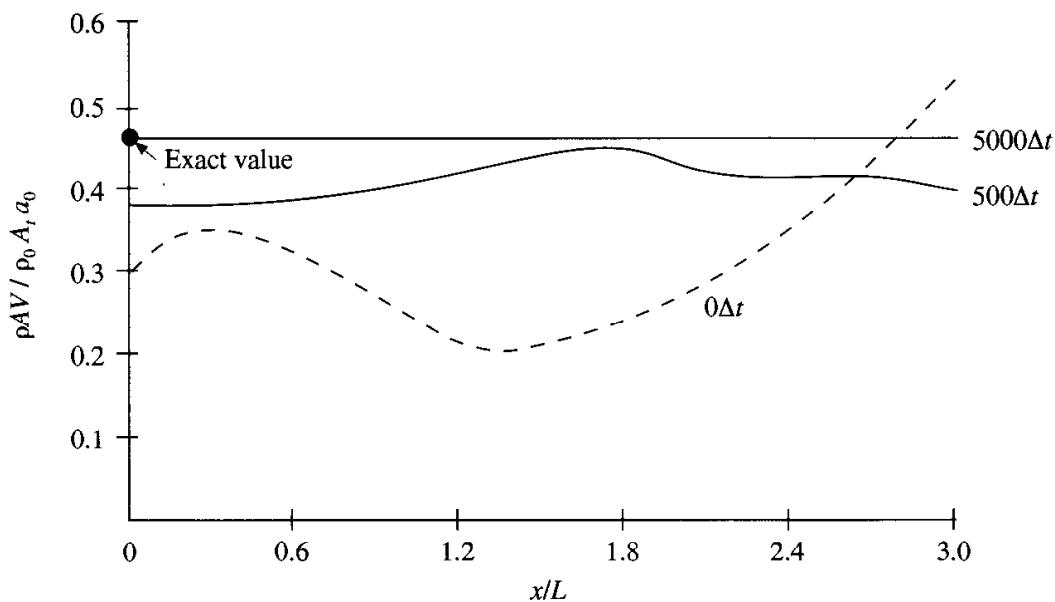
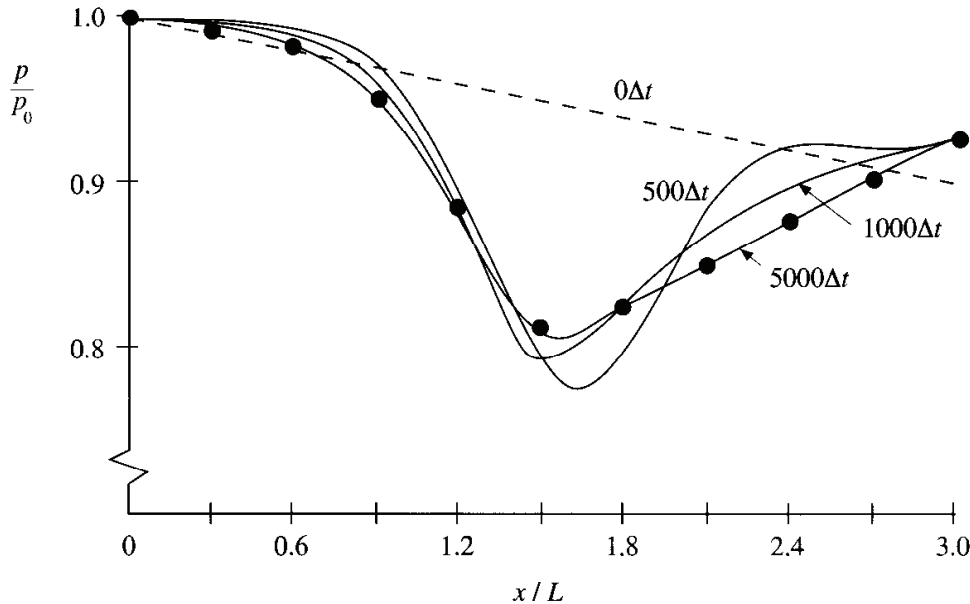


FIG. 7.16

Variation of mass flow through the nozzle at different times; purely subsonic flow case with  $p_e/p_0 = 0.93$ .

**FIG. 7.17**

Variation of the pressure distribution through the nozzle at different times; purely subsonic flow case with  $p_e/p_0 = 0.93$ . Circles indicate exact analytical values.

specified pressure ratio across the nozzle of  $p_e/p_0 = 0.93$ . The distribution of the nondimensional mass flow through the nozzle at three different times is shown in Fig. 7.16. The dashed curve labeled  $0\Delta t$  corresponds to the initial condition. Note that after 500 time steps (the curve labeled  $500\Delta t$ ) the mass flow is moving toward the steady-state value. After 5000 time steps, the mass flow has converged to a horizontal line; that is,  $\rho AV = \text{constant}$ . The dark circle is the exact analytical value; note that good agreement is achieved between the numerical and the analytical results. The timewise variation of the pressure distribution through the nozzle at four different times is shown in Fig. 7.17. Again, the dashed line is the initial distribution. Note that the initial condition for the pressure ratio at the exit is slightly below the specified value of 0.93; however, after the first time step, the boundary condition imposed by Eq. (7.84) is in effect, with  $p_e/p_0 = 0.93$ . This is reflected in the fact that the pressure distributions for  $500\Delta t$ ,  $1000\Delta t$ , and  $5000\Delta t$  all meet at the same point at the nozzle exit. The dark circles in Fig. 7.17 give the exact analytical values.

The final, steady-state values of the flow-field variables, including the mass flow, as a function of distance through the nozzle are tabulated in Table 7.7. For these calculations, 31 grid points are distributed through the nozzle, and the Courant number is 0.5. These results are for time step 5000. This is a conservative number of time steps; in reality, convergence is obtained for all practical purposes after 2500 time steps. The convergence behavior of the solution is further indicated by the values of the residuals (the average nondimensional time derivatives), which are on the order of  $10^{-2}$  after 500 time steps,  $10^{-3}$  after 2500 time steps, and  $10^{-5}$  after 5000 time steps.

A comparison of the numerical results after 5000 time steps with the exact analytical results is tabulated in Table 7.8. The accuracy of the numerical results for

**TABLE 7.7**  
Flow-field variables after 5000 time steps—subsonic flow

<i>I</i>	<i>x</i> <i>L</i>	<i>A</i> <i>A<sub>t</sub></i>	$\frac{\rho}{\rho_0}$	$\frac{V}{a_0}$	$\frac{T}{T_0}$	$\frac{p}{p_0}$	<i>M</i>	<i>m</i>
1	0.000	5.950	1.000	0.079	1.000	1.000	0.079	0.469
2	0.100	5.312	0.998	0.089	0.999	0.997	0.089	0.472
3	0.200	4.718	0.998	0.099	0.999	0.997	0.099	0.467
4	0.300	4.168	0.996	0.113	0.998	0.995	0.113	0.468
5	0.400	3.662	0.995	0.128	0.998	0.992	0.128	0.467
6	0.500	3.200	0.992	0.147	0.997	0.989	0.147	0.467
7	0.600	2.782	0.989	0.170	0.995	0.984	0.170	0.466
8	0.700	2.408	0.984	0.197	0.993	0.977	0.197	0.466
9	0.800	2.078	0.977	0.229	0.991	0.968	0.230	0.466
10	0.900	1.792	0.968	0.268	0.987	0.955	0.270	0.465
11	1.000	1.550	0.955	0.314	0.982	0.937	0.317	0.465
12	1.100	1.352	0.938	0.367	0.975	0.914	0.371	0.465
13	1.200	1.198	0.916	0.424	0.966	0.885	0.431	0.465
14	1.300	1.088	0.892	0.480	0.955	0.853	0.491	0.466
15	1.400	1.022	0.871	0.524	0.946	0.824	0.539	0.467
16	1.500	1.000	0.862	0.542	0.942	0.812	0.559	0.467
17	1.600	1.002	0.863	0.540	0.943	0.814	0.556	0.467
18	1.700	1.009	0.865	0.535	0.944	0.816	0.551	0.467
19	1.800	1.020	0.869	0.526	0.946	0.822	0.541	0.467
20	1.900	1.036	0.875	0.516	0.948	0.829	0.530	0.467
21	2.000	1.056	0.881	0.502	0.951	0.838	0.515	0.467
22	2.100	1.080	0.888	0.487	0.954	0.847	0.499	0.467
23	2.200	1.109	0.896	0.470	0.957	0.857	0.481	0.467
24	2.300	1.142	0.903	0.453	0.960	0.867	0.462	0.467
25	2.400	1.180	0.911	0.434	0.963	0.877	0.443	0.467
26	2.500	1.222	0.918	0.416	0.966	0.887	0.423	0.467
27	2.600	1.269	0.925	0.398	0.970	0.897	0.404	0.467
28	2.700	1.320	0.932	0.379	0.972	0.906	0.385	0.467
29	2.800	1.376	0.938	0.362	0.975	0.915	0.366	0.467
30	2.900	1.436	0.944	0.344	0.977	0.923	0.348	0.467
31	3.000	1.500	0.949	0.327	0.980	0.930	0.331	0.466

this purely subsonic case is about the same as that obtained for the subsonic-supersonic isentropic flow case (see Table 7.4).

It is interesting to note the values of time required to come to a reasonable steady state. For the present case,  $t' = t/(L/a_0) = 84.3$ . This is to be compared with the nondimensional time required for convergence in the subsonic-supersonic flow case calculated earlier, which after 500 time steps was 10.3. For the same nozzle length  $L$  and reservoir speed of sound  $a_0$ , the subsonic flow takes a much longer time to converge to the steady state. That is, in part, a reflection of the time it takes for a fluid element to travel through the nozzle, which we will call the *transit time*. For the steady state to be reached, there should be a time lapse of several transit times—this is required for the history of the initial conditions to “flush through” the nozzle. For a purely subsonic flow, the fluid elements have an average velocity much

**TABLE 7.8**

Comparison between numerical and analytical values

$\frac{x}{L}$	$\frac{A}{A_t}$	$\frac{\rho}{\rho_0}$ (numerical results)	$\frac{\rho}{\rho_0}$ (exact analytical results)	Difference, %	$M$ (numerical results)	$M$ (exact analytical results)	Difference, %
0.000	5.950	1.000	0.997	0.30	0.079	0.077	2.50
0.100	5.312	0.998	0.996	0.20	0.089	0.086	3.30
0.200	4.718	0.998	0.995	0.30	0.099	0.097	2.00
0.300	4.168	0.996	0.994	0.20	0.113	0.110	2.65
0.400	3.662	0.995	0.992	0.30	0.128	0.126	1.56
0.500	3.200	0.992	0.990	0.20	0.147	0.144	2.04
0.600	2.782	0.989	0.986	0.30	0.170	0.167	1.76
0.700	2.408	0.984	0.981	0.30	0.197	0.194	1.52
0.800	2.078	0.977	0.975	0.20	0.230	0.226	1.74
0.900	1.792	0.968	0.966	0.20	0.270	0.265	1.85
1.000	1.550	0.955	0.953	0.21	0.317	0.312	1.58
1.100	1.352	0.938	0.936	0.21	0.371	0.365	1.62
1.200	1.198	0.916	0.916	0.00	0.431	0.423	1.86
1.300	1.088	0.892	0.893	0.11	0.491	0.480	2.24
1.400	1.022	0.871	0.875	0.46	0.539	0.524	2.78
1.500	1.000	0.862	0.867	0.58	0.559	0.541	3.22
1.600	1.002	0.863	0.868	0.58	0.556	0.539	3.06
1.700	1.009	0.865	0.870	0.57	0.551	0.534	3.09
1.800	1.020	0.869	0.874	0.58	0.541	0.526	2.77
1.900	1.036	0.875	0.879	0.46	0.530	0.514	3.02
2.000	1.056	0.881	0.885	0.45	0.515	0.500	2.91
2.100	1.080	0.888	0.892	0.45	0.499	0.485	2.81
2.200	1.109	0.896	0.898	0.33	0.481	0.468	2.91
2.300	1.142	0.903	0.906	0.33	0.462	0.450	2.60
2.400	1.180	0.911	0.913	0.22	0.443	0.431	2.71
2.500	1.222	0.918	0.920	0.22	0.423	0.413	2.36
2.600	1.269	0.925	0.926	0.11	0.404	0.394	2.48
2.700	1.320	0.932	0.933	0.11	0.385	0.376	2.34
2.800	1.376	0.938	0.939	0.11	0.366	0.358	2.19
2.900	1.436	0.944	0.944	0.00	0.348	0.340	2.30
3.000	1.500	0.949	0.949	0.00	0.331	0.324	2.11

lower than for the subsonic-supersonic case; hence the transit time for the subsonic case is much larger. For this reason, nature simply takes a longer time to establish a steady subsonic flow compared to that for a steady supersonic flow. Such a trend is clearly evident in our results here.

### 7.4.3 The Anatomy of a Failed Solution

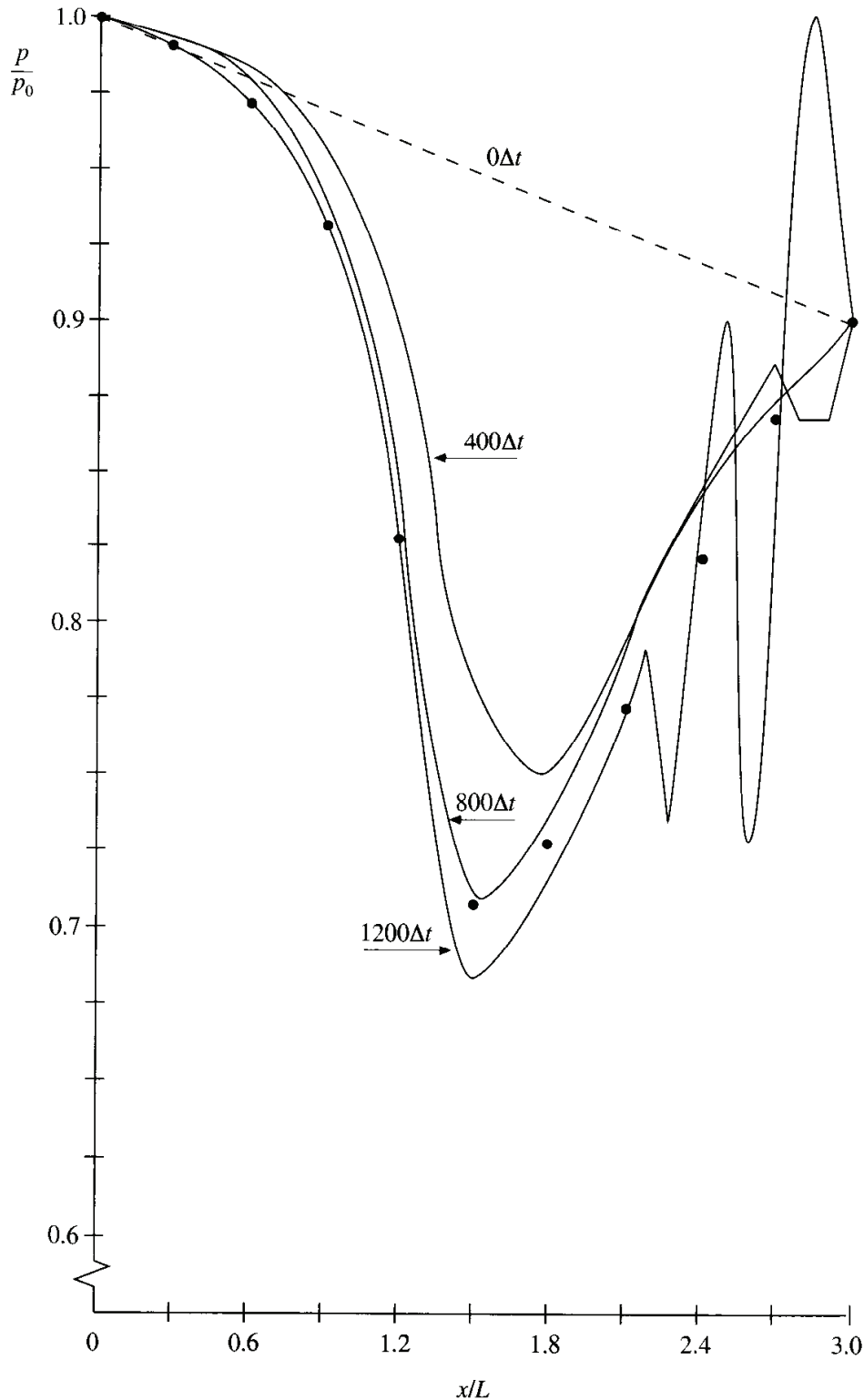
In our discussion of the way we have set up the boundary conditions in Sec. 7.4.1, we noted that there was more to it than meets the eye. Let us examine this comment further.

Consider a case where  $p_e/p_0 = 0.9$ ; this is a stronger pressure ratio across the nozzle than the case discussed in Sec. 7.4.2, where  $p_e/p_0 = 0.93$ . Therefore, the flow Mach number inside the nozzle will be larger. However, according to the exact analytical solution, the steady flow through our nozzle with  $p_e/p_0 = 0.9$  should still be subsonic everywhere; the highest Mach number, which occurs at the throat, is theoretically  $M_t = 0.721$ , and the theoretical Mach number at the exit is 0.391. Nevertheless, under the same conditions as those used in Sec. 7.4.2 (same initial conditions, Courant number, and boundary condition treatment) the case with  $p_e/p_0 = 0.9$  goes unstable and blows up. It is instructional to investigate the behavior of the blowup and to surmise the reasons for this behavior.

The distribution of pressure through the nozzle at four different times is shown in Fig. 7.18. The dashed line labeled  $0\Delta t$  is the initial distribution at time  $t = 0$ . After 400 time steps (the curve labeled  $400\Delta t$ ), the flow appears to be moving toward a qualitatively proper solution. After 800 time steps, for the most part, the solution appears to be approaching a proper steady-state result; for example, at  $800\Delta t$ , the numerical results show the Mach number at the throat  $M_t = 0.704$ , very close to the theoretical value of 0.721. A further comparison is given by the solid circles in Fig. 7.18, which represent the exact analytical results for  $p/p_0$ . Note that in the convergent section of the nozzle ( $x/L < 1.5$ ), the proper steady state is almost achieved. However, tracing through the curve for  $800\Delta t$ , we see a small but disturbing oscillation forming at the downstream boundary. At  $1200\Delta t$ , this oscillation has escalated enormously, and shortly thereafter the solution blows up. This behavior, which occurs when  $p_e/p_0 = 0.9$ , is completely different than the behavior shown in Fig. 7.17 for the case of  $p_e/p_0 = 0.93$ , where the steady state is successfully approached after about 2500 time steps.

Why do the oscillations shown in Fig. 7.18 develop? In short, they are due to finite waves that reflect off the downstream boundary, where the reflection is due to purely numerical reasons. Since we are holding the exit pressure  $p_e$  constant throughout the calculation, there is every reason to expect that finite, unsteady compression and expansion waves that are traveling to the right in the unsteady nozzle flow will reflect off this constant-pressure boundary. If these waves are strong enough, massive oscillations will occur near the downstream boundary. Given enough time, the oscillations eventually lead to a blowup of the calculations. Obviously, for a less severe pressure ratio across the nozzle, such as  $p_e/p_0 = 0.93$ , the weaker unsteady waves produced within the nozzle, when reflected from the downstream boundary, do not set up an oscillation.

Let us reexamine the downstream boundary condition on a physical basis. Our stipulation of a *fixed*, constant pressure at the exit is physically valid only in the *steady-state* case. During the unsteady flow, finite compression and expansion waves travel up and down the nozzle. As these waves travel out of the nozzle at the downstream boundary, *all* the flow variables, including the pressure, *fluctuate* with time. This is the real *physical* situation. (See Chap. 7 of Ref. 21 for a discussion of unsteady, one-dimensional, finite-wave properties.) In the numerical calculation discussed above, we are not allowing the pressure at the downstream boundary to fluctuate; we are stipulating that it is fixed, independent of time. This is the proper boundary condition as the flow approaches the steady state, but it is physically

**FIG. 7.18**

Variation of the pressure distribution through the nozzle at different times; purely subsonic flow case with  $p_e/p_0 = 0.90$ . Note the oscillatory behavior after 1200 time steps. Circles indicate exact analytical values.

improper during the unsteady flow variations that take place during the time-marching process. As a result, with the numerically fixed pressure at the exit, we are in part “bottling up” the waves inside the nozzle. When the pressure ratio  $p_e/p_0$  is

strong enough (such as in the case of  $p_e/p_0 = 0.9$ ), the unsteady finite waves produced at early times in the nozzle are sufficiently strong, and the nonphysical reflections from the constant-pressure boundary eventually grow into the type of oscillations shown in Fig. 7.18, with the result that the calculations blow up. On the other hand, if the pressure ratio  $p_e/p_0$  is milder (such as in the case of  $p_e/p_0 = 0.93$ ), the unsteady finite waves are weaker, and we are able to obtain a proper, steady state, as described earlier.

There are several “fixes” that we could try in order to improve the behavior of the attempted solution for  $p_e/p_0 = 0.9$ . First, we could simply try different initial conditions, ones that are closer to the steady-state answers. In this fashion, the unsteady finite waves set up during the transient approach to the steady state will be weaker, therefore diminishing the tendency for the oscillation buildup as reflected in Fig. 7.18. Second, we could add some artificial viscosity for the reasons discussed in Sec. 6.6. Note that so far in the our nozzle calculations, we have not explicitly added artificial viscosity. However, one of the purposes of artificial viscosity is to help damp the type of oscillations shown in Fig. 7.18. Such a ploy may be effective for the present case.

We will not pursue either of these possible fixes here because we need to turn our attention to other, more pressing matters. We will have the opportunity to explore the matter of adding artificial viscosity to our nozzle calculation in Sec. 7.6, which deals with a shock-capturing case.

## 7.5 THE SUBSONIC-SUPERSONIC ISENTROPIC NOZZLE SOLUTION REVISITED: THE USE OF THE GOVERNING EQUATIONS IN CONSERVATION FORM

In Chap. 2 we made a distinction between the nonconservation form and the conservation form of the governing flow equations. We made the point that, theoretically, either form of the equations is a suitable representation of the fundamental physical principles of mass conservation, Newton’s second law, and energy conservation. However, in CFD, there are some good numerical reasons to use one form or the other for the solution of certain flow problems. An important example is the case of shock capturing (see Sec. 2.10), where we noted that the conservation form of the equations is the proper form to employ; the nonconservation form will lead to poor numerical results.

In the present section, we take the opportunity to examine the differences between results obtained from the nonconservation form of the equations and those obtained from the conservation form. We will first cast the governing equations for quasi-one-dimensional flow in conservation form. Then we will set up the numerical solution of these equations using MacCormack’s technique, as applied to the subsonic-supersonic isentropic flow case. The matter of shock capturing within the nozzle will be deferred until Sec. 7.6. Finally, we will compare the numerical results obtained from the conservation form of the equations to those obtained from the nonconservation form.

### 7.5.1 The Basic Equations in Conservation Form

Returning to Eq. (7.15), repeated below.

$$\frac{\partial(\rho A)}{\partial t} + \frac{\partial(\rho A V)}{\partial x} = 0 \quad (7.15)$$

This is the continuity equation for quasi-one-dimensional flow. It is already in conservation form. Nondimensionalizing the variables according to the forms given in Sec. 7.2, we have

$$\frac{\partial \left( \frac{\rho}{\rho_0} \frac{A}{A^*} \right)}{\partial \left( \frac{t}{L/a_0} \right)} \left( \frac{\rho_0 A^* a_0}{L} \right) + \frac{\partial \left( \frac{\rho}{\rho_0} \frac{A}{A^*} \frac{V}{a_0} \right)}{\partial(x/L)} \left( \frac{\rho_0 A^* a_0}{L} \right) = 0$$

$$\boxed{\frac{\partial(\rho' A')}{\partial t'} + \frac{\partial(\rho' A' V')}{\partial x'}} \quad (7.91)$$

or

As before, the primes in Eq. (7.91) denote the nondimensional variables.

Return to Eq. (7.23), repeated below.

$$\frac{\partial(\rho A V)}{\partial t} + \frac{\partial(\rho A V^2)}{\partial x} = -A \frac{\partial p}{\partial x} \quad (7.23)$$

This is the momentum equation for quasi-one-dimensional flow. It is already in conservation form. Let us combine the two  $x$  derivatives in Eq. (7.23) as follows. Since

$$\frac{\partial(pA)}{\partial x} = p \frac{\partial A}{\partial x} + A \frac{\partial p}{\partial x} \quad (7.92)$$

we can add Eq. (7.92) to Eq. (7.23), obtaining

$$\frac{\partial(\rho A V)}{\partial t} + \frac{\partial(\rho A V^2 + pA)}{\partial x} = p \frac{\partial A}{\partial x} \quad (7.93)$$

Nondimensionalizing Eq. (7.93), we have

$$\begin{aligned} & \frac{\partial \left( \frac{\rho}{\rho_0} \frac{A}{A^*} \frac{V}{a_0} \right)}{\partial \left( \frac{t}{L/a_0} \right)} \left( \frac{\rho_0 A^* a_0^2}{L} \right) + \frac{\partial \left[ \frac{\rho}{\rho_0} \frac{A}{A^*} \frac{V^2}{a_0^2} (\rho_0 A^* a_0^2) + \frac{p}{p_0} \frac{A}{A^*} (p_0 A^*) \right]}{\partial \left( \frac{x}{L} \right) L} \\ &= \frac{p}{p_0} \frac{\partial(A/A^*)}{\partial(x/L)} \left( \frac{p_0 A^*}{L} \right) \end{aligned}$$

or

$$\frac{\partial(\rho' A' V')}{\partial t'} + \frac{\partial[\rho' A' V'^2 + p' A' (p_0/\rho_0 a_0^2)]}{\partial x'} = p' \frac{\partial A'}{\partial x'} \left( \frac{p_0}{\rho_0 a_0^2} \right) \quad (7.94)$$

However,

$$\frac{p_0}{\rho_0 a_0^2} = \frac{\rho_0 R T_0}{\rho_0 a_0^2} = \frac{\rho_0 R T_0}{\rho_0 \gamma R T_0} = \frac{1}{\gamma}$$

Thus, Eq. (7.94) becomes

$$\boxed{\frac{\partial(\rho' A' V')}{\partial t'} + \frac{\partial[\rho' A' V'^2 + (1/\gamma)p' A']}{\partial x'} = \frac{1}{\gamma} p' \frac{\partial A'}{\partial x'}} \quad (7.95)$$

Returning to Eq. (7.33), repeated below.

$$\frac{\partial[\rho(e + V^2/2)A]}{\partial t} + \frac{\partial[\rho(e + V^2/2)AV]}{\partial x} = - \frac{\partial(pAV)}{\partial x} \quad (7.33)$$

This is the energy equation for quasi-one-dimensional flow. It is already in conservation form. Combining the  $x$  derivatives in Eq. (7.33), we have

$$\frac{\partial[\rho(e + V^2/2)A]}{\partial t} + \frac{\partial[\rho(e + V^2/2)AV + pAV]}{\partial x} = 0 \quad (7.96)$$

Let us define a nondimensional internal energy as follows:

$$e' = \frac{e}{e_0} \quad \text{where } e_0 = c_v T_0 = \frac{R T_0}{\gamma - 1}$$

With this, the nondimensional form of Eq. (7.96) is obtained as follows.

$$\begin{aligned} & \frac{\partial \left\{ \frac{\rho}{\rho_0} \left[ \frac{e}{e_0} (e_0) + \frac{V^2}{2a_0^2} (a_0^2) \right] \frac{A}{A^*} \right\}}{\partial \left( \frac{t}{L/a_0} \right)} \left( \frac{\rho_0 A^* a_0}{L} \right) \\ & + \frac{\partial \left\{ \frac{\rho}{\rho_0} \left[ \frac{e}{e_0} (e_0) + \frac{V^2}{2a_0^2} (a_0^2) \right] \frac{V}{a_0} \frac{A}{A^*} (\rho_0 a_0 A^*) + \left( \frac{p}{p_0} \frac{A}{A^*} \frac{V}{a_0} \right) (\rho_0 A^* a_0) \right\}}{\partial \left( \frac{x}{L} \right)} = 0 \end{aligned} \quad (7.97)$$

Since  $e_0 = RT_0/(\gamma - 1)$ , Eq. (7.97) becomes

$$\begin{aligned} & \frac{\partial \left[ \rho' \left( \frac{e'}{\gamma - 1} + \frac{\gamma}{2} V'^2 \right) A' \right]}{\partial t'} \left( \frac{\rho_0 A^* a_0 R T_0}{L} \right) \\ & + \frac{\partial \left[ \rho' \left( \frac{e'}{\gamma - 1} + \frac{\gamma}{2} V'^2 \right) V' A' \left( \frac{\rho_0 a_0 A^* R T_0}{L} \right) + (p' A' V') \left( \frac{\rho_0 A^* a_0}{L} \right) \right]}{\partial x'} = 0 \end{aligned} \quad (7.98)$$

Divide Eq. (7.98) by  $\rho_0 A^* a_0 R T_0 / L$ .

$$\frac{\partial \left[ \rho' \left( \frac{e'}{\gamma - 1} + \frac{\gamma}{2} V'^2 \right) A' \right]}{\partial t'} + \frac{\partial \left[ \rho' \left( \frac{e'}{\gamma - 1} + \frac{\gamma}{2} V'^2 \right) V' A' + p' A' V' \left( \frac{p_0}{\rho_0 R T_0} \right) \right]}{\partial x'} = 0 \quad (7.99)$$

However, in Eq. (7.99),

$$\frac{p_0}{\rho_0 R T_0} = \frac{\rho_0 R T_0}{\rho_0 R T_0} = 1$$

Thus, Eq. (7.99) becomes

$$\frac{\partial \left[ \rho' \left( \frac{e'}{\gamma - 1} + \frac{\gamma}{2} V'^2 \right) A' \right]}{\partial t'} + \frac{\partial \left[ \rho' \left( \frac{e'}{\gamma - 1} + \frac{\gamma}{2} V'^2 \right) V' A' + p' A' V' \right]}{\partial x'} = 0 \quad (7.100)$$

Equations (7.91), (7.95), and (7.100) are the nondimensional conservation form of the continuity, momentum, and energy equations for quasi-one-dimensional flow, respectively. Return to Eq. (2.93), which is a generic form of the governing equations for unsteady, three-dimensional flow. The equations for quasi-one-dimensional flow can be expressed in a similar generic form. Let us define the elements of the solutions vector  $U$ , the flux vector  $F$ , and the source term  $J$  as follows.

$$\begin{aligned} U_1 &= \rho' A' \\ U_2 &= \rho' A' V' \\ U_3 &= \rho' \left( \frac{e'}{\gamma - 1} + \frac{\gamma}{2} V'^2 \right) A' \\ F_1 &= \rho' A' V' \\ F_2 &= \rho' A' V'^2 + \frac{1}{\gamma} p' A' \\ F_3 &= \rho' \left( \frac{e'}{\gamma - 1} + \frac{\gamma}{2} V'^2 \right) V' A' + p' A' V' \\ J_2 &= \frac{1}{\gamma} p' \frac{\partial A'}{\partial x'} \end{aligned}$$

With these elements, Eqs. (7.91), (7.95), and (7.100) can be written, respectively, as

$$\frac{\partial U_1}{\partial t'} = - \frac{\partial F_1}{\partial x'} \quad (7.101a)$$

$$\frac{\partial U_2}{\partial t'} = - \frac{\partial F_2}{\partial x'} + J_2 \quad (7.101b)$$

$$\frac{\partial U_3}{\partial t'} = - \frac{\partial F_3}{\partial x'} \quad (7.101c)$$

We are now finished with the governing equations for quasi-one-dimensional flow. Equations (7.101a) to (7.101c) represent the continuity, momentum, and energy equations for quasi-one-dimensional flow, in conservation form. These are the equations we wish to numerically solve using MacCormack's technique.

Before setting up this numerical solution, keep in mind from our discussions in Chap. 2 that in the conservation form of the equations the dependent variables (the variables for which we directly obtain numbers) are *not* the primitive variables. For example, in Eqs. (7.101a) to (7.101c), our numerical solution will give us numbers directly for  $U_1$ ,  $U_2$ , and  $U_3$  in steps of time; this is why  $U$  is called the *solutions vector*. To obtain the primitive variables ( $\rho$ ,  $V$ ,  $T$ ,  $p$ , etc.), we must *decode* the elements  $U_1$ ,  $U_2$ , and  $U_3$  as follows. From the definitions of  $U_1$ ,  $U_2$ , and  $U_3$  given above, we have

$$\rho' = \frac{U_1}{A'} \quad (7.102)$$

$$V' = \frac{U_2}{U_1} \quad (7.103)$$

$$T' = e' = (\gamma - 1) \left( \frac{U_3}{U_1} - \frac{\gamma}{2} V'^2 \right) \quad (7.104)$$

$$p' = \rho' T' \quad (7.105)$$

Note in Eq. (7.104) that we have recognized the fact that  $e' = T'$ , or

$$e' \equiv \frac{e}{e_0} = \frac{c_v T}{c_v T_0} = \frac{T}{T_0} = T'$$

Therefore, after we obtain  $U_1$ ,  $U_2$ , and  $U_3$  at each time step from the numerical solution of Eqs. (7.101a) to (7.101c), we can immediately calculate the corresponding primitive variables at each time step,  $\rho'$ ,  $V'$ ,  $T'$ , and  $p'$ , from Eqs. (7.102) to (7.105).

### 7.5.2 The Setup

Return to Eqs. (7.101a) to (7.101c) for a moment; we note that the flux vector elements  $F_1$ ,  $F_2$ , and  $F_3$  are couched in terms of the primitive variables [see the relations for  $F_1$ ,  $F_2$ , and  $F_3$  immediately preceding Eqs. (7.101a) to (7.101c)]. It has been the author's experience that when the computer program is written with  $F_1$ ,  $F_2$ , and  $F_3$  expressed directly in terms of  $\rho'$ ,  $V'$ ,  $p'$ , and  $e'$ , instabilities develop during the course of the time-marching solution. For example, in the present example of quasi-one-dimensional, subsonic-supersonic, isentropic nozzle flow, instabilities develop in the subsonic section which finally cause the program to blow up after about 300 time steps. This behavior is an example of a lack of "purity" in the formulation of the governing equations in conservation form, a lack which eventually causes numerical problems. If we were to write a computer program to implement the equations exactly as written in Sec. 7.5.1, we would set up the

numerical solution of Eqs. (7.101a) to (7.101c) for  $U_1$ ,  $U_2$ , and  $U_3$  at each time step. We would then *decode* these elements of the solutions vector to obtain the primitive variables at each time step, as shown in Eqs. (7.102) to (7.105). These primitive variables  $\rho'$ ,  $V'$ ,  $e'$ , and  $p'$  would, in turn, be used to construct  $F_1$ ,  $F_2$ , and  $F_3$  for use in the solution of Eqs. (7.101a) to (7.101c) for the next time step, and so forth. As stated above, in the author's experience, when the primitive variables are used to construct  $F_1$ ,  $F_2$ , and  $F_3$ , numerical difficulties occasionally arise. This is somehow connected to the fact that the dependent variables which appear *explicitly* in Eqs. (7.101a) to (7.101c) are  $U_1$ ,  $U_2$ , and  $U_3$ —not the primitive variables. For this reason, it is best to couch  $F_1$ ,  $F_2$ , and  $F_3$  *directly* in terms of the dependent variables  $U_1$ ,  $U_2$ , and  $U_3$  and avoid the use of the primitive variables in Eqs. (7.101a) to (7.101c). That is, in Eqs. (7.101a) to (7.101c), we will write

$$F_1 = F_1(U_1, U_2, U_3) \quad (7.106a)$$

$$F_2 = F_2(U_1, U_2, U_3) \quad (7.106b)$$

$$F_3 = F_3(U_1, U_2, U_3) \quad (7.106c)$$

$$J_2 = J(U_1, U_2, U_3) \quad (7.106d)$$

such that the governing equations are “purely” in terms of the elements of the solution vector, i.e., in terms of  $U_1$ ,  $U_2$ , and  $U_3$  *only*. Let us proceed to obtain the specific forms indicated by Eqs. (7.106a) to (7.106d).

**“PURE” FORM OF THE FLUX TERMS.** Consider the flux term  $F_1$ , given in Sec. 7.5.1 by

$$F_1 = \rho' A' V' \quad (7.107)$$

Substituting Eqs. (7.102) and (7.103) for  $\rho'$  and  $V'$ , respectively, into Eq. (7.107), we have

$$\boxed{F_1 = U_2} \quad (7.108)$$

Consider the flux term  $F_2$ , given in Sec. 7.5.1 by

$$F_2 = \rho' A' V'^2 + \frac{1}{\gamma} p' A' \quad (7.109)$$

From Eq. (7.105), the pressure in Eq. (7.109) can be replaced by the product  $\rho' T'$ . In turn,  $\rho'$ ,  $V'$ , and  $T'$  can be expressed in terms of  $U_1$ ,  $U_2$ , and  $U_3$  via Eqs. (7.102) to (7.104). Hence, Eq. (7.109) becomes

$$F_2 = \frac{U_2^2}{U_1} + \frac{1}{\gamma} U_1 (\gamma - 1) \left[ \frac{U_3}{U_1} - \frac{\gamma}{2} \left( \frac{U_2}{U_1} \right)^2 \right]$$

or

$$\boxed{F_2 = \frac{U_2^2}{U_1} + \frac{\gamma - 1}{\gamma} \left( U_3 - \frac{\gamma}{2} \frac{U_2^2}{U_1} \right)} \quad (7.110)$$

Consider the flux term  $F_3$ , given in Sec. 7.5.1 by

$$F_3 = \rho' \left( \frac{e'}{\gamma - 1} + \frac{\gamma}{2} V'^2 \right) V' A' + p' A' V' \quad (7.111)$$

Substituting Eqs. (7.102) to (7.105) into Eq. (7.111), we have

$$\begin{aligned} F_3 &= U_2 \left( \frac{U_3}{U_1} - \frac{\gamma}{2} V'^2 + \frac{\gamma}{2} V'^2 \right) + U_2 T' \\ &= \frac{U_2 U_3}{U_1} + (\gamma - 1) U_2 \left[ \frac{U_3}{U_1} - \frac{\gamma}{2} \left( \frac{U_2}{U_1} \right)^2 \right] \end{aligned}$$

or

$$F_3 = \gamma \frac{U_2 U_3}{U_1} - \frac{\gamma(\gamma - 1)}{2} \frac{U_2^3}{U_1^2} \quad (7.112)$$

Finally, the source term  $J_2$  was given in Sec. 7.5.1 as

$$J_2 = \frac{1}{\gamma} p' \frac{\partial A'}{\partial x'} \quad (7.113)$$

From Eq. (7.105), this becomes

$$J_2 = \frac{1}{\gamma} \rho' T' \frac{\partial A'}{\partial x'} \quad (7.114)$$

Substituting Eqs. (7.102) and (7.104) into (7.114), we have

$$J_2 = \frac{1}{\gamma} \frac{U_1}{A'} (\gamma - 1) \left[ \frac{U_3}{U_1} - \frac{\gamma}{2} \left( \frac{U_2}{U_1} \right)^2 \right] \frac{\partial A'}{\partial x'}$$

or

$$J_2 = \frac{\gamma - 1}{\gamma} \left( U_3 - \frac{\gamma}{2} \frac{U_2^2}{U_1} \right) \frac{\partial(\ln A')}{\partial x'} \quad (7.115)$$

We now return to our governing flow equations in conservation form as given by Eqs. (7.101a) to (7.101c). With  $F_1$ ,  $F_2$ ,  $F_3$ , and  $J_2$  given by Eqs. (7.108), (7.110), (7.112), and (7.115), respectively, then Eqs. (7.101a) to (7.101c) are expressed in terms of  $U_1$ ,  $U_2$ , and  $U_3$  only—the primitive variables are nowhere to be found. This is the “pure” form of the governing equations in conservation form; it is the form which we will use in the following sections. When a computer program is written to solve the equations in this pure form, the solution is stable and convergence to a steady state is achieved.

*A comment:* The behavior discussed above, namely, that instabilities are sometimes encountered when  $F_1$ ,  $F_2$ , and  $F_3$  are constructed in terms of the primitive variables, whereas a stable solution is obtained when  $F_1$ ,  $F_2$ , and  $F_3$  are constructed in terms of  $U_1$ ,  $U_2$ , and  $U_3$ , is one of those nonintuitive peculiarities of CFD. So what if  $F_1$ ,  $F_2$ , and  $F_3$  are written in terms of  $\rho'$ ,  $V'$ ,  $T'$ , and  $p'$  instead of

$U_1$ ,  $U_2$ ,  $U_3$ ? On a *theoretical* basis, there is no difference. However, on a numerical basis, there is a big difference—the difference between instability and stability. This author has no simple mathematical explanation for this behavior. Let us simply consider it as part of the “art” of CFD. On the other hand, we have here an example of the advantages to be obtained by writing our CFD programs using the most consistent, or pure, form of the equations and by treating all steps in the computer program in a consistent fashion, i.e., by not changing horses in midstream.

**BOUNDARY CONDITIONS.** The boundary conditions for the subsonic-supersonic isentropic flow solution using the conservation form of the governing equations are theoretically the same as discussed in the Boundary Conditions subsection in Sec. 7.3.1; i.e., at the subsonic inflow boundary two properties are held fixed and one is allowed to float, and at the supersonic outflow boundary all properties are allowed to float. In the present formulation, as before, we hold  $\rho'$  and  $T'$  fixed at the inflow boundary, both equal to 1.0, and allow  $V'$  to float. By holding  $\rho'$  fixed, then  $U_1$  at grid point  $i = 1$  is fixed, independent of time, via  $U_1 = \rho' A'$ . That is,

$$U_{1(i=1)} = (\rho' A')_{i=1} = A'_{i=1} = \text{fixed value}$$

The floating value of  $V'$  at the inflow boundary is calculated at the end of each time step by linearly extrapolating  $U_2$  from the known values at the internal grid points  $i = 2$  and 3, that is,

$$U_{2(i=1)} = 2U_{2(i=2)} - U_{2(i=3)} \quad (7.116)$$

and then obtaining  $V'$  at  $i = 1$  from Eq. (7.103). Since  $V'$  floats at the inflow boundary, so does the value of  $U_3$ , which is given by

$$U_3 = \rho' \left( \frac{e'}{\gamma - 1} + \frac{\gamma}{2} V'^2 \right) A' \quad (7.117)$$

Since  $\rho' A' = U_1$  and  $e' = T'$ , Eq. (7.117) is written as

$$U_3 = U_1 \left( \frac{T'}{\gamma - 1} + \frac{\gamma}{2} V'^2 \right) \quad (7.118)$$

The value of  $U_3$  ( $i = 1$ ) is found by inserting the value of  $V'$  at  $i = 1$ , calculated above, as well as the *fixed* value  $T' = 1$ , into Eq. (7.118). Note that the values of  $U_1$ ,  $U_2$ , and  $U_3$  calculated at grid point  $i = 1$  are used in turn to obtain the values of the flux terms  $F_1$ ,  $F_2$ , and  $F_3$  at grid point  $i = 1$ . These values of the flux terms at the inflow boundary are needed to form the rearward differences that appear in Eqs. (7.101a) to (7.101c) during the corrector step of MacCormack’s technique. The values of  $F_1$ ,  $F_2$ , and  $F_3$  at the inflow boundary are calculated from Eqs. (7.108), (7.110), and (7.112), respectively, using  $U_1$ ,  $U_2$ , and  $U_3$  at grid point  $i = 1$ .

The flow properties at the downstream, supersonic outflow boundary are obtained by linear extrapolation from the two adjacent internal points. If  $N$  denotes the grid point at the outflow boundary, then

$$(U_1)_N = 2(U_1)_{N-1} - (U_1)_{N-2} \quad (7.119a)$$

$$(U_2)_N = 2(U_2)_{N-1} - (U_2)_{N-2} \quad (7.119b)$$

$$(U_3)_N = 2(U_3)_{N-1} - (U_3)_{N-2} \quad (7.119c)$$

The values of  $F_1$ ,  $F_2$ , and  $F_3$  at grid point  $i = N$  are obtained from the values of  $U_1$ ,  $U_2$ , and  $U_3$  at point  $i = N$ , using Eqs. (7.108), (7.110), and (7.112), respectively. These flux values are needed to form the forward differences that appear in Eqs. (7.101a) to (7.101c) during the predictor step of MacCormack's technique. Of course, the primitive variables at the downstream outflow boundary are obtained from Eqs. (7.102) to (7.105).

**INITIAL CONDITIONS.** Since the dependent variables being solved in Eqs. (7.101a) to (7.101c) are  $U_1$ ,  $U_2$ , and  $U_3$ , we need initial conditions for these same variables at time  $t = 0$  in order to start the finite-difference solution. The initial conditions for  $U_1$ ,  $U_2$ , and  $U_3$  also allow initial conditions for  $F_1$ ,  $F_2$ , and  $F_3$  to be obtained from Eqs. (7.108), (7.110), and (7.112), respectively. Such initial conditions for  $F_1$ ,  $F_2$ , and  $F_3$  are needed to form the  $x$  derivatives on the right-hand sides of Eqs. (7.101a) to (7.101c) at the first time step.

For the present calculations the same nozzle shape as given by Eq. (7.73) is used. The initial conditions for  $U_1$ ,  $U_2$ , and  $U_3$  were synthesized by assuming the following variations of  $\rho'$  and  $T'$ :

$$\rho' = 1.0 \quad \left. \begin{array}{l} \\ T' = 1.0 \end{array} \right\} \text{for } 0 \leq x' \leq 0.5 \quad (7.120a)$$

$$\left. \begin{array}{l} \\ T' = 1.0 - 0.167(x' - 0.5) \end{array} \right\} \text{for } 0.5 \leq x' \leq 1.5 \quad (7.120b)$$

$$\left. \begin{array}{l} \rho' = 1.0 - 0.366(x' - 0.5) \\ T' = 1.0 - 0.167(x' - 0.5) \end{array} \right\} \text{for } 1.5 \leq x' \leq 3.5 \quad (7.120c)$$

$$\left. \begin{array}{l} \rho' = 0.634 - 0.3879(x' - 1.5) \\ T' = 0.833 - 0.3507(x' - 1.5) \end{array} \right\} \text{for } 1.5 \leq x' \leq 3.5 \quad (7.120d)$$

$$\left. \begin{array}{l} \rho' = 0.634 - 0.3879(x' - 1.5) \\ T' = 0.833 - 0.3507(x' - 1.5) \end{array} \right\} \text{for } 1.5 \leq x' \leq 3.5 \quad (7.120e)$$

$$\left. \begin{array}{l} \rho' = 0.634 - 0.3879(x' - 1.5) \\ T' = 0.833 - 0.3507(x' - 1.5) \end{array} \right\} \text{for } 1.5 \leq x' \leq 3.5 \quad (7.120f)$$

These variations are slightly more realistic than those assumed in the Nozzle Shape and Initial Conditions subsection of Sec. 7.3.1; this is in anticipation that the stability behavior of the finite-difference formulation using the conservation form of the governing equations might be slightly more sensitive, and therefore it is useful to start with more improved initial conditions than those given in Sec. 7.3.1 by Eqs. (7.74a) to (7.74c). The initial condition for the variation of  $V'$  is synthesized by taking advantage of the fact that one of the dependent variables in our governing equations, namely,  $U_2$ , is physically the local mass flow; that is,  $U_2 = \rho'A'V'$ . Therefore, *for the initial conditions only*, let us assume a constant mass flow through the nozzle and calculate  $V'$  as

$$V' = \frac{U_2}{\rho'A'} = \frac{0.59}{\rho'A'} \quad (7.121)$$

The value 0.59 is chosen for  $U_2$  because it is close to the exact analytical value of the steady-state mass flow (which for this case is 0.579). Therefore, the initial condition for  $V'$  as a function of  $x'$  is obtained by substituting the  $\rho'$  variation given by Eqs. (7.120a), (7.120c), and (7.120e) into Eq. (7.121). Finally, the initial conditions for  $U_1$ ,  $U_2$ ,  $U_3$  are obtained by substituting the above variations for  $\rho'$ ,  $T'$ , and  $V'$  into the definitions given in Sec. 7.5.1, namely,

$$U_1 = \rho' A' \quad (7.122a)$$

$$U_2 = \rho' A' V' \quad (7.122b)$$

$$U_3 = \rho' \left( \frac{e'}{\gamma - 1} + \frac{\gamma}{2} V'^2 \right) A' \quad (7.122c)$$

where  $e' = T'$ . Of course, for the initial conditions described above,  $V'$  is calculated such that  $U_2 = \rho' A' V' = 0.59$ .

**TIME STEP CALCULATION.** The governing equations for unsteady, quasi-one-dimensional flow in *conservation* form are hyperbolic partial differential equations, just as are the governing equations in *nonconservation* form which are employed in Sec. 7.3. Therefore, for an explicit finite-difference solution, the stability criterion for the time step increment  $\Delta t$  is specified by the CFL criterion. In turn, for the calculations in the present section, the value of  $\Delta t$  is obtained precisely as described in Sec. 7.3.1 and given by Eqs. (7.67) to (7.69). Hence, no further elaboration is given here.

### 7.5.3 Intermediate Calculations: The First Time Step

In the same spirit as Sec. 7.3.2, which gave some intermediate calculations using the nonconservation form of the governing equations, we carry out the same idea in the present section for the conservation form. Since the sequence of calculations is somewhat modified when the conservation form is used, it will be useful to go through some of the details of the computation for the first time step. As explained earlier, the presentation of these intermediate results will not only be instructional but they will also allow you to check the accuracy of your computer program, should you choose to write one for the solution of the present problem.

The nozzle shape and initial conditions for the present calculations are given in Table 7.9. The nozzle shape is the same as used for the calculations in Sec. 7.3 and is sketched in Fig. 7.8. The current initial conditions are different from those used in Sec. 7.3, principally to take advantage of the fact that  $U_2$  is the local mass flow, and following the adage that we should choose initial conditions as intelligently as possible, we assume an initial constant mass flow distribution through the nozzle. This is obvious from the column labeled  $\dot{m}$  in Table 7.9. Here,  $\dot{m}$  is nondimensional, denoted by  $\dot{m} = \rho A V / \rho_0 A^* a_0$ . The values of  $\rho'$ ,  $T'$ , and  $V'$  in Table 7.9 are obtained from Eqs. (7.120a) to (7.120f) and (7.121), respectively. Also shown in Table 7.9 are the corresponding initial conditions for  $U_1$ ,  $U_2$ , and  $U_3$ , obtained from Eqs. (7.122a) to (7.122c), respectively.

**TABLE 7.9**  
Initial conditions for the case using the conservation form

$\frac{x}{L}$	$\frac{A}{A^*}$	$\frac{\rho}{\rho_0}$	$\frac{V}{a_0}$	$\frac{T}{T_0}$	$\dot{m}$	$U_1$	$U_2$	$U_3$
0.000	5.950	1.000	0.099	1.000	0.590	5.950	0.590	14.916
0.100	5.312	1.000	0.111	1.000	0.590	5.312	0.590	13.326
0.200	4.718	1.000	0.125	1.000	0.590	4.718	0.590	11.847
0.300	4.168	1.000	0.142	1.000	0.590	4.168	0.590	10.478
0.400	3.662	1.000	0.161	1.000	0.590	3.662	0.590	9.222
0.500	3.200	1.000	0.184	1.000	0.590	3.200	0.590	8.076
0.600	2.782	0.963	0.220	0.983	0.590	2.680	0.590	6.679
0.700	2.408	0.927	0.264	0.967	0.590	2.232	0.590	5.502
0.800	2.078	0.890	0.319	0.950	0.590	1.850	0.590	4.525
0.900	1.792	0.854	0.386	0.933	0.590	1.530	0.590	3.728
1.000	1.550	0.817	0.466	0.916	0.590	1.266	0.590	3.094
1.100	1.352	0.780	0.559	0.900	0.590	1.055	0.590	2.604
1.200	1.198	0.744	0.662	0.883	0.590	0.891	0.590	2.241
1.300	1.088	0.707	0.767	0.866	0.590	0.769	0.590	1.983
1.400	1.022	0.671	0.861	0.850	0.590	0.685	0.590	1.811
1.500	1.000	0.634	0.931	0.833	0.590	0.634	0.590	1.705
1.600	1.022	0.595	0.970	0.798	0.590	0.608	0.590	1.614
1.700	1.088	0.556	0.975	0.763	0.590	0.605	0.590	1.557
1.800	1.198	0.518	0.951	0.728	0.590	0.620	0.590	1.521
1.900	1.352	0.479	0.911	0.693	0.590	0.647	0.590	1.498
2.000	1.550	0.440	0.865	0.658	0.590	0.682	0.590	1.479
2.100	1.792	0.401	0.821	0.623	0.590	0.719	0.590	1.458
2.200	2.078	0.362	0.783	0.588	0.590	0.753	0.590	1.430
2.300	2.408	0.324	0.757	0.552	0.590	0.779	0.590	1.389
2.400	2.782	0.285	0.744	0.517	0.590	0.793	0.590	1.333
2.500	3.200	0.246	0.749	0.482	0.590	0.788	0.590	1.259
2.600	3.662	0.207	0.777	0.477	0.590	0.759	0.590	1.170
2.700	4.168	0.169	0.840	0.412	0.590	0.702	0.590	1.071
2.800	4.718	0.130	0.964	0.377	0.590	0.612	0.590	0.975
2.900	5.312	0.091	1.221	0.342	0.590	0.483	0.590	0.917
3.000	5.950	0.052	1.901	0.307	0.590	0.310	0.590	1.023

To illustrate the intermediate calculations, let us focus on grid point  $i = 16$ , which, as seen in Fig. 7.8, is at the throat of the nozzle. We will follow MacCormack's explicit predictor-corrector technique, described at length in previous sections.

**Predictor step.** To start the calculation, we use the initial conditions for  $U_1$ ,  $U_2$ , and  $U_3$  to calculate the initial values of  $F_1$ ,  $F_2$ , and  $F_3$  at grid points  $i = 16$  and 17. From Table 7.9, the initial values for the  $U$ 's are

$$(U_1)_{i=16} = 0.634 \quad (U_2)_{i=16} = 0.590 \quad (U_3)_{i=16} = 1.705$$

$$(U_1)_{i=17} = 0.608 \quad (U_2)_{i=17} = 0.590 \quad (U_3)_{i=17} = 1.614$$

From Eq. (7.108)

$$(F_1)_{i=16} = (U_2)_{i=16} = \boxed{0.590}$$

$$(F_1)_{i=17} = (U_2)_{i=17} = \boxed{0.590}$$

From Eq. (7.110)

$$\begin{aligned} (F_2)_{i=16} &= \left[ \frac{U_2^2}{U_1} + \frac{\gamma - 1}{\gamma} \left( U_3 - \frac{\gamma}{2} \frac{U_2^2}{U_1} \right) \right]_{i=16} \\ &= \frac{(0.590)^2}{0.634} + \frac{0.4}{1.4} \left[ 1.705 - 0.7 \frac{(0.590)^2}{0.634} \right] \\ &= \boxed{0.926} \\ (F_2)_{i=17} &= \frac{(0.590)^2}{0.608} + \frac{0.4}{1.4} \left[ 1.614 - 0.7 \frac{(0.590)^2}{0.608} \right] \\ &= \boxed{0.919} \end{aligned}$$

From Eq. (7.112)

$$\begin{aligned} (F_3)_{i=16} &= \left[ \frac{\gamma U_2 U_3}{U_1} - \frac{\gamma(\gamma - 1)}{2} \frac{U_2^3}{U_1^2} \right]_{i=16} \\ &= \frac{1.4(0.590)(1.705)}{0.634} - \frac{1.4(0.4)(0.590)^3}{2(0.634)^2} \\ &= \boxed{2.078} \\ (F_3)_{i=17} &= \frac{1.4(0.590)(1.614)}{0.608} - \frac{1.4(0.4)(0.590)^3}{2(0.608)^2} \\ &= \boxed{2.036} \end{aligned}$$

From Eq. (7.113) we have

$$J_2 = \frac{1}{\gamma} p' \frac{\partial A'}{\partial x'} = \frac{1}{\gamma} \rho' T' \frac{\partial A'}{\partial x'}$$

Hence  $(J_2)_{i=16} = \frac{1}{1.4} (0.634)(0.833) \left( \frac{1.022 - 1.0}{0.1} \right) = 0.083$

Note that by using Eq. (7.113) for  $J_2$  rather than the expression given by Eq. (7.115), we are breaking slightly with the purity of the governing equations as described in the first subsection of Sec. 7.5.2. This is being done for simplicity [Eq. (7.113) is much shorter than Eq. (7.115)]. The results are not compromised. The

value of  $\Delta x'$  is  $L/N$ , where  $L$  is the length of the nozzle and  $N$  is the number of increments along the nozzle, which for the present case is 30. Hence

$$\Delta x' = \frac{L}{N} = \frac{3.0}{30} = 0.1$$

From Eq. (7.101a), using forward differences for the  $x$  derivatives, we have

$$\left( \frac{\partial U_1}{\partial t'} \right)_{i=16}^{t'} = - \frac{(F_1)_{i=17} - (F_1)_{i=16}}{\Delta x'} = - \frac{0.590 - 0.590}{0.1} = \boxed{0}$$

From Eq. (7.101b), we have

$$\begin{aligned} \left( \frac{\partial U_2}{\partial t'} \right)_{i=16}^{t'} &= - \frac{(F_2)_{i=17} - (F_2)_{i=16}}{\Delta x'} + J_2 \\ &= - \frac{0.919 - 0.926}{0.1} + 0.083 = \boxed{0.156} \end{aligned}$$

(Please note: Once again, remember that since we are giving the numbers in the present section to three decimal places, if you are following along with a hand calculator using these three-place figures, some small numerical errors may result in your hand calculations. In the above, and throughout this section, the numbers that appear in boxes are the exact numbers that came from the author's Macintosh computer.) Finally, from Eq. (7.101c), we have

$$\left( \frac{\partial U_3}{\partial t'} \right)_{i=16}^{t'} = - \frac{(F_3)_{i=17} - (F_3)_{i=16}}{\Delta x'} = - \frac{2.036 - 2.078}{0.1} = \boxed{0.416}$$

To obtain the predicted values of the flow quantities, we must first obtain the value of the time step  $\Delta t'$ . This is carried out as mentioned in the last subsection of Sec. 7.5.2 and as given by Eqs. (7.67) to (7.69) in Sec. 7.3.1. After scanning all the grid points from  $i = 1$  to  $i = 31$ , the minimum value of  $\Delta t'$  is found to be, using a Courant number of  $C = 0.5$ ,

$$\Delta t' = 0.0267$$

We proceed to find the predicted values of  $U_1$ ,  $U_2$ , and  $U_3$ , denoted by the barred quantities.

$$\begin{aligned} (\bar{U}_1)_{i=16}^{t'+\Delta t'} &= (U_1)_{i=16}^{t'} + \left( \frac{\partial U_1}{\partial t'} \right)_{i=16}^{t'} \Delta t' \\ &= 0.634 + 0\Delta t' = \boxed{0.634} \\ (\bar{U}_2)_{i=16}^{t'+\Delta t'} &= (U_2)_{i=16}^{t'} + \left( \frac{\partial U_2}{\partial t'} \right)_{i=16}^{t'} \Delta t' \\ &= 0.590 + 0.156(0.0267) = \boxed{0.594} \\ (\bar{U}_3)_{i=16}^{t'+\Delta t'} &= (U_3)_{i=16}^{t'} + \left( \frac{\partial U_3}{\partial t'} \right)_{i=16}^{t'} \Delta t' \\ &= 1.705 + 0.416(0.0267) = \boxed{1.716} \end{aligned}$$

At this stage, the *predicted* values of the primitive variables can be decoded from  $\bar{U}_1$ ,  $\bar{U}_2$ , and  $\bar{U}_3$ , using Eqs. (7.102) to (7.105). For example, from Eq. (7.102),

$$(\bar{\rho}')_{i=16}^{t'+\Delta t'} = \frac{(\bar{U}_1)_{i=16}^{t'+\Delta t'}}{(\bar{A}')_{i=16}} = \frac{0.634}{1.0} = \boxed{0.634}$$

and from Eqs. (7.103) and (7.104),

$$\begin{aligned} (\bar{T}')_{i=16}^{t'+\Delta t'} &= (\gamma - 1) \left\{ \frac{(\bar{U}_3)_{i=16}^{t'+\Delta t'}}{(\bar{U}_1)_{i=16}^{t'+\Delta t'}} - \frac{\gamma}{2} \left[ \frac{(\bar{U}_2)_{i=16}^{t'+\Delta t'}}{(\bar{U}_1)_{i=16}^{t'+\Delta t'}} \right]^2 \right\} \\ &= 0.4 \left[ \frac{1.716}{0.634} - 0.7 \left( \frac{0.594}{0.634} \right)^2 \right] = \boxed{0.837} \end{aligned}$$

The above numbers for the predicted  $\rho'$  and  $T'$  will be needed on the corrector step. Before we move on to the corrector step, we need to find the predicted values of  $F_1$ ,  $F_2$ , and  $F_3$  at grid points  $i = 15$  and  $16$ ; these values for  $i = 16$  are based on the predicted values of  $U_1$ ,  $U_2$ , and  $U_3$  found above, and for  $i = 15$  are based on the predicted values of  $U_1$ ,  $U_2$ , and  $U_3$  for  $i = 15$  (not recorded above in order to not let the length of this section get out of hand). The predicted fluxes, obtained from Eqs. (7.108), (7.110), and (7.112) using  $\bar{U}_1$ ,  $\bar{U}_2$ , and  $\bar{U}_3$ , are

$$\begin{aligned} (\bar{F}_1)_{i=16} &= 0.594 & (\bar{F}_2)_{i=16} &= 0.936 & (\bar{F}_3)_{i=16} &= 2.105 \\ (\bar{F}_1)_{i=15} &= 0.585 & (\bar{F}_2)_{i=15} &= 0.915 & (\bar{F}_3)_{i=15} &= 2.037 \end{aligned}$$

**Corrector step.** The predicted time derivatives of  $U_1$ ,  $U_2$ , and  $U_3$  are obtained from Eqs. (7.101a) to (7.101c), respectively, using rearward differences for the  $x$  derivatives. From Eq. (7.101a)

$$\begin{aligned} \left( \frac{\partial \bar{U}_1}{\partial t'} \right)_{i=16}^{t'+\Delta t'} &= - \frac{(\bar{F}_1)_{i=16} - (\bar{F}_1)_{i=15}}{\Delta x'} \\ &= - \frac{0.594 - 0.585}{0.1} = \boxed{-0.0918} \end{aligned}$$

From Eq. (7.101b)

$$\begin{aligned} \left( \frac{\partial \bar{U}_2}{\partial t'} \right)_{i=16}^{t'+\Delta t'} &= - \frac{(\bar{F}_2)_{i=16} - (\bar{F}_2)_{i=15}}{\Delta x'} + \frac{1}{\gamma} \bar{\rho}' \bar{T}' \frac{\partial A'}{\partial x'} \\ &= - \frac{0.936 - 0.915}{0.1} + \frac{1}{1.4} (0.634)(0.837) \left( \frac{1.0 - 1.022}{0.1} \right) \\ &= \boxed{-0.290} \end{aligned}$$

From Eq. (7.101c)

$$\begin{aligned} \left( \frac{\partial \bar{U}_3}{\partial t'} \right)_{i=16}^{t'+\Delta t'} &= - \frac{(\bar{F}_3)_{i=16} - (\bar{F}_3)_{i=15}}{\Delta x'} \\ &= - \frac{2.105 - 2.037}{0.1} = \boxed{-0.679} \end{aligned}$$

The average time derivatives are formed as follows.

$$\begin{aligned} \left( \frac{\partial U_1}{\partial t} \right)_{av} &= \frac{1}{2} \left[ \left( \frac{\partial U_1}{\partial t'} \right)_{i=16}^{t'} + \left( \frac{\partial \bar{U}_1}{\partial t'} \right)_{i=16}^{t'+\Delta t'} \right] \\ &= 0.5(0 - 0.0918) = \boxed{-0.0459} \\ \left( \frac{\partial U_2}{\partial t} \right)_{av} &= \frac{1}{2} \left[ \left( \frac{\partial U_2}{\partial t'} \right)_{i=16}^{t'} + \left( \frac{\partial \bar{U}_2}{\partial t'} \right)_{i=16}^{t'+\Delta t'} \right] \\ &= 0.5(0.156 - 0.290) = \boxed{-0.0668} \\ \left( \frac{\partial U_3}{\partial t} \right)_{av} &= \frac{1}{2} \left[ \left( \frac{\partial U_3}{\partial t'} \right)_{i=16}^{t'} + \left( \frac{\partial \bar{U}_3}{\partial t'} \right)_{i=16}^{t'+\Delta t'} \right] \\ &= 0.5(0.416 - 0.679) = \boxed{-0.131} \end{aligned}$$

The final *corrected* values of  $U_1$ ,  $U_2$ , and  $U_3$  at time step  $t' + \Delta t'$  (here, since  $t' = 0$  to start with, we are calculating the final *corrected* values at time  $t' = \Delta t'$ ) are obtained from

$$\begin{aligned} (U_1)_{i=16}^{t'+\Delta t'} &= (U_1)_{i=16}^{t'} + \left( \frac{\partial U_1}{\partial t'} \right)_{av} \Delta t \\ &= 0.634 + (-0.0459)(0.0267) = \boxed{0.633} \\ (U_2)_{i=16}^{t'+\Delta t'} &= (U_2)_{i=16}^{t'} + \left( \frac{\partial U_2}{\partial t'} \right)_{av} \Delta t \\ &= 0.590 + (-0.0668)(0.0267) = \boxed{0.588} \\ (U_3)_{i=16}^{t'+\Delta t'} &= (U_3)_{i=16}^{t'} + \left( \frac{\partial U_3}{\partial t'} \right)_{av} \Delta t \\ &= 1.705 + (-0.131)(0.0267) = \boxed{1.701} \end{aligned}$$

Finally, the corrected values of the primitive variables are obtained by decoding  $U_1$ ,  $U_2$ , and  $U_3$ , obtained above, via Eqs. (7.102) to (7.105). That is, from Eq. (7.102),

$$(\rho')_{i=16}^{t'+\Delta t'} = (U_1)_{i=16}^{t'+\Delta t'} = \frac{0.633}{1} = \boxed{0.633}$$

From Eq. (7.103)

$$(V')_{i=16}^{t'+\Delta t'} = \left( \frac{U_2}{U_1} \right)_{i=16}^{t'+\Delta t'} = \frac{0.588}{0.633} = \boxed{0.930}$$

From Eq. (7.104)

$$\begin{aligned} (T')_{i=16}^{t'+\Delta t'} &= (\gamma - 1) \left( \frac{U_3}{U_1} - \frac{\gamma}{2} V'^2 \right)_{i=16}^{t'+\Delta t'} \\ &= 0.4 \left[ \frac{1.701}{0.633} - 0.7(0.930)^2 \right] = \boxed{0.833} \end{aligned}$$

This brings to an end the calculations of the flow properties at grid point  $i = 16$  at time  $t' = \Delta t'$ . This process is repeated for all the interior grid points distributed along the nozzle. The properties at the inflow and outflow boundaries are calculated as described in the Boundary Conditions subsection of Sec. 7.5.2. By this stage, since you are most likely saturated with numbers, we will spare you the details.

For the sake of reference and so that you can check the numbers from your own computer program, the flow-field variables, including  $U_1$ ,  $U_2$ , and  $U_3$ , obtained after the first time step at all the grid points are tabulated in Table 7.10. Comparing the numbers in Table 7.10 with the initial conditions given in Table 7.9, we see that the largest changes over the first time step have taken place near the exit of the nozzle and that the mass flow distribution, originally chosen as constant at  $t' = 0$ , is no longer constant after the first time step.

#### 7.5.4 Final Numerical Results: The Steady-State Solution

The steady-state results obtained from the time-marching solution of the governing equations in conservation form are essentially the same as those obtained using the nonconservation form (described in Sec. 7.3.3), with a few slight, but notable differences. The present converged solution is tabulated in Table 7.11, which are the results obtained after 1400 time steps. A quick comparison of the numbers given in Tables 7.11 (for conservation form) and 7.3 (for nonconservation form) show little material difference. We conclude that, for all practical purposes, both forms of the governing equations give the same results. This is as it should be; the flow problem studied in both tables is the isentropic, subsonic-supersonic flow through a nozzle, and for such a flow the choice of the form of equations is not important. However, as described in Sec. 2.10, an important numerical distinction between the nonconservation and conservation forms of the equations is related to problems dealing with shock capturing, and we are not capturing any shocks in the present problem.

Let us highlight some of the slight but notable differences mentioned above. The most dramatic difference is in the mass flow distribution. First of all, with the initial conditions assuming a constant mass flow, it is interesting to examine the variation of  $\dot{m}$  with  $x/L$  at a few different times during the convergence toward the

**TABLE 7.10**  
Flow-field variables at the end of the first time step

$\frac{x}{L}$	$\frac{A}{A^*}$	$\frac{\rho}{\rho_0}$	$\frac{V}{a_0}$	$\frac{T}{T_0}$	$\frac{p}{p_0}$	$M$	$\dot{m}$	$U_1$	$U_2$	$U_3$
0.000	5.950	1.000	0.099	1.000	1.000	0.099	0.588	5.950	0.588	14.916
0.100	5.312	1.000	0.111	1.000	1.000	0.111	0.588	5.312	0.588	13.326
0.200	4.718	1.000	0.125	1.000	1.000	0.125	0.588	4.718	0.588	11.846
0.300	4.168	1.000	0.141	1.000	1.000	0.141	0.587	4.168	0.587	10.478
0.400	3.662	1.000	0.160	1.000	1.000	0.160	0.587	3.662	0.587	9.221
0.500	3.200	0.999	0.187	1.000	0.999	0.187	0.598	3.197	0.598	8.067
0.600	2.782	0.963	0.228	0.983	0.947	0.230	0.611	2.679	0.611	6.682
0.700	2.408	0.927	0.271	0.967	0.897	0.276	0.606	2.233	0.606	5.513
0.800	2.078	0.891	0.325	0.950	0.846	0.333	0.601	1.851	0.601	4.534
0.900	1.792	0.854	0.389	0.934	0.798	0.403	0.596	1.531	0.596	3.735
1.000	1.550	0.818	0.467	0.917	0.750	0.487	0.592	1.268	0.592	3.098
1.100	1.352	0.781	0.557	0.900	0.703	0.587	0.588	1.056	0.588	2.605
1.200	1.198	0.744	0.656	0.883	0.657	0.698	0.585	0.892	0.585	2.238
1.300	1.088	0.707	0.759	0.866	0.613	0.815	0.584	0.770	0.584	1.977
1.400	1.022	0.670	0.854	0.849	0.569	0.927	0.585	0.685	0.585	1.804
1.500	1.000	0.633	0.930	0.833	0.527	1.018	0.588	0.633	0.588	1.701
1.600	1.022	0.594	0.979	0.800	0.475	1.094	0.594	0.607	0.594	1.621
1.700	1.088	0.555	0.992	0.766	0.425	1.134	0.599	0.604	0.599	1.572
1.800	1.198	0.517	0.975	0.731	0.377	1.141	0.604	0.619	0.604	1.542
1.900	1.352	0.478	0.939	0.695	0.333	1.126	0.607	0.647	0.607	1.523
2.000	1.550	0.440	0.893	0.660	0.290	1.099	0.609	0.682	0.609	1.506
2.100	1.792	0.401	0.848	0.625	0.251	1.073	0.610	0.719	0.610	1.485
2.200	2.078	0.362	0.809	0.590	0.214	1.054	0.610	0.753	0.610	1.456
2.300	2.408	0.324	0.781	0.554	0.179	1.049	0.609	0.780	0.609	1.413
2.400	2.782	0.285	0.766	0.519	0.148	1.063	0.607	0.793	0.607	1.354
2.500	3.200	0.246	0.768	0.484	0.119	1.104	0.605	0.788	0.605	1.278
2.600	3.662	0.208	0.791	0.448	0.093	1.182	0.601	0.760	0.601	1.184
2.700	4.168	0.169	0.846	0.412	0.070	1.318	0.595	0.704	0.595	1.078
2.800	4.718	0.131	0.949	0.375	0.049	1.551	0.584	0.616	0.584	0.965
2.900	5.312	0.093	1.133	0.324	0.030	1.990	0.560	0.494	0.560	0.846
3.000	5.950	0.063	1.438	0.200	0.013	3.217	0.536	0.373	0.536	0.726

steady state. This is shown in Fig. 7.19, where the nondimensional mass flow is plotted verus  $x/L$  for several different values of time. The dashed line labeled  $0\Delta t$  represents the assumed initial conditions. Note that the transient mass flow deviates away from the initial conditions; the result after 100 time steps (labeled  $100\Delta t$ ) shows a somewhat “humped” distribution. After 200 time steps (labeled  $200\Delta t$ ), the mass flow distribution is becoming more constant, and after 700 time steps (labeled  $700\Delta t$ ), it is almost (but not quite) equal to a constant value. Moreover, it is quite close to the exact analytical value of 0.579. Comparing Fig. 7.19 with the corresponding results obtained with the nonconservation form of the equations as plotted in Fig. 7.11, we see that the present variations in mass flow are much less severe. Of course, this is comparing apples and oranges, because Figs. 7.11 and 7.19 correspond to different initial conditions. We can suppose that the milder behavior

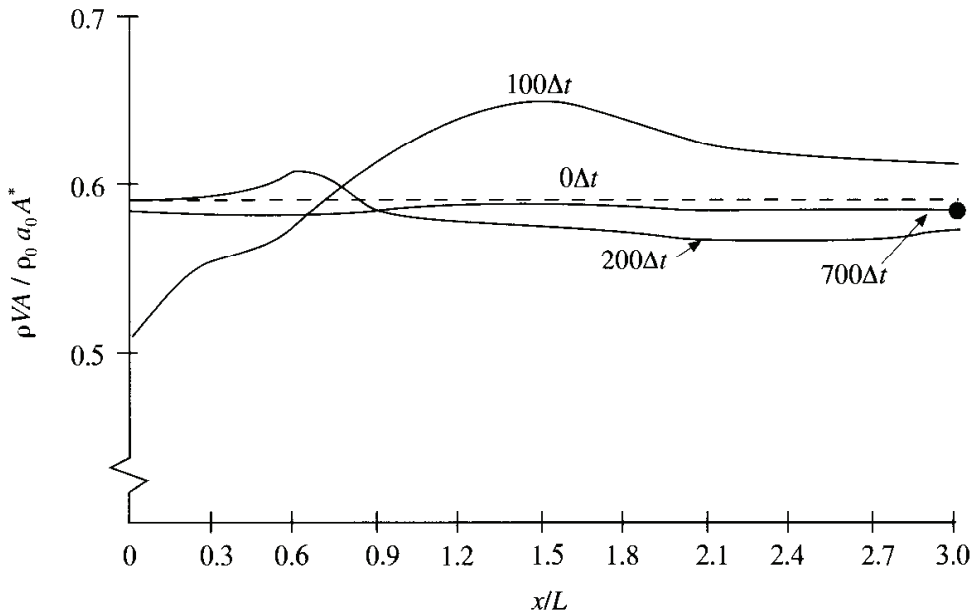
**TABLE 7.11**  
Steady-state results, using the conservation form

$\frac{x}{L}$	$\frac{A}{A^*}$	$\frac{\rho}{\rho_0}$	$\frac{V}{a_0}$	$\frac{T}{T_0}$	$\frac{p}{p_0}$	$M$	$\dot{m}$	$U_1$	$U_2$	$U_3$
0.000	5.950	1.000	0.098	1.000	1.000	0.098	0.583	5.950	0.583	14.915
0.100	5.312	0.999	0.110	0.999	0.998	0.110	0.583	5.306	0.583	13.301
0.200	4.718	0.997	0.124	0.999	0.996	0.124	0.583	4.704	0.583	11.798
0.300	4.168	0.995	0.141	0.998	0.993	0.141	0.583	4.147	0.583	10.404
0.400	3.662	0.992	0.161	0.997	0.989	0.161	0.583	3.633	0.583	9.118
0.500	3.200	0.988	0.184	0.995	0.983	0.185	0.583	3.161	0.583	7.941
0.600	2.782	0.982	0.213	0.993	0.975	0.214	0.583	2.732	0.583	6.869
0.700	2.408	0.974	0.249	0.989	0.964	0.250	0.584	2.345	0.584	5.903
0.800	2.078	0.962	0.292	0.985	0.948	0.294	0.584	2.000	0.584	5.043
0.900	1.792	0.946	0.344	0.978	0.926	0.348	0.584	1.696	0.584	4.287
1.000	1.550	0.923	0.408	0.969	0.894	0.415	0.584	1.431	0.584	3.632
1.100	1.352	0.891	0.485	0.955	0.851	0.496	0.585	1.205	0.585	3.075
1.200	1.198	0.847	0.577	0.935	0.792	0.596	0.585	1.015	0.585	2.609
1.300	1.088	0.789	0.682	0.909	0.718	0.715	0.585	0.859	0.585	2.231
1.400	1.022	0.718	0.798	0.874	0.628	0.854	0.586	0.734	0.586	1.932
1.500	1.000	0.648	0.904	0.839	0.544	0.987	0.586	0.648	0.586	1.730
1.600	1.022	0.548	1.046	0.783	0.429	1.182	0.586	0.560	0.586	1.525
1.700	1.088	0.462	1.164	0.731	0.338	1.361	0.585	0.503	0.585	1.396
1.800	1.198	0.384	1.272	0.679	0.261	1.544	0.585	0.460	0.585	1.301
1.900	1.352	0.316	1.368	0.628	0.198	1.726	0.585	0.427	0.585	1.231
2.000	1.550	0.260	1.452	0.581	0.151	1.905	0.584	0.402	0.584	1.178
2.100	1.792	0.214	1.524	0.538	0.115	2.077	0.584	0.383	0.584	1.138
2.200	2.078	0.177	1.586	0.500	0.088	2.243	0.583	0.368	0.583	1.107
2.300	2.408	0.148	1.639	0.466	0.069	2.402	0.583	0.356	0.583	1.083
2.400	2.782	0.124	1.685	0.436	0.054	2.554	0.583	0.346	0.583	1.064
2.500	3.200	0.106	1.725	0.409	0.043	2.698	0.583	0.338	0.583	1.048
2.600	3.662	0.090	1.760	0.384	0.035	2.838	0.582	0.331	0.582	1.035
2.700	4.168	0.078	1.790	0.363	0.028	2.969	0.582	0.325	0.582	1.025
2.800	4.718	0.068	1.817	0.344	0.023	3.100	0.582	0.320	0.582	1.015
2.900	5.312	0.060	1.840	0.327	0.019	3.216	0.582	0.316	0.582	1.008
3.000	5.950	0.052	1.863	0.310	0.016	3.345	0.582	0.312	0.582	1.001

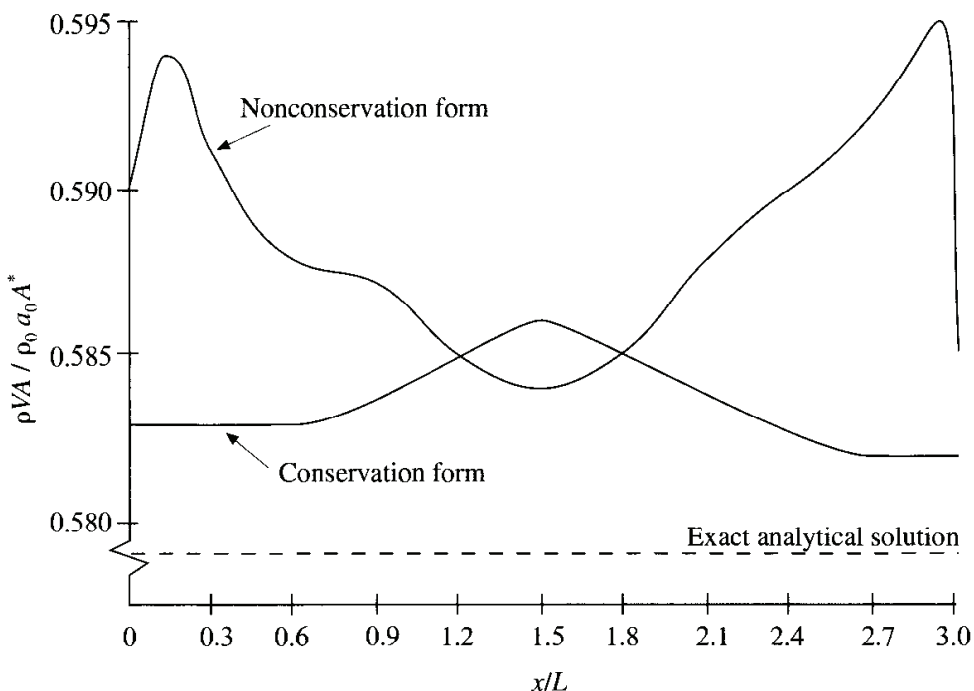
illustrated in Fig. 7.19 is due predominantly to our assumed initial condition of constant mass flow.

Let us compare the *steady-state* variations of mass flow obtained with the nonconservation and conservation forms of the governing equations (both after 1400 time steps—well beyond the time required to converge to the steady state). This comparison is shown in Fig. 7.20, in which the scale of the ordinate for mass flow is greatly magnified. Here we see that the steady-state mass flow distribution predicted by the *conservation* form of the equations is much more satisfactory than that obtained from the nonconservation form, on two accounts:

1. The conservation form gives a distribution that is much closer to being a constant. In contrast, the nonconservation results have (on the magnified scale) a

**FIG. 7.19**

Variation of mass flow distribution through the nozzle at different times during the time-marching process; solution of the conservation form of the governing equations. Circle indicates exact analytical value.

**FIG. 7.20**

A detailed comparison of the steady-state mass flow variations (on a magnified scale) obtained with the nonconservation and conservation forms of the governing flow equations.

sizeable variation, with some spurious oscillations at both the inflow and outflow boundaries. Of course, on a practical basis, when plotted on the scale shown in Fig. 7.11, these variations are not apparent, and the mass flow essentially appears to be a constant.

2. The steady-state mass flow results obtained with the conservation form are, on the whole, much closer to the exact analytical solution of  $\rho' A' V' = 0.579$ , shown in Fig. 7.20 by the dashed line.

The comparison shown in Fig. 7.20 illustrates a general advantage of the conservation form of the equations. The conservation form does a better job of preserving mass throughout the flow field, mainly because the mass flow itself is one of the dependent variables in the equations—the mass flow is a primary result from these equations. In contrast, the dependent variables in the nonconservation form of the equations are the primitive variables, and the mass flow is obtained only as a secondary result. Because the conservation form of the equations does a better job of conserving mass throughout the flow field, we can begin to understand why they are labeled the *conservation* form.

*Caution:* The above discussion does not necessarily establish a definite superiority of the conservation form results over the nonconservation form results. Quite the contrary, let us take a look at the *primitive* variables; in particular, temperature, pressure, and Mach number at the nozzle throat, as tabulated in Table 7.12. The first row gives the exact, analytical results. The second and third rows give the numerical results for the nonconservation and the conservation forms, respectively. Note that the *nonconservation form* results are distinctly closer to the exact values. The last row in Table 7.12 gives conservation form results for a grid with twice as many grid points (61 in comparison to 31 points). A comparison of the last two rows are an indication of *grid independence* for the conservation form results. Note that, by doubling the number of grid points, the steady-state numerical results are slightly closer to the exact, analytical values (but still not as close as the nonconservation form results with half as many grid points). For all practical purposes, we have grid independence with 31 grid points.

**TABLE 7.12**  
Comparison of steady-state results; conservation  
versus nonconservation form

	$\frac{\rho^*}{\rho_0}$	$\frac{T^*}{T_0}$	$\frac{p^*}{p_0}$	$M$
Exact analytical solution	0.634	0.833	0.528	1.000
Nonconservation form, numerical results (31 points)	0.639	0.836	0.534	0.999
Conservation form, numerical results (31 points)	0.648	0.839	0.544	0.987
Conservation form, numerical results (61 points)	0.644	0.838	0.540	0.989

The behavior of the residuals for the conservation form is not as good as that for the nonconservation form of the equations. For the nonconservation form, recall from Fig. 7.10 that at early times the residuals are on the order of  $10^{-1}$ , but they decay to about  $10^{-6}$  after 1400 time steps. In contrast, for the conservation form of the equations, the residuals at early times are on the order of  $10^{-1}$  but decay only to about  $10^{-3}$  after 1400 time steps. However, this is sufficient to produce the steady-state results, for all practical purposes.

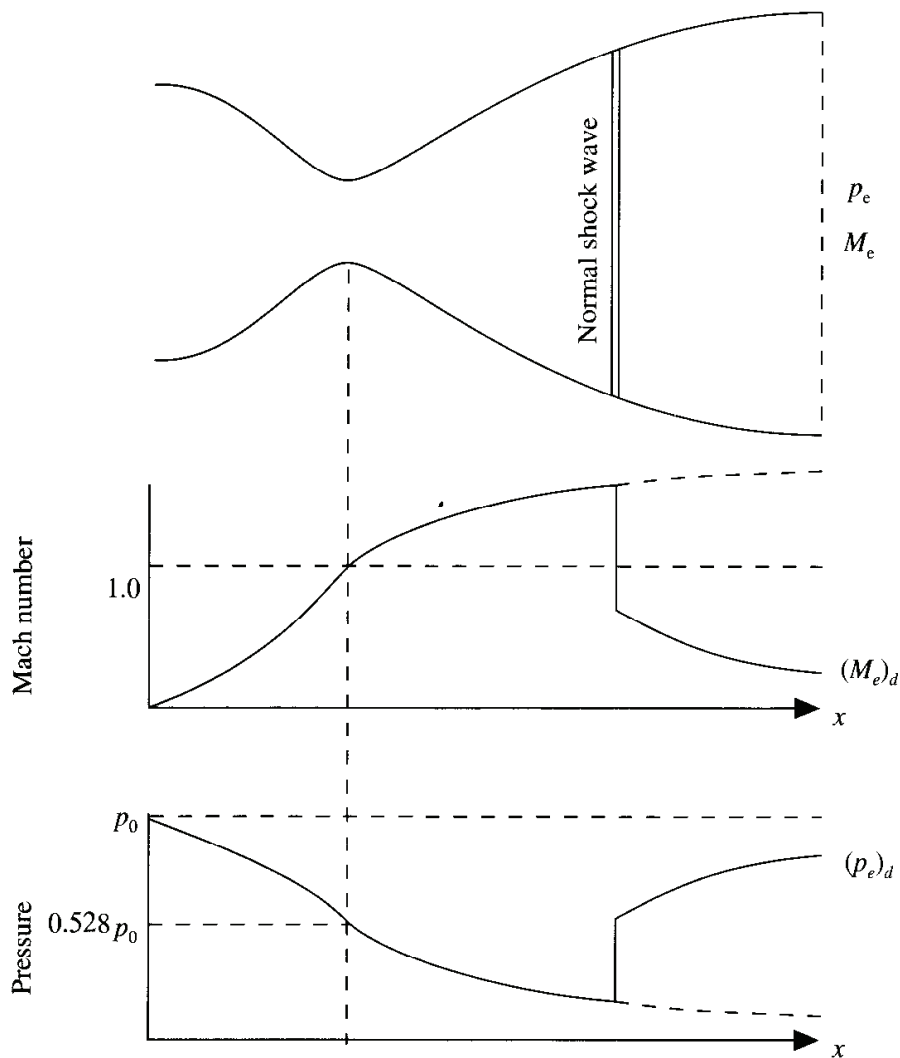
In summary, for the given flow problem, we cannot establish a clear superiority of the conservation form of the governing equations over the nonconservation form. In essence, from all our previous discussions, we can only make the following observations:

1. The conservation form yields a better mass flow distribution. The conservation form simply does a better job of conserving mass.
2. The nonconservation form leads to smaller residuals. The amount by which the residuals decay is often used as an index of “quality” of the numerical algorithm. In this sense, the nonconservation form does a better job.
3. There is no clear superiority of either form in terms of accuracy of the results. The nonconservation form seems to produce slightly more accurate results for the primitive variables, and the conservation form seems to produce slightly more accurate results for the flux variables. The results in either case are certainly satisfactory.
4. Comparing the amount of calculational effort to achieve a solution, as reflected in our extended discussions in Sec. 7.3 (nonconservation form) and Sec. 7.5 (conservation form), we note that the solution of the conservation form requires marginally more work. Most of this is due to the need to decode the primitive variables from the flux variables; such decoding is not necessary when you are solving the nonconservation form.

## 7.6 A CASE WITH SHOCK CAPTURING

In Sec. 7.2 we discussed the physical aspects of subsonic-supersonic isentropic flow. We emphasized that for a given nozzle shape there exists only one unique solution; the qualitative aspects of that solution are sketched in Fig. 7.2. Return to Fig. 7.2, and in particular focus on the pressure distribution shown in Fig. 7.2c. The pressure ratio across the nozzle,  $p_e/p_0$ , comes out as part of the solution; i.e., we do not have to *specify* it to obtain the solution. (On the other hand, in the laboratory we would have to make certain that this particular pressure ratio somehow is maintained across the nozzle, or else the subsonic-supersonic isentropic solution may not occur.) In contrast, in Sec. 7.4 we discussed the physical aspects of purely subsonic flow through the nozzle and emphasized the fact that there are an infinite number of possible isentropic flow solutions to this problem, each one corresponding to a specific value of the pressure ratio  $p_e/p_0$ . In this case, we *have to specify*  $p_e/p_0$  to obtain a unique solution. The qualitative behavior of such subsonic flow solutions is sketched in Fig. 7.13.

Return to Fig. 7.13, and let us ask the question: What happens when the exit pressure is reduced slightly *below* the value  $(p_e)_c$ ? The answer is that the nozzle becomes “choked;” i.e., the flow remains sonic at the throat, and the mass flow becomes a fixed value, no matter how much  $p_e$  is reduced below the value  $(p_e)_c$ . The flow downstream of the nozzle throat goes supersonic, following for a certain length the isentropic flow solution described in Fig. 7.2. Assume that the exit pressure is denoted by  $(p_e)_d$ , where  $(p_e)_d$  is less than  $(p_e)_c$  by a relatively small amount. In this case, a normal shock wave must form somewhere in the divergent portion of the nozzle, as sketched in Fig. 7.21. Upstream of the normal shock wave, the flow is given by the subsonic-supersonic isentropic solution. The flow, which is supersonic immediately in front of the shock, becomes subsonic immediately behind the shock. Further downstream, this subsonic flow slows within the divergent duct, with a corresponding increase in pressure. These variations are sketched in Fig. 7.21. The pressure at the exit of the nozzle is equal to  $(p_e)_d$ , which is the *imposed* pressure at the exit. The *location* of the normal shock wave within the nozzle is just right such that the static pressure increase across the shock wave plus the further static pressure

**FIG. 7.21**

Schematic of a nozzle flow with an internal normal shock wave.

increase downstream of the shock results in precisely  $(p_e)_d$  at the exit. (In contrast, the full subsonic-supersonic isentropic solution is shown by the dashed line in Fig. 7.21.) As in the case of the purely subsonic flow case, the present solution depends on the value of  $(p_e)_d$ . To have a unique solution,  $(p_e)_d$  must be *specified*. For more details on the physical nature of this type of flow, see the extensive discussion in Refs. 8 and 21.

In the present section, we will numerically solve a nozzle flow with  $p_e$  specified such that a normal shock wave will form within the nozzle. In terms of our overall development of the basics of CFD in this book, this case is important because it will illustrate the aspect of *shock capturing* within a numerical solution of the flow. The nature of shock capturing was described in Sec. 2.10. Make certain to review that section before progressing further; it is important for you to have clearly in mind the idea of shock capturing and why it is necessary to use the conservation form of the governing equations to numerically capture shock waves within a flow field. Also, reexamine Fig. 1.32c, which itemizes those various ideas that feed into this application.

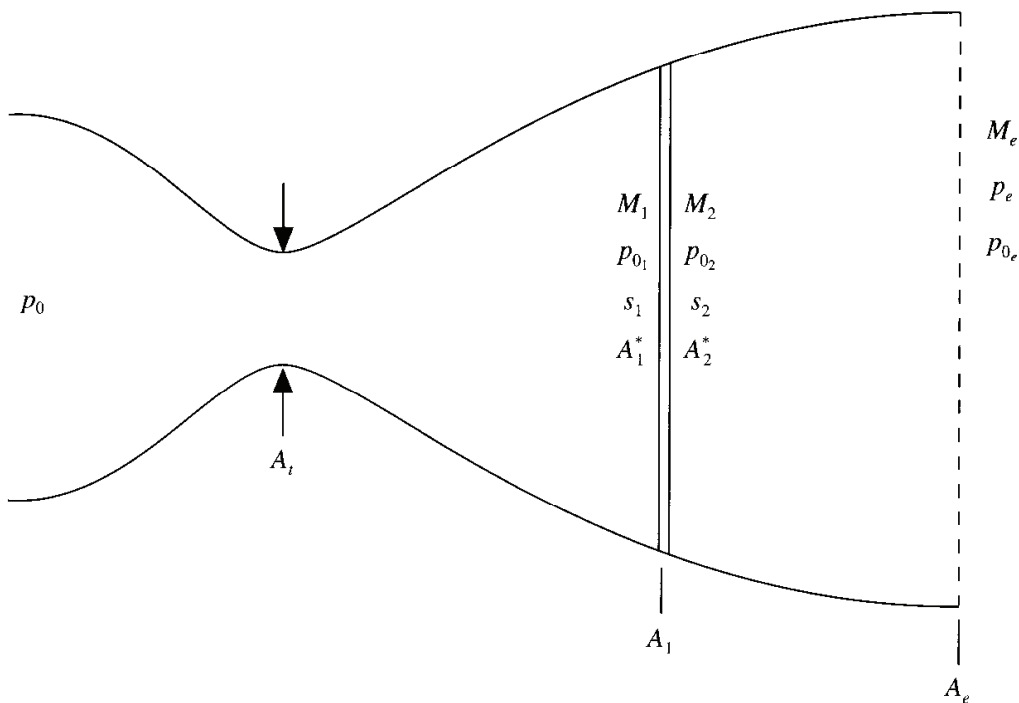
### 7.6.1 The Setup

Consider the nomenclature shown in Fig. 7.22. The normal shock wave is located at area  $A_1$ . Conditions immediately upstream of the shock are denoted with a subscript 1, and those immediately downstream of the shock are denoted with a subscript 2. The flow from the reservoir, where the pressure is  $p_0$ , to station 1 is isentropic (with constant entropy  $s_1$ ). Hence, the total pressure is constant in this flow; that is,  $p_{01} = p_0$ . The total pressure decreases across the shock (due to the entropy increase across the shock). The flow from station 2 downstream of the shock to the nozzle exit is also isentropic (with constant entropy  $s_2$ , where  $s_2 > s_1$ ). Hence the total pressure is constant in this portion of the flow, with  $(p_0)_e = p_{02}$ . Keep in mind that  $p_{02} < p_{01}$ . For the flow in front of the shock,  $A_1^*$  is a constant value, equal to the area of the sonic throat,  $A_1^* = A_t$ . However, due to the entropy increase across the shock, the value of  $A^*$  in the subsonic flow downstream of the shock, denoted by  $A_2^*$ , takes on the role of a reference value (just as in the purely subsonic case discussed in Sec. 7.4). Indeed,  $A_2^* > A_1^*$ .

In this section, we will numerically calculate the flow through a convergent-divergent nozzle under the condition where a normal shock wave exists in the divergent portion. The nozzle shape will be the same as used in Sec. 7.3, namely, that given by Eq. (7.73). We will use the governing equations in conservation form and will employ the philosophy of shock capturing. However, before jumping into the numerical solution, let us examine the exact analytical results.

**EXACT ANALYTICAL RESULTS.** For the nozzle shape specified by Eq. (7.73), the area of the exit is  $A_e/A_t = 5.95$ . Let us calculate the flow where  $p_e$  is *specified* as follows:

$$\frac{p_e}{p_{01}} = 0.6784 \quad (\text{specified}) \quad (7.123)$$

**FIG. 7.22**

Nomenclature for the normal shock case.

Note that this value is considerably below the values specified in Sec. 7.4 for the purely subsonic case; there, we specified, for example, that  $p_e/p_0 = 0.93$  and calculated the corresponding subsonic flow through the nozzle. Also note that the value  $p_e/p_{01} = 0.6784$  is considerably higher than that which came out of the subsonic-supersonic isentropic solution in Sec. 7.2, where we found that  $p_e/p_0 = 0.016$ . Hence, the value of  $p_e/p_{01} = 0.6784$  specified in the current section should be about right to force a normal shock wave to stand somewhere inside the divergent portion of the nozzle. Let us first calculate the precise location, i.e., the precise area ratio inside the nozzle, where the normal shock wave will be located, compatible with the specified exit pressure given in Eq. (7.123). This calculation can be done in a direct fashion as follows.

The mass flow through the nozzle can be expressed as

$$\dot{m} = \frac{p_{01} A_1^*}{\sqrt{T_0}} \sqrt{\gamma \left( \frac{2}{\gamma + 1} \right)^{(\gamma + 1)/(\gamma - 1)}} \quad (7.124)$$

See, for example, Refs. 8 and 21 for further discussion. That is, for a given  $T_0$ ,

$$\dot{m} \propto p_0 A^*$$

Since the mass flow is constant across the normal shock wave in Fig. 7.22, we have

$$p_{01} A_1^* = p_{02} A_2^* \quad (7.125)$$

(Keep in mind from our previous conversations that  $A^*$  is always defined as the *sonic* throat area; in the supersonic flow ahead of the shock,  $A_1^*$  is equal to the actual

throat area  $A_t$ , because the flow is actually sonic at  $A_t$ , whereas behind the shock  $A_2^*$  is the area the flow behind the shock would have to be reduced to in order to make it locally sonic. Since the flow behind the shock is always subsonic, then  $A_2^*$  never equals the actual physical throat area in the nozzle itself, because the entropy in region 2 is higher than in region 1.) Forming the ratio  $p_e A_e / p_{0_e} A_2^*$ , where  $A_e^* = A_2^*$ , and invoking Eq. (7.125), we have

$$\frac{p_e A_e}{p_{0_e} A_e^*} = \frac{p_e A_e}{p_{0_2} A_2^*} = \frac{p_e A_e}{p_{0_1} A_1^*} = \frac{p_e}{p_{0_1}} \frac{A_e}{A_t} \quad (7.126a)$$

The right-hand side of Eq. (7.126a) is known, because  $p_e/p_{0_1}$  is specified as 0.6784 and  $A_e/A_t = 5.95$ . Thus, from Eq. (7.126a)

$$\frac{p_e A_e}{p_{0_e} A_e^*} = 0.6784(5.95) = 4.03648 \quad (7.126b)$$

From the isentropic relations given by Eqs. (7.6) and (7.7), we have, respectively,

$$\frac{A_e}{A_e^*} = \frac{1}{M_e} \left[ \frac{2}{\gamma + 1} \left( 1 + \frac{\gamma - 1}{2} M_e^2 \right) \right]^{(\gamma + 1)/2(\gamma - 1)} \quad (7.127)$$

and  $\frac{p_e}{p_{0_e}} = \left( 1 + \frac{\gamma - 1}{2} M_e^2 \right)^{-\gamma/(\gamma - 1)}$  (7.128)

Substituting Eqs. (7.127) and (7.128) in (7.126b), we have

$$\frac{1}{M_e} \left( \frac{2}{\gamma + 1} \right)^{(\gamma + 1)/2(\gamma - 1)} \left[ 1 + \frac{\gamma - 1}{2} M_e^2 \right]^{-1/2} = 4.03648 \quad (7.129)$$

Solving Eq. (7.129) for  $M_e$ , we have

$$M_e = 0.1431 \quad (7.130)$$

From Eq. (7.128), we have

$$\frac{p_e}{p_{0_e}} = \left[ 1 + \frac{\gamma - 1}{2} (0.1431)^2 \right]^{-3.5} = 0.9858 \quad (7.131)$$

The total pressure ratio across the normal shock can be written as

$$\frac{p_{0_2}}{p_{0_1}} = \frac{p_{0_e}}{p_{0_1}} = \frac{p_{0_e}}{p_e} \frac{p_e}{p_{0_1}} \quad (7.132)$$

Substituting the numbers from Eqs. (7.123) and (7.131) into Eq. (7.132), we have

$$\frac{p_{0_2}}{p_{0_1}} = \frac{0.6784}{0.9858} = 0.6882 \quad (7.133)$$

The total pressure ratio across a normal shock is a function of  $M_1$  in front of the shock, given by (see Ref. 45)

$$\frac{p_{02}}{p_{01}} = \left[ \frac{(\gamma + 1)M_1^2}{(\gamma - 1)M_1^2 + 2} \right]^{\gamma/(\gamma-1)} \left[ \frac{\gamma + 1}{2\gamma M_1^2 - (\gamma - 1)} \right]^{1/(\gamma-1)} \quad (7.134)$$

Combining Eqs. (7.133) and (7.134) and solving for  $M_1$ , we have

$$M_1 = 2.07 \quad (7.135)$$

Substituting Eq. (7.135) into (7.6), we have

$$\frac{A_1}{A_1^*} = \frac{A_1}{A_t} = 1.790 \quad (7.136)$$

The exact, analytical location of the normal shock wave is now known—it stands at a location in the nozzle where the area ratio is 1.79. From Eq. (7.73) for our nozzle shape, this corresponds to a station of  $x/L = 2.1$ . All other properties across the shock wave now fall out from the result that  $M_1 = 2.07$ . For example, from Ref. 21, the static pressure ratio across the shock and the Mach number immediately behind the shock are obtained from

$$\frac{p_2}{p_1} = 1 + \frac{2\gamma}{\gamma + 1} (M_1^2 - 1) = 1 + 1.167[(2.07)^2 - 1] = 4.83 \quad (7.137)$$

and

$$M_2 = \left\{ \frac{1 + [(\gamma - 1)/2]M_1^2}{\gamma M_1^2 - (\gamma - 1)/2} \right\}^{1/2} = \left[ \frac{1 + 0.2(2.07)^2}{1.4(2.07)^2 - 0.2} \right]^{1/2} = 0.566 \quad (7.138)$$

The exact, analytical solution obtained above will be compared with the numerical solution in subsequent sections.

**BOUNDARY CONDITIONS.** The subsonic inflow boundary conditions are treated exactly as described in Sec. 7.5.2 and given by Eqs. (7.116) and (7.118); hence, no elaboration will be given here.

The outflow boundary condition for the present problem is also subsonic. A generic discussion of a subsonic outflow boundary was given in Sec. 7.4.1, where we emphasized that the exit pressure  $p_e$  must be specified, but all other properties are allowed to float. The same applies to the present calculation. However, in Sec. 7.4.1 we proceeded to couch the details of the numerical implementation of the subsonic outflow boundary condition in terms of the solution of the nonconservation form of the governing equations. In contrast, in the present calculation we are using the conservation form of the equations; hence the numerical implementation

is slightly different, as follows. Keep in mind that  $U_1$ ,  $U_2$ , and  $U_3$  are the primary dependent variables in the governing equations. Hence, we obtain  $U_1$  and  $U_2$  at the downstream boundary by linear extrapolation from the adjacent two interior points.

$$(U_1)_N = 2(U_1)_{N-1} - (U_1)_{N-2} \quad (7.139a)$$

$$(U_2)_N = 2(U_2)_{N-1} - (U_2)_{N-2} \quad (7.139b)$$

Next, we decode  $V'_N$  from  $(U_1)_N$  and  $(U_2)_N$  using Eq. (7.103).

$$V'_N = \frac{(U_2)_N}{(U_1)_N} \quad (7.140)$$

The value of  $U_3$  at grid point  $i = N$  is determined from the *specified* value of  $p'_N = 0.6784$  as follows. From the definition of  $U_3$ ,

$$U_3 = \rho' \left( \frac{e'}{\gamma - 1} + \frac{\gamma}{2} V'^2 \right) A' \quad (7.141)$$

However,  $e' = T'$ , and from the equation of state,  $p' = \rho' T'$ . Hence, Eq. (7.141) becomes

$$U_3 = \frac{p' A'}{\gamma - 1} + \frac{\gamma}{2} \rho' A' V'^2 \quad (7.142)$$

Since  $U_2 = \rho' A' V'$ , Eq. (7.142) becomes

$$U_3 = \frac{\rho' A'}{\gamma - 1} + \frac{\gamma}{2} U_2 V' \quad (7.143)$$

Evaluating Eq. (7.143) at the downstream boundary, we have

$$(U_3)_N = \frac{p'_N A'}{\gamma - 1} + \frac{\gamma}{2} (U_2)_N V'_N \quad (7.144)$$

Since  $p'_N$  is specified as 0.6784, Eq. (7.144) becomes

$$(U_3)_N = \frac{0.6784 A'}{\gamma - 1} + \frac{\gamma}{2} (U_2)_N V'_N \quad (7.145)$$

Equation (7.145) is the manner in which the specified exit pressure is folded into the numerical solution.

**INITIAL CONDITIONS.** For the present calculations, we choose the following initial conditions, which are qualitatively similar to the final solution. From  $x' = 0$  to 1.5, we use the same initial conditions as given by Eqs. (7.120a) to (7.120d). However, for  $x' > 1.5$ , we use

$$\rho' = 0.634 - 0.702(x' - 1.5) \quad \left. \begin{array}{l} \\ \end{array} \right\} \text{for } 1.5 \leq x' \leq 2.1 \quad (7.146a)$$

$$T' = 0.833 - 0.4908(x' - 1.5) \quad \left. \begin{array}{l} \\ \end{array} \right\} \text{for } 1.5 \leq x' \leq 2.1 \quad (7.146b)$$

$$\rho' = 0.5892 + 0.10228(x' - 2.1) \quad \left. \begin{array}{l} \\ \end{array} \right\} \text{for } 2.1 \leq x' \leq 3.0 \quad (7.146c)$$

$$T' = 0.93968 + 0.0622(x' - 2.1) \quad \left. \begin{array}{l} \\ \end{array} \right\} \text{for } 2.1 \leq x' \leq 3.0 \quad (7.146d)$$

As before, the initial condition for  $V'$  is determined by assuming a constant mass flow; it is calculated from Eq. (7.121).

### 7.6.2 The Intermediate Time-Marching Procedure: The Need For Artificial Viscosity

Perhaps the most dramatic distinction between the present shock-capturing case and our previous calculations in this chapter is the matter of artificial viscosity. Think back about our calculations so far; they have been carried out with no artificial viscosity explicitly added to the numerical calculations. The solutions of the subsonic-supersonic isentropic flow (Sec. 7.3) and the purely subsonic flow (Sec. 7.4) did not require additional numerical dissipation—there was enough dissipation inherent in the algorithm itself to yield stable and smooth solutions. Furthermore, it made no difference whether the governing equations were used in nonconservation form (Sec. 7.3 and 7.4) or in conservation form (Sec. 7.5). The requirement for artificial viscosity is essentially disconnected with which form of the equations is used. However, as we will see in the next section, when we practice the art of shock capturing, the smoothing and stabilization of the solution by the addition of some type of numerical dissipation is absolutely necessary. At this stage, return to Sec. 6.6 where the matter of artificial viscosity is introduced. Read this section again before proceeding further so that you can more fully understand what we have to do to obtain a reasonable solution for the nozzle flow with a normal shock wave standing inside the nozzle.

To proceed with this solution, we will add artificial viscosity in the manner described in Sec. 6.6. Specifically following Eq. (6.58), we form an expression

$$S'^i = \frac{C_x |(p')_{i+1}^{t'} - 2(p')_i^{t'} + (p')_{i-1}^{t'}|}{(p')_{i+1}^{t'} + 2(p')_i^{t'} + (p')_{i-1}^{t'}} (U_{i+1}^{t'} - 2U_i^{t'} + U_{i-1}^{t'}) \quad (7.147)$$

Whereas beforehand we would calculate a predicted value (using MacCormack's technique) from

$$\bar{U}_i^{t'+\Delta t'} = (U)_i^{t'} + \left( \frac{\partial U}{\partial t'} \right)_i^{t'} \Delta t'$$

we now replace this with

$$(\bar{U}_1)_i^{t'+\Delta t'} = (U_1)_i^{t'} + \left( \frac{\partial U_1}{\partial t'} \right)_i^{t'} \Delta t' + (S_1)_i^{t'} \quad (7.148)$$

$$(\bar{U}_2)_i^{t'+\Delta t'} = (U_2)_i^{t'} + \left( \frac{\partial U_2}{\partial t'} \right)_i^{t'} \Delta t' + (S_2)_i^{t'} \quad (7.149)$$

$$(\bar{U}_3)_i^{t'+\Delta t'} = (U_3)_i^{t'} + \left( \frac{\partial U_3}{\partial t'} \right)_i^{t'} \Delta t' + (S_3)_i^{t'} \quad (7.150)$$

where  $U_1$ ,  $U_2$ , and  $U_3$  are our dependent variables in Eqs. (7.101a) to (7.101c) and  $S_1$ ,  $S_2$ , and  $S_3$  in Eqs. (7.148) to (7.150) are obtained from Eq. (7.147) by using, respectively,  $U_1$ ,  $U_2$ , and  $U_3$  on the right-hand side. Similarly, on the corrector step, whereas beforehand we would calculate the corrected values from

$$U_i^{t'+\Delta t'} = U_i^t + \left( \frac{\partial U}{\partial t} \right)_{av} \Delta t'$$

we now replace this with

$$(U_1)_i^{t'+\Delta t'} = (U_1)_i^t + \left( \frac{\partial U_1}{\partial t} \right)_{av} \Delta t' + (\bar{S}_1)_i^t \quad (7.151)$$

$$(U_2)_i^{t'+\Delta t'} = (U_2)_i^t + \left( \frac{\partial U_2}{\partial t} \right)_{av} \Delta t' + (\bar{S}_2)_i^t \quad (7.152)$$

$$(U_3)_i^{t'+\Delta t'} = (U_3)_i^t + \left( \frac{\partial U_3}{\partial t} \right)_{av} \Delta t' + (\bar{S}_3)_i^t \quad (7.153)$$

where  $\bar{S}_1$ ,  $\bar{S}_2$ , and  $\bar{S}_3$  are obtained from an equation patterned after Eq. (6.59), namely,

$$\begin{aligned} \bar{S}_i^{t'+\Delta t'} &= \frac{C_x |(\bar{p}')_{i+1}^{t'+\Delta t'} - 2(\bar{p}')_i^{t'+\Delta t'} + (\bar{p}')_{i-1}^{t'+\Delta t'}|}{(\bar{p}')_{i+1}^{t'} + 2(\bar{p}')_i^{t'} + (\bar{p}')_{i-1}^{t'}} \\ &\times [(\bar{U})_{i+1}^{t'+\Delta t'} - 2(\bar{U})_i^{t'+\Delta t'} + (\bar{U})_{i-1}^{t'+\Delta t'}] \end{aligned} \quad (7.154)$$

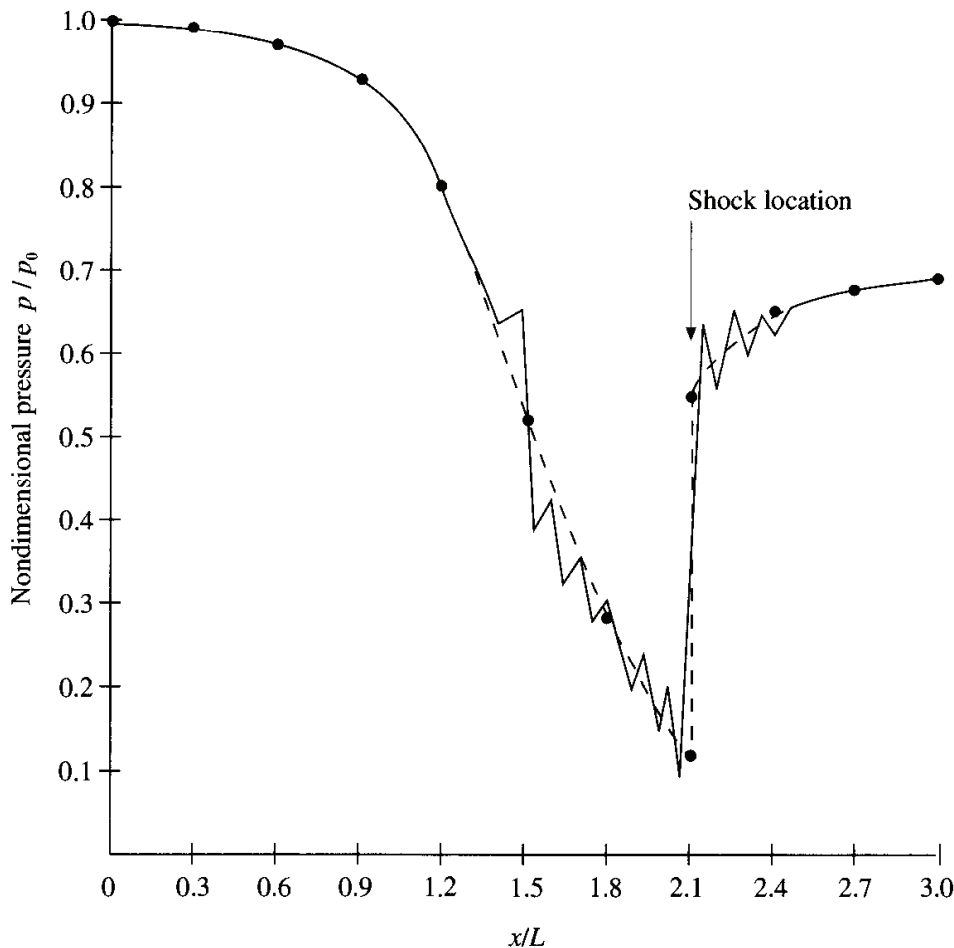
The values of  $\bar{S}_1$ ,  $\bar{S}_2$ , and  $\bar{S}_3$  are obtained from Eq. (7.154) by using, respectively, the values of  $\bar{U}_1$ ,  $\bar{U}_2$ , and  $\bar{U}_3$  on the right-hand side.

The rest of the shock-capturing solution proceeds in exactly the same manner as our previously described case in Sec. 7.5; hence no further elaboration will be given here. We will proceed directly to a discussion of the steady-state results.

### 7.6.3 Numerical Results

The following numerical results were obtained with 61 grid points distributed evenly through the nozzle rather than the 31-point grid used for most of our previous results. Since in the shock-capturing approach using MacCormack's finite-difference technique the captured shock wave is spread over several grid points, it is desirable to have a finer grid so as to more precisely define the location of the shock. Also, for the following results, a Courant number of 0.5 was employed. The conservation form of the governing flow equations was used in exactly the same manner as in Sec. 7.5 (except for the numerical implementation of the downstream boundary conditions, which has already been described in Sec. 7.6.1 and for the addition of artificial viscosity as described in Sec. 7.6.2). The pressure ratio at the nozzle exit is specified as  $p'_e = p_e/p_0 = 0.6784$  and is held fixed, invariant of time.

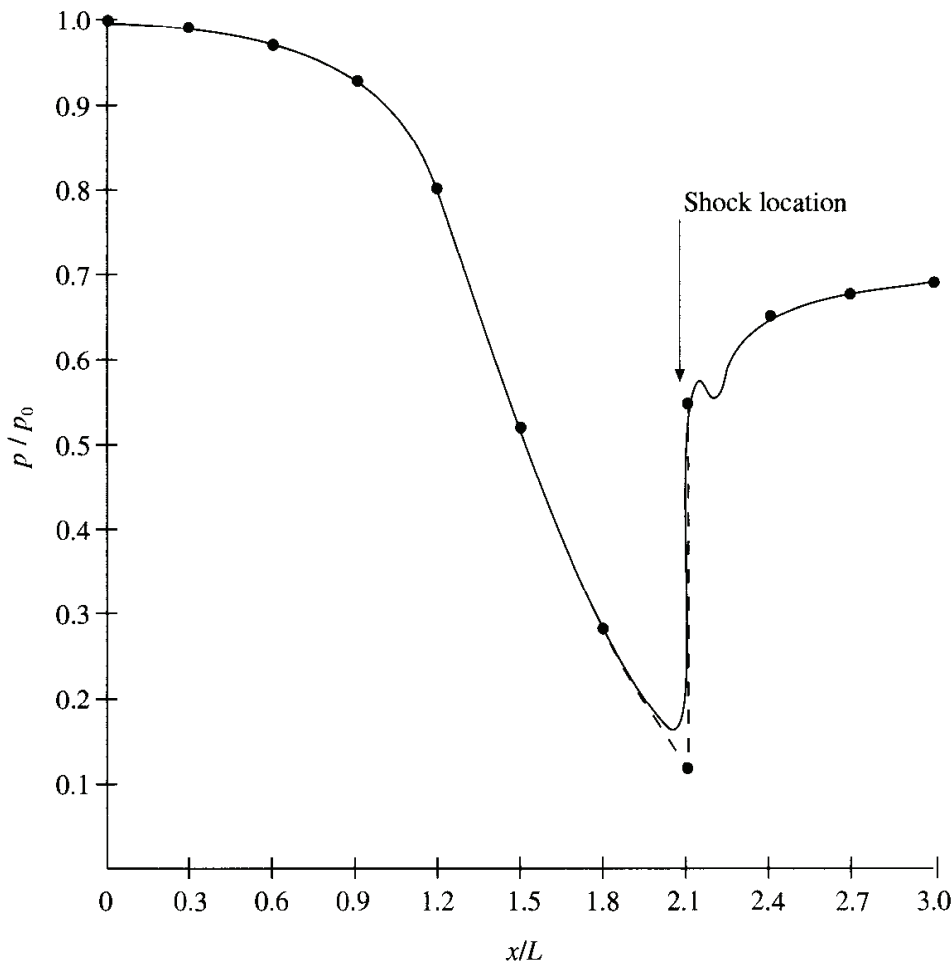
To begin with, it is instructional to examine what happens when *no* artificial viscosity is added to the calculations. Figure 7.23 shows the numerical solution for the pressure distribution through the nozzle (the solid line) compared with the exact,

**FIG. 7.23**

Shock-capturing numerical results (solid line) for the pressure distribution through the nozzle. No artificial viscosity. Results shown are for 1600 time steps. Comparison with the exact analytical results (solid circles connected by dashed curve).

analytical results (the solid circles connected by the dashed curve). The numerical solution is that obtained after 1600 time steps, corresponding to a nondimensional time of 17.2. No artificial viscosity has been added to this calculation. At 1600 time steps, the numerical results are not steady-state results. Although the numerical results are trying to capture the shock wave in about the right location, the residuals are still fairly large—on the order of  $10^{-1}$ . Moreover, as time progresses beyond 1600 time steps, the residuals start to grow instead of decreasing as they should. By 2800 time steps, the attempted solution has not blown up, but the oscillations have grown much more pronounced, and some of the residuals have grown to  $10^1$ . This is a totally unsatisfactory solution, and we will not discuss it further. It needs to be fixed by the addition of artificial viscosity, as discussed below.

When artificial viscosity is added to the calculation via Eqs. (7.147) to (7.154) and the adjustable constant  $C_x$  is set equal to 0.2, the following results are obtained. The steady-state pressure distribution through the nozzle is shown in Fig. 7.24. The numerical results (the solid curve) are shown after 1400 time steps—the converged, steady state. The exact, analytical results are given by the solid circles connected by the dashed curve. From Fig. 7.24, we make the following observations:

**FIG. 7.24**

Shock-capturing numerical results (solid curve) for the pressure distribution through the nozzle. With artificial viscosity;  $C_x = 0.2$ . Results shown are for 1400 time steps. Comparison with exact, analytical results (solid circles connected by dashed curve).

1. The addition of artificial viscosity has just about eliminated the oscillations that were encountered in the case with no artificial viscosity. The contrast between the numerical results in Fig. 7.24 (with  $C_x = 0.2$ ) and those in Fig. 7.23 (with  $C_x = 0.0$ ) is dramatic. This is what artificial viscosity does—smooth the results and decrease (if not virtually eliminate) the oscillations.
2. Close examination of Fig. 7.24 shows that the oscillations are not *completely* eliminated. There is a small oscillation in the pressure distribution just downstream of the shock; however, it is not that bothersome. Results obtained with more artificial viscosity ( $C_x = 0.3$ ) show that even this small oscillation virtually disappears. However, *too much* artificial viscosity can compromise other aspects of the solution, as noted below.
3. The numerical results in Fig. 7.24 show that artificial viscosity tends to smear the captured shock wave over more grid points. The more extreme changes across the shock that are predicted by the exact, analytical results are slightly diminished by the inclusion of artificial viscosity in the numerical results. This increased smearing of the shock wave due to increased artificial viscosity is one of the undesirable aspects of adding extra numerical dissipation to the

solution. Some modern CFD methods (beyond the scope of this book) have successfully improved this situation; by using innovative ideas from applied mathematics, current researchers are able to reap the benefits of adding numerical dissipation when and where in the flow field it is really needed and still preserve the sharpness of the captured shock wave. Such matters are left to your future advanced studies of CFD.

The steady-state Mach number distribution is shown in Fig. 7.25; these results simply reinforce the comments made above.

The detailed steady-state numerical results, obtained after 1400 time steps, are tabulated in Table 7.13 for comparison with numbers obtained with your own computer program. Just as a reminder, these results are obtained by using the conservation form of the governing equations, artificial viscosity where  $C_x = 0.2$ , a Courant number of 0.5, and 61 points evenly distributed along the nozzle. The solution corresponds to a specified exit pressure ratio  $p_e/p_0 = 0.6784$ . Scanning down the various columns for  $\rho'$ ,  $p'$ , etc., in the vicinity of the shock wave (which is theoretically located at grid point  $i = 43$ , i.e., at  $x' = 2.1$ ) we see just how small is the slight oscillation downstream of the shock. However, focus for a moment on the column for mass flow; here we see that  $\dot{m} = \rho' A' V'$  is essentially constant upstream of the shock wave at a value of  $\rho' A' V' = 0.582$ . (Recall that the exact, analytical

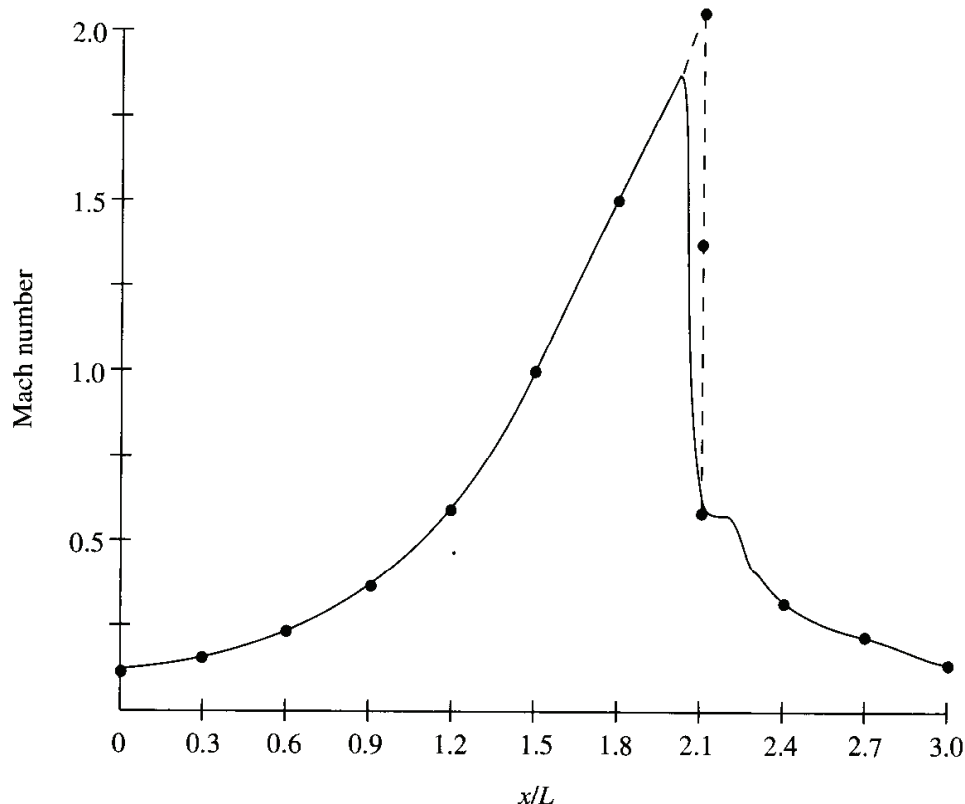


FIG. 7.25

Shock-capturing numerical results (solid curve) for the Mach number distribution through the nozzle. With artificial viscosity;  $C_x = 0.2$ . Results shown here are for 1400 time steps. Comparison with the exact, analytical results (solid circles connected by dashed curve).

**TABLE 7.13**  
Shock capturing, steady-state numerical results

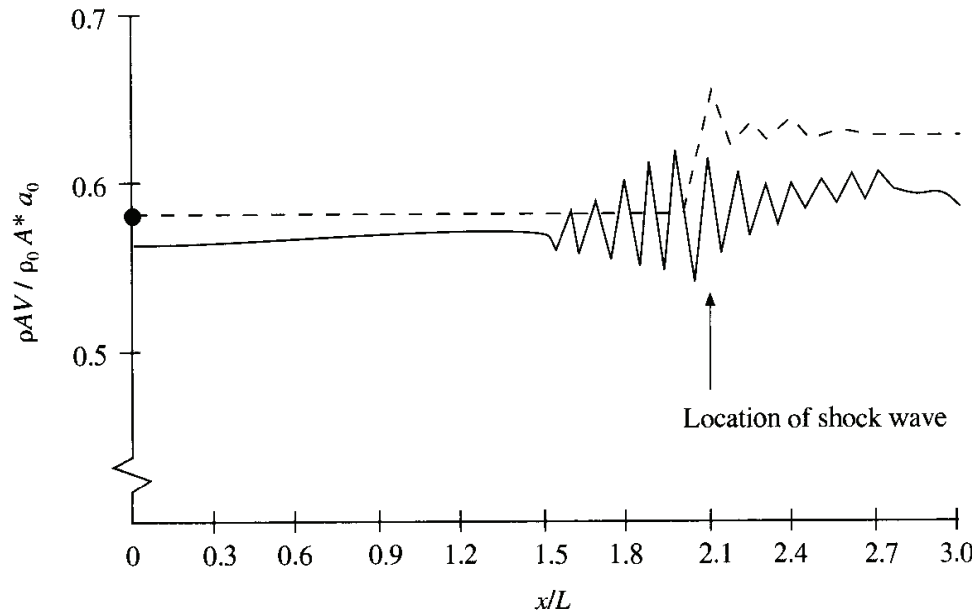
<i>I</i>	$\frac{x}{L}$	$\frac{A}{A^*}$	$\frac{\rho}{\rho_0}$	$\frac{V}{a_0}$	$\frac{T}{T_0}$	$\frac{p}{p_0}$	<i>M</i>	<i>m</i>
1	0.000	5.950	1.000	0.098	1.000	1.000	0.098	0.582
2	0.050	5.626	0.999	0.103	1.000	0.999	0.103	0.582
3	0.100	5.312	0.999	0.110	1.000	0.998	0.110	0.582
4	0.150	5.010	0.998	0.116	0.999	0.997	0.116	0.582
5	0.200	4.718	0.997	0.124	0.999	0.996	0.124	0.582
6	0.250	4.438	0.996	0.132	0.998	0.995	0.132	0.582
7	0.300	4.168	0.995	0.140	0.998	0.993	0.140	0.582
8	0.350	3.910	0.994	0.150	0.997	0.991	0.150	0.582
9	0.400	3.662	0.992	0.160	0.997	0.989	0.160	0.582
10	0.450	3.425	0.990	0.172	0.996	0.986	0.172	0.582
11	0.500	3.200	0.988	0.184	0.995	0.983	0.184	0.582
12	0.550	2.985	0.985	0.198	0.994	0.979	0.198	0.582
13	0.600	2.782	0.982	0.213	0.993	0.975	0.214	0.582
14	0.650	2.589	0.979	0.230	0.991	0.970	0.231	0.582
15	0.700	2.408	0.974	0.248	0.990	0.964	0.249	0.582
16	0.750	2.237	0.969	0.268	0.987	0.957	0.270	0.582
17	0.800	2.078	0.963	0.291	0.985	0.948	0.293	0.582
18	0.850	1.929	0.956	0.316	0.982	0.938	0.319	0.582
19	0.900	1.792	0.947	0.343	0.978	0.926	0.347	0.582
20	0.950	1.665	0.936	0.373	0.974	0.912	0.378	0.582
21	1.000	1.550	0.924	0.407	0.969	0.895	0.413	0.582
22	1.050	1.445	0.909	0.443	0.963	0.875	0.452	0.582
23	1.100	1.352	0.892	0.483	0.955	0.852	0.494	0.583
24	1.150	1.270	0.872	0.526	0.946	0.825	0.541	0.583
25	1.200	1.198	0.848	0.573	0.936	0.794	0.593	0.583
26	1.250	1.138	0.821	0.624	0.924	0.759	0.649	0.583
27	1.300	1.088	0.791	0.678	0.910	0.720	0.710	0.583
28	1.350	1.050	0.757	0.734	0.894	0.677	0.776	0.583
29	1.400	1.022	0.719	0.793	0.876	0.630	0.847	0.583
30	1.450	1.006	0.679	0.854	0.856	0.581	0.923	0.583

value is 0.579—the numerical result is very close.) But in the vicinity of the shock wave, *m* takes a substantial jump and seems to settle in to a value of about 0.632 further downstream of the shock wave.

A further look at this spurious mass flow behavior is provided in Fig. 7.26. Here, the nondimensional mass flow  $\rho' A' V'$  is plotted versus distance through the nozzle. The scale of the graph is the same as that used in Fig. 7.19 for the subsonic-supersonic isentropic flow case. The solid line corresponds to the numerical results (obtained after 1600 time steps) for the case with no artificial viscosity ( $C_x = 0$ ); the dashed line gives the numerical results for the case with artificial viscosity ( $C_x = 0.2$ ). Note that with no artificial viscosity the mass flow exhibits a massive, vibratory behavior in the general vicinity of the shock wave—totally unacceptable, as stated before. In contrast, the case with artificial viscosity exhibits excellent mass flow behavior *upstream* of the shock wave, with a quality and accuracy every bit as good as that reflected in the steady-state results for the

<i>I</i>	$\frac{x}{L}$	$\frac{A}{A^*}$	$\frac{\rho}{\rho_0}$	$\frac{V}{a_0}$	$\frac{T}{T_0}$	$\frac{p}{p_0}$	<i>M</i>	$\dot{m}$
31	1.500	1.000	0.633	0.921	0.832	0.527	1.009	0.583
32	1.550	1.005	0.596	0.973	0.812	0.484	1.080	0.583
33	1.600	1.022	0.549	1.040	0.786	0.431	1.173	0.583
34	1.650	1.049	0.507	1.096	0.761	0.386	1.256	0.584
35	1.700	1.088	0.462	1.159	0.734	0.339	1.353	0.583
36	1.750	1.137	0.424	1.210	0.709	0.301	1.437	0.584
37	1.800	1.198	0.383	1.268	0.680	0.261	1.538	0.582
38	1.850	1.269	0.351	1.311	0.658	0.231	1.617	0.584
39	1.900	1.352	0.315	1.368	0.628	0.198	1.725	0.582
40	1.950	1.445	0.289	1.398	0.611	0.177	1.788	0.584
41	2.000	1.550	0.256	1.462	0.574	0.147	1.930	0.581
42	2.050	1.665	0.318	1.207	0.677	0.215	1.467	0.639
43	2.100	1.792	0.524	0.697	0.872	0.457	0.747	0.655
44	2.150	1.929	0.619	0.521	0.925	0.573	0.542	0.622
45	2.200	2.078	0.613	0.501	0.926	0.567	0.521	0.638
46	2.250	2.237	0.643	0.436	0.939	0.604	0.450	0.627
47	2.300	2.408	0.643	0.410	0.943	0.607	0.422	0.635
48	2.350	2.589	0.660	0.368	0.950	0.627	0.378	0.629
49	2.400	2.782	0.662	0.344	0.953	0.631	0.353	0.635
50	2.450	2.985	0.671	0.314	0.959	0.643	0.321	0.629
51	2.500	3.200	0.675	0.294	0.958	0.647	0.300	0.634
52	2.550	3.425	0.680	0.271	0.964	0.655	0.276	0.630
53	2.600	3.662	0.682	0.253	0.965	0.658	0.258	0.633
54	2.650	3.909	0.687	0.235	0.965	0.663	0.239	0.632
55	2.700	4.168	0.687	0.221	0.969	0.666	0.224	0.632
56	2.750	4.437	0.690	0.206	0.970	0.669	0.209	0.631
57	2.800	4.718	0.692	0.194	0.970	0.671	0.197	0.633
58	2.850	5.009	0.694	0.182	0.971	0.674	0.184	0.631
59	2.900	5.312	0.694	0.171	0.973	0.675	0.174	0.631
60	2.950	5.625	0.697	0.161	0.972	0.677	0.164	0.632
61	3.000	5.950	0.698	0.152	0.972	0.678	0.154	0.632

subsonic-supersonic isentropic flow solution shown in Fig. 7.19 and tabulated in Table 7.11. However, in the vicinity of the shock wave, the case with artificial viscosity takes an almost quantum jump in mass flow, leveling out at the nozzle exit to a value about 8.6 percent higher than at the nozzle inlet. Clearly, the artificial viscosity terms added to the numerical solution of the governing equations are acting like a *source* of mass flow in the vicinity of the shock wave. This is not hard to imagine when you again examine Eqs. (7.147) to (7.154). Note that the values of  $S_i''$  obtained from Eq. (7.147) and those for  $\bar{S}_i^{t'+\Delta t'}$  obtained from Eq. (7.154) are large in those regions of the flow where the change in pressure gradients are large; this is the role of the leading factor involving pressure in these expressions—it plays the role of a “sensor” which increases the amount of artificial viscosity in those regions where the pressure gradients are changing rapidly (the second derivative of the pressure), such as when the oscillatory behavior discussed earlier tries to occur. Furthermore, these values of  $S_i''$  and  $\bar{S}_i^{t'+\Delta t'}$  are directly added to the calculated

**FIG. 7.26**

Comparison of mass flow distributions with artificial viscosity (dashed line;  $C_x = 0.2$ ) and without artificial viscosity (solid line;  $C_x = 0$ ). Solid circle indicates exact analytical result.

values of the  $U_i$ 's via Eqs. (7.148) to (7.150) and (7.151) to (7.154). In particular, recall that  $U_2 = \rho' A' V'$  is the mass flow. Therefore, it is no surprise that the artificial viscosity governed by the scheme originally described in Sec. 6.6 would lead to source terms for mass flow.

Is this mass flow behavior for cases with artificial viscosity acceptable? The answer is essentially yes when you consider the alternative. Clearly, shock capturing leads to unacceptable oscillations (and sometimes unstable behavior) when no artificial viscosity is used in the calculations. So we *have* to use artificial viscosity, at least for the explicit MacCormack technique we have been illustrating in this chapter. In general, the results for the *primitive variables* that are obtained via a shock-capturing solution with artificial viscosity are acceptable. This is shown in Tables 7.14 and 7.15. In Table 7.14, we tabulate the steady-state flow-field values at the nozzle throat for the cases with  $C_x$  ranging from 0 to 0.3 and compare them with the exact analytical values. The case with no artificial viscosity,  $C_x = 0$ , has already

**TABLE 7.14**  
Shock-capturing solution; values at the nozzle throat

	$\frac{\rho}{\rho_0}$	$\frac{V}{a_0}$	$\frac{T}{T_0}$	$\frac{p}{p_0}$	$M$	$\dot{m}$
Exact analytical values	0.634	0.913	0.833	0.528	1.0	0.579
Numerical values:						
$C_x = 0$	0.735	0.784	0.879	0.646	0.836	0.576
$C_x = 0.1$	0.629	0.926	0.831	0.523	1.016	0.583
$C_x = 0.2$	0.633	0.921	0.832	0.527	1.009	0.583
$C_x = 0.3$	0.640	0.911	0.836	0.535	0.997	0.583

**TABLE 7.15**  
Shock-capturing solution; values at the nozzle exit

	$\frac{\rho}{\rho_0}$	$\frac{V}{a_0}$	$\frac{T}{T_0}$	$\frac{p}{p_0}$	$M$	$m$
Exact analytical values	0.681	0.143	0.996	0.678	0.143	0.579
Numerical values:						
$C_x = 0$	0.672	0.148	1.009	0.678	0.147	0.591
$C_x = 0.1$	0.694	0.151	0.978	0.678	0.153	0.624
$C_x = 0.2$	0.698	0.152	0.972	0.678	0.154	0.632
$C_x = 0.3$	0.698	0.153	0.972	0.678	0.155	0.634

been affected at the throat by the oscillations working their way upstream from the shock wave; the comparison with the exact analytical values shows that the numerical results with no artificial viscosity are totally unacceptable. In contrast, the results with artificial viscosity are quite good. Indeed, the results at the nozzle throat obtained for the case with  $C_x = 0.2$  are the most accurate of *any* case we have examined in this chapter! In Table 7.15, we tabulate the steady-state flow-field values at the nozzle exit, downstream of the captured normal shock wave. It is interesting to note (but not too surprising) that as the artificial viscosity is increased, the numerical results for the exit flow-field variables progressively move further away from the exact analytical values. Indeed, the results from the case with no artificial viscosity give the best comparison with the exact analytical results. On the other hand, the case for  $C_x = 0$  is tabulated after 1600 time steps; as we have mentioned earlier, this case further deviates away from the steady state as time progresses and may very well blow up after enough time steps are taken. Therefore, the comparison associated with  $C_x = 0$  in both Tables 7.14 and 7.15 is really moot.

With this, we end our discussion of shock capturing in a convergent-divergent nozzle. This has been a particularly relevant section, because:

1. It is an illustration of the shock-capturing philosophy as first discussed in Sec. 2.10. This is one of the two basic approaches for handling shock waves in CFD, the other being shock fitting. The shock-capturing philosophy is, by far, the most prevalent in CFD today.
2. It was our first application of artificial viscosity, which allowed us to examine some of the pros and cons of explicitly increasing the amount of numerical dissipation in the solution.
3. It allowed us the opportunity to calculate yet another flow using the conservation form of the governing equations. This form of the equations is, by far, the most prevalent in CFD today.

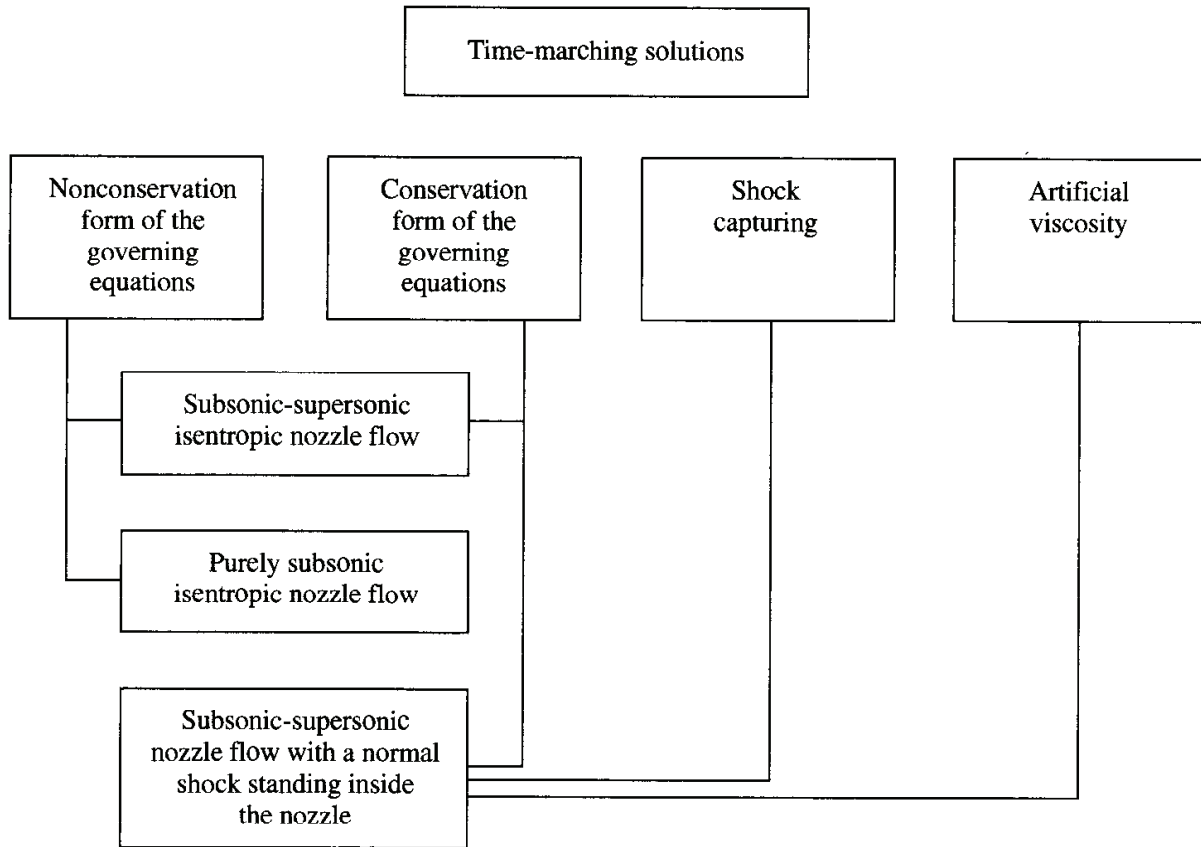
Also, let us wax philosophical for a moment. In this section, we have calculated a flow which contains a shock wave *without doing anything special to account for the shock*; that is, we have employed a form of the governing Euler equations for an inviscid flow and have imposed boundary conditions across the nozzle that, in

nature, calls for a shock wave to be present in the nozzle. The numerical solution of the Euler equations senses this need for a shock wave and establishes it within the flow. Of course, this is the essence of shock capturing. But isn't it rather awesome that a set of equations for an *inviscid* flow, namely, the Euler equations, will allow the solution of such a flow with shock waves without us adding some additional *theoretical* baggage to the equations to alert them to the existence of the shock? Of course, some of the awesomeness is diminished when we realize that the *numerical solution* is really not solving the exact Euler equations, but rather a set of modified differential equations in the spirit of our discussion in Sec. 6.6, and that these modified equations have viscouslike terms on the right-hand side. Moreover, during the numerical solution, we are adding even more numerical dissipation via the artificial viscosity terms. Therefore, what we think is the numerical solution of the Euler equations is really a solution of some "mildly viscouslike" equations, which in turn have the mechanism (through these viscouslike terms) to create a shock wave. In any event, it is still somewhat a marvel to this author that not only will shock waves form in such a numerical solution, but they will be the *correct* shock waves with (more or less) the correct jump conditions across the wave as well as standing at the correct location in the flow.

## 7.7 SUMMARY

This brings to a conclusion our application of CFD to the time-marching solution of quasi-one-dimensional nozzle flows. Such flows are particularly useful in this regard because, within the framework of a relatively familiar flow problem, many of the important facets of CFD as discussed in Chaps. 1 to 6 can be illustrated. The flow of ideas in the present chapter can be diagrammed on the road map shown in Fig. 7.27. Once again we put the road map at the end of the chapter because it has the most significance *after* we have labored through our various cases. Examining Fig. 7.27, we make the following observations about the content of Chap. 7:

1. It has provided a nonstop illustration of the philosophy of time marching to obtain steady-state solutions in the limit of large times. The use of time-marching solutions in CFD is extensive.
2. Reading across the top row of blocks in Fig. 7.27, we have four of the most important aspects of CFD, namely, the choice between the nonconservation form and the conservation form of the governing equations, the use of the conservation form in conjunction with the shock-capturing philosophy, and the corresponding need for artificial viscosity.
3. We applied both the nonconservation and the conservation forms for solutions of the subsonic-supersonic isentropic nozzle flow and compared the results. For all practical purposes, the results are the same, except that the conservation form yielded a slightly better mass flow distribution. Artificial viscosity is not needed to obtain solutions for this flow, and none was used.
4. The solution of the purely subsonic flow provided an opportunity to explore the effect of the numerical implementation of *boundary conditions*—a vital aspect of

**FIG. 7.27**

Road map for Chap. 7.

CFD. Here, the subsonic flow case is driven by a *fixed* pressure ratio between the exit and inlet, invariant with time. This case provided a further opportunity to discuss the various aspects of subsonic and supersonic inflow and outflow boundary conditions. We chose to use the nonconservation form of the equations for this solution—we could have just as well used the conservation form.

5. The case with a normal shock wave standing inside the nozzle was an opportunity for the confluence of four important streams in CFD, namely, (a) the *necessary* use of the conservation form of the governing equations, (b) the application of the shock-capturing philosophy, (c) the *necessary* use of artificial viscosity to obtain a quality solution, and (d) once again, the way that a subsonic outflow boundary condition can be implemented.